SAINT-PETERSBURG UNIVERSITY

Published in manuscript form

Zhao Shixiang

DYNAMIC PLASTICITY MODELING OF METALLIC MATERIALS UNDER IMPACT LOADS: STRAIN-RATE EFFECTS AND THERMAL SOFTENING PHENOMENA

Scientific specialty – 1.1.8. Solid Mechanics

DISSERTATION

Thesis for the degree of Candidate of Physico-Mathematical Sciences
(Translation from Russian)

Scientific advisor:
Corresponding Member of the Russian Academy of Sciences,
Doctor of Physical and Mathematical Sciences,
Professor Yuri V. Petrov

Saint-Petersburg
2024

Contents

Introduction

The relevance of the thesis topic

The thesis topic is highly relevant due to its potential applicability for various industries and engineering applications. For instance, in the field of automotive industry, where crashworthiness and occupant safety are paramount concerns, studying the plastic behavior of metallic materials under impact loads is essential. The research's focus on developing accurate models that consider strain-rate effects and thermal softening phenomena allows for predicting material response during high-speed collisions or accidents. Consequently, this aids in designing improved vehicle structures and safety systems, leading to enhanced passenger protection. In the aerospace sector, the research topic is crucial for aircraft design, particularly in emergency landing scenarios and bird strikes. Through the incorporation of strain-rate effects and thermal softening phenomena in computational models, engineers can optimize the structural integrity of aircraft components. This optimization contributes to safer and more reliable flight operations, mitigating risks associated with impact events. Moreover, this work can be used for metal cutting processes. Accurate modeling of material responses during cutting operations allows manufacturers to optimize machining parameters, tool design, and cutting strategies. By gaining insights into dynamic plasticity under impact loads, improvements in safety, reliability, and efficiency can be achieved in a range of applications.

The degree of development of the thesis topic

The plastic deformation at high-loading rates is often accompanied by an obvious adiabatic temperature rise. This process involves strain rate effects and thermal softening phenomenon. To account for the combined influence of strain rate and temperature, a strain rate-temperature correspondence is proposed. It assumes that the increased stress caused by higher strain rates can be effectively simulated by lowering the temperature. Mathematically, this relationship is expressed through the multiplicative form $\sigma = f_1(\varepsilon_p, \dot{\varepsilon}) f_2(\varepsilon_p, T)$, where f_1 represents the function capturing the strain rate effect, and f_2 represents the function accounting for the temperature effect. Empirical formulations can be found in numerous models [1] [2] [3] [4] [5]. These models are usually investigated by introducing additional and empirical rate-dependent and temperature-dependent components into classical models initially developed for quasi-static cases. They give a satisfactory description of dynamic plastic behavior for many materials and are widely used to deal with different engineering problems. However, they are proposed using the direct empirical curve fitting approach based on the experimental analysis.This is so-called empirical fitting approach. In addition, the dynamic stress-strain curves of many materials are non-monotonic. The yield drop phenomenon can be observed in series of experiments and often neglected in the simulation of stress–strain diagrams. Plastic deformation in metals occurs mainly by the motion of dislocations. Many micromechanism-based models [6] [7] are also developed, incorporating physical background of plastic deformation. This approach requires a detailed understanding of the material's microstructure and the interaction between dislocations, and the value of some model's parameters can be challenging to determine experimentally. The incubation time approach proposed by Petrov and Morozov provides a new viewpoint for understanding the dynamic response of materials. They indicate that in the limit case of low-rate loading it transfers into the classical quasi-static models by neglecting certain insignificant components. This approach requires further development.

Goals and tasks of the thesis

The primary goal of this thesis is to provide a new perspective in understanding strain rate sensitivity and thermal softening response of metallic materials by developing the incubation time approach. This approach aims to study the relaxation model of plasticity, considering the influence of strain rate effects and thermal softening phenomena, while also accounting for negative hardening behavior of materials subjected to high-rate loads.

To achieve this overarching goal, several specific tasks have been identified:

1. Develop the RP model. This includes formulating a comprehensive model that incorporates the incubation time approach and accurately represents the strain

rate sensitivity and thermal softening effects observed in metallic materials under impact loads.

2. Investigate the temperature-time correspondence. By analyzing experimental data and introducing the concept of the relative stress factor, the research aims to establish the relationship between temperature and incubation time in order to better understand the dynamic plastic response of metallic materials.
3. Perform a comparative analysis between different existing models. This task involves evaluating and comparing the proposed RP model with other existing models used for dynamic plasticity modeling. By assessing their strengths and weaknesses, insights can be gained to further enhance the accuracy and effectiveness of the RP model.
4. Develop a computational approach for the RP model within finite element analysis (FEA) to simulate 3D plasticity problems. This task focuses on implementing a robust computational framework using FEA techniques. The aim is to enable accurate simulation and prediction of the plastic behavior of metallic materials under impact loads, incorporating the developed RP model.

Scientific novelty

The plastic response of metals under impact loads is generally modeled by introducing the rate-dependent and temperature-dependent components into hardening models originally developed for quasi-static cases. The multiplicative from $\sigma = f_1(\varepsilon_p, \dot{\varepsilon}) f_2(\varepsilon_p, T)$ is widely accepted. Differing from that, we consider the strain-rate sensitivity as a manifestation of the time sensitivity of materials and develop the relaxation model of plasticity (RP model) using the incubation time approach. The original RP model has a limited ability to describe work-hardening response over a wide range of strain rates and temperatures. The temperature-time dependence is also comprehensively examined. Previous studies [8] [9] [10] have discussed some temperature-time dependences. Nevertheless, they were performed within a limited range of strain and strain rate, and the adiabatic temperature rise appeared under impact loading was not considered. Additionally, the impact of temperature on the elastic properties of the materials studied was not considered, which could influence the incubation time measurement. In contrast to previous researches, this study establishes a framework of modified RP model to overcome existing difficulties and examines the temperature-time correspondence by introducing the relative stress (RS) factor over a wide range of strain, strain rate and temperature. Experiments demonstrate that the RS factor has a clear rate-dependent and temperature-dependent behavior pattern, which must be followed by the temperature-time correspondence. However, the multiplicative model in the form $\sigma = f_1(\varepsilon_p, \dot{\varepsilon}) f_2(\varepsilon_p, T)$ leads to a temperature-independent behavior of the RS factor. In addition, a possible explanation for the existence of different proposed phenomenological temperature-time correspondences are discussed. The relation between this model and the yield surface equation within the incubation time framework is explored. As a result, using the incubation time approach, we can describe the non-monotonic/softening stress-strain diagram, i.e. the negative hardening, due to thermal softening induced by the adiabatic plastic deformation under high-rate loading conditions. The main differences between the artificial neural networks (ANN model) and constitutive models are discussed. At last, a computational approach for RP model used in FEA is proposed firstly.

Research methods

The RP model is developed through incubation time approach. The temperature-time correspondence is examined by introducing the relative stress factor and analyzing existing experimental data at different strain rates and temperatures. The computational scheme is implemented using the finite element method. To solve dynamic plasticity problems associated with the RP model, several numerical techniques are employed. Firstly, we use the explicit method for time integration to efficiently handle the transient nature of these problems. Additionally, the return mapping algorithm is incorporated to ensure accurate computation of the plastic strains. Moreover, we adopt a safe version of the Newton-Raphson method to achieve robust convergence during the iterative solution process. By combining the incubation time approach, analysis of experimental data, and implementation of various numerical techniques, our developed computational scheme provides a comprehensive framework for studying dynamic plasticity problems within the context of the RP model.

Theoretical and practical significance

This work has significant theoretical importance as it contributes to the development of the relaxation model of plasticity, the establishment of temperature-time correspondence, and the formulation of a computational algorithm for finite element analysis (FEA). These advancements improve our understanding of dynamic plasticity and enhance the accuracy of simulations. Specifically, the work enriches the field by expanding the application of the incubation time approach. By incorporating this approach into the modeling of dynamic plastic response of metallic materials, the study provides a valuable framework for simulating and predicting their behavior under impact loads. Practically, this thesis has direct relevance to engineering applications that require the simulation and prediction of material plastic behavior under impact conditions. Industries such as automotive, aerospace, and structural engineering can benefit from these results to optimize designs, improve safety measures, and ensure the integrity of components subjected to high-velocity impacts.

Results submitted for defense

1. Framework of the modified relaxation model of plasticity (RP model). A simplified version and incremental version of the RP model are introduced. The incubation time approach considers the rate sensitivity as a manifestation of time sensitivity of materials.

2. Methodology of investigating the temperature-time correspondence. The relative stress (RS) factor is introduced to analyze the tendency of the temperature-time relationship over a wide range of strain, strain rate and temperature. The reliability of the methodology is confirmed by existing experimental data.

3. Result of the study on the descriptive ability of multiplicative models $\sigma = f_1(\varepsilon_p, \dot{\varepsilon}) f_2(\varepsilon_p, T)$. These models are improper to simulate the strain-rate effect and thermal softening phenomenon over a wide temperature range. They are derived from the direct empirical fitting approach and results in a temperature-independent RS factor, which does not follow the behavior pattern of the RS factor observed by analyzing existing experimental facts.

4. Results of the comparative analysis of the IRP model with other phenomenological models and micromechanism-base models. The comparison is performed based on experimental data from various metallic materials including aluminium alloy 6082-T6, 2519A, HSLA-65 steel, 93W–4.9Ni–2.1Fe tungsten-based composite, and titanium alloy Ti-6Al-4V.

5. An artificial neural network model and results of its comparative analysis with other discussed constitutive models. The ANN model uses a data-driven learning approach, while other constitutive models are proposed by the rule-based analyzing method.

6. New approaches and results of modeling negative hardening in HSLA-65 steel, induced by rapid plastic deformation and adiabatic energy dissipation.

7. An original computational scheme for finite element analysis of dynamic plasticity problems using a simplified version of the RP model. For solving three-dimensional dynamic plasticity problems, a Fortran program based on the developed finite element scheme has been implemented.

8. Software modules written in Python for calculating stress-strain diagrams of various materials and determining parameters of different models.

The **main scientific achievements** obtained during the dissertation research include the following:

1. Modification of the relaxation model of plasticity. The modified RP model can be derived from the yield surface equation within the framework of the incubation time approach, while many other phenomenological models are primarily derived using a direct empirical approach. This is one of the main differences between the modified RP model and other phenomenological models.

2. Estimation of the dependence between incubation time and temperature for HSLA-65 steel and the tungsten-based composite 93W–4.9Ni–2.1Fe, as well as the titanium alloy Ti–6Al–4V.

3. Comparison of the IRP model with other constitutive models. It is shown that the commonly used multiplicative form $\sigma = f_1(\varepsilon_p, \dot{\varepsilon}) f_2(\varepsilon_p, T)$ is not suitable

for modeling the strain rate effect and thermal softening over a wide range of temperatures.

4. Modeling of negative hardening in HSLA-65 steel induced by rapid deformation and adiabatic energy dissipation.
5. Development of an original computational scheme for finite element analysis of dynamic plasticity problems using a simplified version of the RP model. Simulation of split Hopkinson pressure bar experiments using the finite element method (FEM) was conducted to verify the developed computational scheme. The simulation results show good agreement with available experimental data.

Verification of results

The main results of the thesis were presented by the author at the following conferences:

1. International Student Conference "Science and Progress" organized by German-Russian Interdisciplinary Science Center (Saint Petersburg, 2021).
2. 7th International Conference on Crack Paths (Trondheim, 2021).
3. School-Seminar "Mechanics, Chemistry, and New Materials" (Saint Petersburg, 2022, 2023)
4. 13th Russian Congress on Theoretical and Applied Mechanics (Saint Petersburg, 2023)
5. 3rd Sino-Russian Forum «Material science & Technology» (Harbin, 2023)

At the 13th Russian Congress on Theoretical and Applied Mechanics held in 2023, the author was awarded for the best sectional presentation among young scientists.

Based on the results of the thesis, 6 works were published, the following 3 of which are indexed by the Web of Science and Scopus databases:

1. Modeling of the thermal softening of metals under impact loads and their temperature–time correspondence / S. Zhao, Yu. V. Petrov, Yuyi Zhang et al. // International Journal of Engineering Science. — 2024. — Vol. 194. — P. 103969. (Q1)

2. Zhao S., Petrov Yu.V., Volkov G.A. The modified relaxation plasticity model and the non-monotonic stress–strain diagram // International Journal of Mechanical Sciences. — 2023. — Vol. 240. — P. 107919. (Q1)
3. Zhao S., Petrov Yu. V., Volkov G. A. Modeling the Nonmonotonic Behavior Flow Curves under Dynamic Loads // Physical Mesomechanics. — 2022. — Vol. 25, no. 3. — P. 221–226. (Q2)

Based on the developed RP model, a state registration was obtained by the author for computer program No. 2023684476 titled "Software package for constructing deformation diagrams of metals under impact loading, calculated using an incremental relaxation model of plasticity" [11].

Acknowledgments

The author extends his heartfelt gratitude to Professor Yuri Viktorovich Petrov and Associate Professor Grigory Aleksandravich Volkov for their invaluable support, valuable suggestions, constant encouragement, comprehensive assistance, and extensive guidance throughout the preparation of this thesis. The author also deeply appreciates his wife, Qi Dongfang, for her unwavering love, care, long-term companionship, understanding, and encouragement in all circumstances. Furthermore, the author would like to acknowledge the support and encouragement received from the China Scholarship Council during his doctoral studies.

This thesis was financially supported by the Ministry of Science and Higher Education of the Russian Federation, agreement number No. 075-15-2022-1114. Results of chapter 2 and 4 were also supported by the Russian Science Foundation (RSF No. 22-11-00091).

Literature review

In engineering applications, accurately modeling the plastic behavior of various materials, such as metals, across a wide range of strain rates and temperatures is crucial. In finite element analysis, the J_2 plasticity model is widely accepted for a large amount of plasticity problems, with the yield function playing a key role in describing the performance of the yield surface. The yield function consists of the yield criterion and the hardening rule, which determine the yield condition and stress level of the plastic flow for each element in the object under consideration. While classical isotropic and kinematic hardening models are commonly used in the yield function, they are inadequate for capturing the dynamic behavior of materials subjected to high-rate loading and different thermal conditions. To address this limitation, additional rate-dependent and temperature-dependent components have been introduced into classical models originally developed for quasi-static cases to investigate the thermal-mechanical response of materials at high loading rates.

Strain rate effects encompass various phenomena that occur at different strain rates. Generally, these effects are characterized by an increase in stress levels as the strain rates rise. In particular, it is widely acknowledged that metals tend to exhibit higher yield stress under higher strain rates. Additionally, impact loads can sometimes result in non-monotonic stress-strain behavior, notably leading to the occurrence of the yield drop phenomenon. Conversely, elevated temperatures typically induce relaxation or softening of materials, resulting in a decrease in stress levels. This phenomenon is commonly referred to as the temperature effect.

The Split Hopkinson Pressure Bar (SHPB) technology has emerged as the one of main experimental methods for evaluating the dynamic properties of engineering materials subjected to high strain rates [12]. The SHPB test apparatus comprises essential components, including a gas gun serving as the launching system, a striker bar, an incident bar, a transmission bar, and a data acquisition system, as illustrated in figure 1 [13]. Notably, both the incident and transmission bars have identical mechanical properties.

During the experiment, a striker bar is fired by an air gun and strikes the end of the incident bar, generating an elastic pressure pulse that propagates along the incident bar. At the interface marked as ①, which connects the incident bar and the specimen, the elastic stress wave experiences partial reflection and transmission into the short specimen with a length l. Consequently, plastic deformation occurs within the specimen. Similarly, at interface ② between the specimen and the transmission bar, the stress wave also undergoes partial reflection and transmission. The choice of a "short" specimen length is deliberate to ensure uniform stress distribution within it. As a result, this experimental setup does not deal with a wave front where plastic deformation takes place due to a uniform stress distribution.

In the SHPB device, the propagation of stress waves is assumed to be one-dimensional. For a specimen of length l, the strain rate within the specimen can be expressed as

$$\dot{\varepsilon}_s = \frac{\mathrm{d}\varepsilon}{\mathrm{d}t} = \frac{v_1(t) - v_2(t)}{l}, \tag{1}$$

where $v_1(t)$ and $v_2(t)$ are the particle velocity at interfaces ① and ②, respectively. Using one-dimensional wave theory, relations between the particle velocities and the strains are $v_1 = c_0 \left(\varepsilon_I - \varepsilon_R\right)$ and $v_2 = c_0 \varepsilon_T$, where c_0 is the longitudinal wave speed in incident and transmission bars, ε_I, ε_R and ε_T denote strains caused by incident, reflected and transmission bars, respectively. Consequently, the strain rate and strain can be defined as

$$\begin{aligned} \dot{\varepsilon}_s &= \frac{\mathrm{d}\varepsilon_s}{\mathrm{d}t} = \frac{c_0 \left(\varepsilon_R + \varepsilon_T - \varepsilon_I\right)}{l}, \\ \varepsilon_s &= \frac{c_0}{l} \int_0^t \left(\varepsilon_R + \varepsilon_T - \varepsilon_I\right) \mathrm{d}t. \end{aligned} \tag{2}$$

Based on the assumption of a uniform stress field within the specimen, stress can be determined using the equation

$$\sigma_s = \frac{F_1 + F_2}{2A_s} = \frac{E_0 A_0 \left(\varepsilon_I + \varepsilon_R + \varepsilon_T\right)}{2A_s}, \tag{3}$$

where $F_1 = A_0 E_0 \left(\varepsilon_I + \varepsilon_R\right)$ and $F_2 = A_0 E_0 \varepsilon_T$ are forces on the two interfaces, E_0 and A_0 are the Young's modulus and cross-sectional area of the incident and trans-

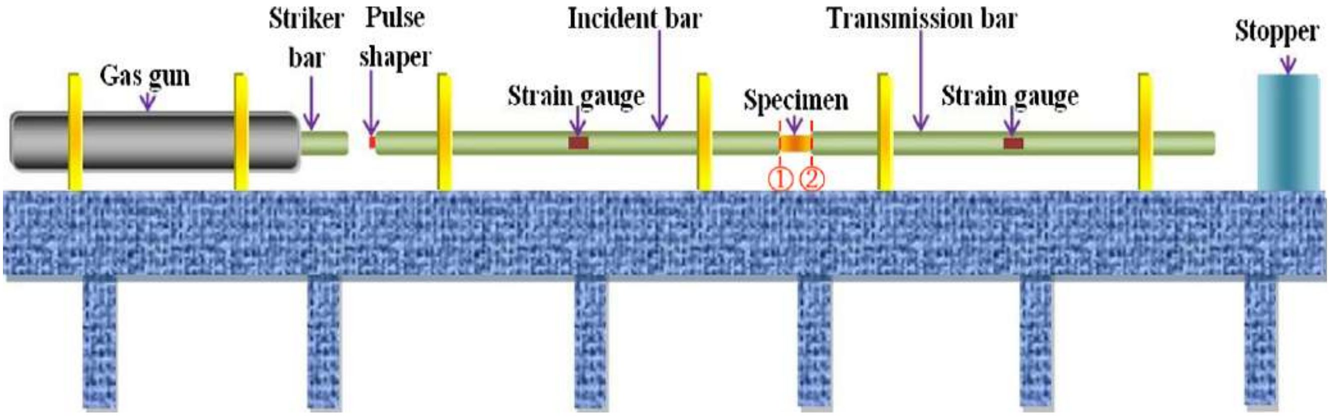

Figure 1: Schematic of the pulse shaped SHPB test apparatus, given in work [13]

mission bars, and A_s is the cross-sectional area of the specimen. The assumption of uniformity also implies the equality expressed as

$$\varepsilon_I + \varepsilon_R = \varepsilon_T \tag{4}$$

By substituting this equality into the equations for strain rate and stress, given by equations (2) and (3), respectively, the following relations are obtained to reveal the constitutive relation of tested materials

$$\varepsilon_s(t) = \frac{2c_0}{l}\int_0^t \varepsilon_R(t)\mathrm{d}t \tag{5}$$

$$\dot{\varepsilon}_s(t) = \frac{2c_0}{l}\varepsilon_R(t) \tag{6}$$

$$\sigma_s(t) = E_0\frac{A_0}{A_s}\varepsilon_T(t) \tag{7}$$

The present thesis does not encompass any experimental work. The description of the SHPB is primarily based on works by other professors cited in references [12] and [13].

Under quasi-static loading conditions, the plastic deformation process is generally isothermal and has been discussed in many works. Following the dissipation of energy produced by the irreversible deformation, materials generally strive to attain a renewed thermal balance with their surrounding media. However, the material undergoing high-rate loads is unable to achieve thermal equilibrium with the ambient environment within the deformation period. Thus, the irreversible deformation at high-loading rates is accompanied by an obvious adiabatic temperature rise [14] [15] [16] [17] [18] [19]. The thermal softening refers to the process where the stress level in materials reduces as the internal temperature increases. It is related to the stress relaxation, i.e. a reduction in the internal resistance to deformation. For some metals subjected to rapid loads, the non-monotonic relation between true stress and true strain may be observed [14], which seems to contradict the Drucker stability postulates. In fact, it just indicates a negative hardening due to thermal softening induced by the rapid plastic dissipation. To simulate the thermal softening phenomenon occurred under impact loads, different types of phenomenological constitutive models, micromechanism-based constitutive models and artificial neural network (ANN) models were developed and are further discussed in this work.

To account for the combined influence of strain rate and temperature, a strain rate-temperature correspondence is proposed. It assumes that the increased stress caused by higher strain rates can be effectively simulated by lowering the temperature. Mathematically, this relationship is expressed through the multiplicative form $\sigma = f_1(\varepsilon_p, \dot{\varepsilon}) f_2(\varepsilon_p, T)$, where f_1 represents the function capturing the strain rate effect, and f_2 represents the function accounting for the temperature effect. As for the rate-dependent multiplier, empirical formulations can be found in numerous empirical models [1] [2] [3] [4] [5]. For example, the Johnson-Cook [1] and Johnson-Holmquist models [20] incorporate the logarithmic rate-dependent component $1 + C \ln(\dot{\varepsilon}/\dot{\varepsilon}_0)$ to describe the dynamic behavior of plastic and brittle damaged materials, respectively. The Cowper-Symonds model [3] adds the power-like component $1 + (\dot{\varepsilon}/B)^{1/q}$ to the classical hardening model. Peng et al. [21] proposed a modified Johnson-Cook model that assumes an exponential relationship between the rate-dependent component and the normalized logarithmic strain rate, given by $\exp\left[C \ln\left(\dot{\varepsilon}/\dot{\varepsilon}_0\right)\right]$. Shokry suggested using the multiplier $1 + (C_1 + C_2 \varepsilon) \ln\left(\dot{\varepsilon}/\dot{\varepsilon}_0\right)$ for predicting the dynamic mechanical response of materials [22]. Zhang et al. [23] improved the Johnson-Cook model by introducing a sinusoidal strain rate strengthening coefficient as $1 + \left(C_1 + C_2 \sin\left(\frac{\ln \dot{\varepsilon} - C_3}{C_4} \pi\right)\right) \ln(\dot{\varepsilon}/\dot{\varepsilon}_0)$. In a study by Zhao et al. [24] on the dynamic mechanical response of a U75VG rail flash-butt welded joint, it was found that the aforementioned models did not accurately describe the strain rate strengthening behavior of the base metal, welding zone, and heat-affected zone at high strain rates. To address this limitation, an improved constitutive model was proposed:

$$\sigma = \left[\eta_1 A + B\left(\varepsilon_p\right)^{n_1}\right]\left[1 + \eta_2 C^{\#}\left(\frac{\dot{\varepsilon}_p}{\dot{\varepsilon}_0}\right)^{n_2}\ln\left(\frac{\dot{\varepsilon}_p}{\dot{\varepsilon}_0}\right)\right],$$

where $C^{\#}$ is the strain rate dependent material parameter. The correction coefficient η_1 reflects the relationship between strain hardening and material strength in different regions (i.e., the base metal, welding zone, and heat-affected zone). Likewise, the correction coefficient η_2 accounts for the difference in strain rate strengthening among these regions. All the models mentioned here provide a satisfactory description of rate-dependent plastic behavior for various materials and are widely used in addressing different engineering problems. However, it is important to note that these models are generally developed by assuming empirical rate-dependent and/or temperature-dependent components into existing conventional bases originally proposed for quasi-static cases.

A negative feature of these empirical models is their single model performance, which may cause difficulties in explaining many of the fundamental effects that distinguish the dynamic behavior of materials from the static one. The Johnson-Cook (JC) model [1] and its modifications [21] [22] [23] [25] are widely used models of that type. They are based on the assumption that the material behavior is a combination of strain hardening, strain rate hardening, and thermal softening. These are multiplicative-type models, and the thermal softening phenomenon is characterised by the temperature-dependent component $f_2 = 1 - \left(\frac{T-T_r}{T_m-T_r}\right)^m$, where T_m, T_r and m are materials constants. The Khan-Huang-Liang (KHL) model, initially proposed by Khan and Liang [26], aims to depict the interdependence of flow stress on the strain, strain rate, and temperature. The temperature-dependent term $\left(\frac{T_m-T}{T_m-T_r}\right)^m$ is proposed. Subsequently, Farrokh and Khan [27] enhanced the KHL model by considering the post-yield mechanical properties of ultra-fine-grained and nanocrystalline materials. Piao et al. [28] incorporated a rate-dependent thermal softening term into the Lim-Huh model [29] to account for elevated temperature effects. Omer, Butcher, and Worswick demonstrated that the generalized Voce model accurately represented the constitutive behavior of current 7000-series alloys under the temperatures and strain rates experienced during hot forming [30]. These models were developed through empirical fitting approaches based on experimental observations, and they have good agreement with experimental data at various strain rates and temperatures. Consequently, they are useful for numerical simulations, such as the finite element method, and can be conveniently determined using commercial or self-programmed constrained optimization procedures. However, these models have drawbacks, including a lack of physical basis for the model parameters and the inability to describe non-monotonic stress-strain behavior and abnormal work-hardening response. To empirically address these limitations, additional terms should be introduced into the classical basis, or other empirical functions that depend on the strain rate and/or temperature should replace the logarithm and/or power function.

Plastic deformation in metals occurs mainly by the motion of dislocations. The interaction of defects in materials with dislocations may result in obstacles to the dislocation motion. The flow stresses necessary to surmount these obstacles were separated into athermal and thermal components. The thermal component may be derived by different relations in dislocation kinetics for metals with the body-centered cubic (BCC), the face-centered cubic (FCC) and hexagonal close packed (HCP) structures. The form of the athermal component may be guided by experimental results. Hence, various versions of the constitutive models were obtained. According to Orowan's equation of the plastic strain rate and Kock's relation on the energy required for a dislocation to overcome its short-range barrier by its thermal activation, Nemat-Nasser and Isaacs [6] introduced a constitutive model for BCC metals with the physical background. Later, similar constitutive models for FCC metals [31] and HCP models [32] were discussed, and the thermal softening of the HSLA-65 steel plates at a strain rate of 3000 s^{-1} was reliably verified by experiments [14]. Referring to the activation energy expressed as $G = G_0 - \int_0^{\sigma_{\mathrm{th}}} A^* b \, d\sigma'_{\mathrm{th}}$, Zerilli and Armstrong proposed different physical-based models for metals with BCC, FCC [7] and HCP structure [33]. Voyiadjis and Abed developed microstructure-based and consistent constitutive relations to describe the flow stress of pure metals with various crystal structures for both static and dynamic applications [34] [35]. Song, Yeon, and Voyiadjis proposed a constitutive model that incorporates an additional flow stress component accounting for the hardening caused by dynamic strain aging in Martensitic Microcomposite Formable Steel alloy [36]. Voyiadjis, Song and Rusinek examined the dynamic strain aging (DSA) phenomenon and introduced the Voyiadjis-Abed-Rusinek model to address the stress increase due to the DSA phenomenon [37]. Inspired by the thermally-activated dislocation motion theory, Rusinek and Klepaczko assumed a decomposition of the total flow stress into the internal stress and the effective stress with a consideration of the the temperature-dependent evolution of Young's modulus [38]. The Rusinek-Klepaczko model is further developed in works [39] [40] etc. Based on the thermally activated depinning of dislocations from grain boundary obstacles, Khan and Liu established an Arrhenius type rate equation for ultrafine-grained/nanocrystalline FCC polycrystals [41]. Zhang, Lu, Kang et al. developed a thermodynamic model to investigate the temperature effect on the tensile behavior of the interstitial high entropy alloy, considering the kinematics of dislocation slip, deformation twinning and martensite phase transformation [42]. By employing a suitable scale-transition rule from a single crystal grain to polycrystalline aggregates, Xie, Zhu, Kang et al. introduced a crystal plasticity-based impact dynamic constitutive model [43]. Later, they proposed a thermal-activation-based dynamic constitutive model for temperature-dependent deformation of extruded AZ31B magnesium alloy, taking into account both dislocation slipping and twinning as shear movements with fixed planes and directions but differing thermodynamic features [44]. These are micromechanism-based models. They have been shown to accurately describe the thermo-mechanical behavior of different metallic materials under various loading conditions. However, it requires a detailed understanding of the material's microstructure and the interaction between dislocations, and the value of some model's parameters can be challenging to determine experimentally.

Artificial neural network (ANN) models have gained significant attention in recent studies, such as those conducted by Jia et al. [40], Ali et al. [45], Olivier et al. [46], and Xu [47], for simulating the plastic behavior of various materials. Gu, Zhang, and Golub proposed a meshless physics-informed neural networks method to solve thin-walled structural problems [48]. Li, Mohr, et al. [49] developed a machine-learning-based plasticity model capable of capturing complex rate and temperature-dependent hardening with dynamic strain aging. They also proposed a neural network-based fracture model for predicting fracture initiation. Jordan, Gorji, and Mohr [50] demonstrated that a single-hidden-layer neural network is sufficient for characterizing the hardening behavior of polypropylene. They introduced a neural-network-based viscoelastic model combined with a temperature-dependent spring to account for the immediate elastic response of the material. The backpropagation algorithm, incorporating Bayesian regularization, was employed to identify an appropriate neural network function. In our current work, we have found that a single-hidden-layer artificial neural network is more suitable for our specific needs compared to other more complex structures, which are determined by the inherent characteristics of neural networks. Additionally, we discuss the main differences between ANN models and constitutive models, including phenomenological and physically-based models.

The rate-dependent constitutive response of plastics and metals has been investigated by Cristescu [51] and Lubliner [52], who introduced a quasi-linear differential equation. They proposed a function that describes the non-instantaneous plastic response. Another approach to address the non-instantaneous material response is the integral approach. Cotrell and Bilby's dislocation theory [53] states that the time required to release dislocations is proportional to $\exp\left(\frac{U(\sigma/\sigma_0))}{kT}\right)$, where T represents the absolute temperature, σ_0 is the yield limit at temperature $T = 0, K$, k is Boltzmann's constant, U is the energy of activation, and σ is the applied stress. By assuming that the plastic process begins when the dislocation density reaches a certain critical value, Campbell derived a dynamic yield criterion in the form of an integral equation:

$$\int_0^{t_y} \left(\frac{\sigma(t)}{\sigma_0}\right)^{\alpha} dt = C, \tag{8}$$

Here, t_y represents the starting time of the plastic process, α is a constant that may vary with temperature, and C is a constant with units of time. Campbell's criterion is considered convenient and applicable for arbitrary impact loading histories [54]. Moreover, Klepaczko [55], Stolarski [56], and Jankowiak [57] have found it suitable for use as a dynamic fracture criterion, referred to as the cumulative fracture criterion, by substituting fracture parameters for t_y and σ_0. Tuler and Butcher proposed a similar integral fracture criterion [58] based on the concepts of cumulative damage and overstress. These integral criteria have been shown to effectively describe yield and fracture conditions at high loading rates. However, it should be noted that they contradict the quasi-static conditions of plasticity and fracture, where $\sigma(t_c) = \sigma_c$, with σ_c representing the static yield stress or static critical strength.

New perspectives on modeling the dynamic response of the materials can be associated with the structural-temporal approach, which was initially proposed by

Petrov and Utkin [59] and Petrov and Morozov[60] and Petrov [61] in the field of fracture dynamics. The approach is based on the notion of the incubation time of the fracture process and suggests that, in cases of low-rate loading, it can be reduced to classical models by ignoring insignificant components. Instead of using an empirical rate-dependent component, the approach introduces an incubation time constant, denoted by τ, into a time integral. The parameter τ characterizes the time sensitivity of materials and has a sense of the characteristic period of relaxation processes. The relaxation nature of the incubation time was mentioned in works [62] [63]. To account for dynamic rock fracture, Xu et al. [64] used a modified incubation time criterion with a contribution weight factor containing the incubation characteristic time and discussed the viscosity analogy of microcrack kinematics. The contribution weight factor can actually be regarded as the kernel $K'(t) = \frac{1}{\tau}e^{-\frac{t}{\tau}}$ of an integral operator $\int_0^t K'(t-s)\sigma(s)\,\mathrm{d}s$, while original incubation time criterion uses the kernel $K(t) = \frac{1}{\tau}H(\tau - t)$, where $H(\cdot)$ is the Heaviside function, as a linear approximation of $K'(t)$ [62]. Petrov and Gruzdkov proposed an integral criterion of plasticity [8], which was inspired by the structural-temporal approach [59] [60] [61] and Campbell's criterion (8) [54]. Applicable to arbitrary loading forms [65] [66], Petrov's integral criterion [67] [68] discussed later in section 2.1.1 furnishes a unified depiction of both quasi-static and dynamic yield conditions using merely a limited parameter set.

An irreversible deformation and corresponding stress-strain relationships can be described by the relaxation model of plasticity (RP model) first introduced by Petrov and his group [69] [70] [71]. The RP model considers plastic deformation as a relaxation process, where stresses caused by loads are released with time due to the motion of defects in the crystal lattice. The RP model proposes a dimensionless relaxation function to describe the relaxation nature of plasticity and is derived from the incubation time concept, without the empirically proposed rate-dependent component. The RP model has been demonstrated to effectively simulate both the strain-rate effect and the yield point phenomenon across a broad range of strain rates [70] [71]. However, the RP model has a limited ability to describe work-hardening response over a wide strain range. The incubation time, reflecting the time sensitivity of materials, is a characteristic time of the relaxation process of microscopic events. The softening of materials, as a relaxation event, is significantly affected by temperature. Higher temperatures can cause more noticeable softening, leading to a decrease in its characteristic time. This temperature-time correspondence can be mathematically summarised through the temperature dependence of the incubation time parameter. Previous studies, such as [9] and [10], have discussed some temperature-time dependences. However, they were performed within a limited range of strain and strain rate, and the adiabatic temperature rise appeared under impact loading was not considered. Additionally, the impact of temperature on the elastic properties of the materials studied was not considered, which could influence the incubation time measurement. In contrast to the previous researches, we examines the temperature-time correspondence by introducing the relative stress (RS) factor over a wide range of strain, strain rate and temperature. In addition, a possible explanation for the existence of different proposed phenomenological temperature-time correspondences are discussed. We also describe the non-monotonic stress-strain diagram, i.e. the negative hardening, due to thermal softening induced by the adiabatic plastic deformation under high-rate loading conditions. Furthermore, the incubation time approach considers the strain-rate sensitivity as a manifestation of the time sensitivity of materials. The time-dependent yield surface equation in the incubation time approach is essential for further development of this theory. Therefore, in this work, we introduce the framework of the modified RP model and explore the role of the relaxation function $\gamma(t)$, as well as the relationship between the modified RP model and the time-dependent yield surface equation.

Chapter 1

Existing models for dynamic plasticity

In this chapter, some widely used models describing the strain rate effects and thermal softening phenomenon, including phenomenological, dislocation-mechanics-based constitutive models and the ANN model, are briefly introduced.

Discussion presented in the chapter is published in paper [72].

1.1 A basic background

The strain rate sensitivity of materials can be effectively examined through SPHB experiments [73]. In these experiments, the material is subjected to high strain rates while being maintained in a state of dynamic equilibrium. During deformation, the material experiences either an isothermal or adiabatic condition. Thus, we will focus on the elasto-plastic behavior of isotropic metallic materials under monotonic loads and neglect heat transfer. This behavior is described by Hook's law (1.1), the plastic flow rule $\dot{\boldsymbol{\varepsilon}}^p = \gamma \frac{\partial \Phi(\boldsymbol{\sigma})}{\partial \boldsymbol{\sigma}}, \forall \boldsymbol{\sigma} : f(\boldsymbol{\sigma}, \mathbf{q}) \leqslant 0$ and the yield surface equation $f(\boldsymbol{\sigma}, \mathbf{q}) = 0$, where $\boldsymbol{\sigma}$ is the Cauchy stress tensor (true stress tensor), $\mathbf{C}$ is the fourth-order tensor of the elastic moduli, $\boldsymbol{\varepsilon}^e$ and $\boldsymbol{\varepsilon}^p$ are the elastic strain tensor and plastic strain tensor, respectively, γ is a scalar multiplier function, $\Phi(\boldsymbol{\sigma})$ represents the plastic flow potential. The internal variables $\mathbf{q}$ are generally considered the functions of the plastic strain tensor $\boldsymbol{\varepsilon}^p$ and a set of hardening parameters. We consider the isotropic J_2 plasticity problem, i.e. the case with an isotropic von-Mises yield surface (1.4), where $\bar{\sigma}(\mathbf{s}) = (\frac{3}{2}\mathbf{s} : \mathbf{s})^{1/2}$ represents the shear stress intensity, $\mathbf{s}$ is the stress deviator tensor. The hardening function $\sigma^y\left(\bar{\varepsilon}^p, \dot{\bar{\varepsilon}}^p, T\right)$ can be established by pure tension or compression tests in the one-dimensional statement. The equivalent plastic strain is determined by $\bar{\varepsilon}^p = \int_0^t \dot{\bar{\varepsilon}}^p dt'$ and $\dot{\bar{\varepsilon}}^p = \left(\frac{2}{3}\dot{\boldsymbol{\varepsilon}}^p : \dot{\boldsymbol{\varepsilon}}^p\right)^{\frac{1}{2}}$.

The hardening behavior of materials generally conforms to Drucker's stability postulate (1.5), which implies that the normality (or convexity) rule for the yield surface holds at different strain rates. Furthermore, these materials also satisfy the principle of maximum plastic dissipation, indicating the validity of the associated flow rule (1.2) ($\Phi(\cdot) = f(\cdot)$). However, in certain cases, such as under impact loads [14], hardening materials may exhibit softening behavior, seemingly contrary to Drucker's postulate and the associated flow rule. This specific response, characterized by negative hardening at high strain rates, can be attributed to thermal softening caused by adiabatic temperature rise (or rapid plastic dissipation). To describe this thermal softening phenomenon resulting from impact loads, equation (1.3) provides an explanation. Here, ρ is the mass density, C_ν refers to the temperature-dependent heat capacity and η is the Taylor–Quinney coefficient. Typically, η is evaluated experimentally by measuring the temperature rise of a specimen during plastic deformation.

In this work, we consider the isotropic J_2 dynamic plasticity problem. This problem is characterized by a set of constitutive relations represented by equations (1.1) to (1.4), where the one-dimensional hardening function $\sigma^y\left(\bar{\varepsilon}^p, \dot{\bar{\varepsilon}}^p, T\right)$ is rate-dependent and has been developed by different scientific groups. To investigate the behavior of materials under dynamic loading conditions, several approaches have been proposed in the literature. In the following sections, we will discuss empirical models, dislocation-mechanics-based models, and artificial neural network models. These models can serve as potential options for representing the rate-dependent hardening function $\sigma^y\left(\bar{\varepsilon}^p, \dot{\bar{\varepsilon}}^p, T\right)$. By analyzing their strengths and limitations, we aim to provide insights into the applicability of a new approach in capturing the complex behavior of materials during plastic deformation.

$$\dot{\boldsymbol{\sigma}} = \mathbf{C} : \dot{\boldsymbol{\varepsilon}}^e, \mathbf{C} = K\mathbf{I} \otimes \mathbf{I} - 2G\left(\mathbf{E} - \frac{1}{3}\mathbf{I} \otimes \mathbf{I}\right) \tag{1.1}$$

$$\dot{\boldsymbol{\varepsilon}}^p = \gamma \mathbf{n}, \, \mathbf{n} = \frac{\mathbf{s}}{(\mathbf{s} : \mathbf{s})^{\frac{1}{2}}} = \frac{\mathbf{s}}{|\mathbf{s}|} \tag{1.2}$$

$$\dot{T} = \frac{\eta(\dot{\bar{\varepsilon}}^p)}{\rho C_v} \boldsymbol{\sigma} : \dot{\boldsymbol{\varepsilon}}^p \tag{1.3}$$

$$f\left(\boldsymbol{\sigma}, \bar{\varepsilon}^p, \dot{\bar{\varepsilon}}^p, T\right) = \bar{\sigma}(\mathbf{s}) - \sigma^y\left(\bar{\varepsilon}^p, \dot{\bar{\varepsilon}}^p, T\right) = 0,\ \bar{\sigma}(\mathbf{s}) = \left(\frac{3}{2}\mathbf{s} : \mathbf{s}\right)^{\frac{1}{2}} \tag{1.4}$$

$$\int_0^t \left(\boldsymbol{\sigma}(\boldsymbol{\varepsilon}(s)) - \boldsymbol{\sigma}'\right) : \dot{\boldsymbol{\varepsilon}}(s) ds \geqslant 0 \tag{1.5}$$

1.2 Empirical models

1.2.1 The Johnson-Cook model

The Johnson-Cook (JC) model [1] is one of the most influential phenomenological constitutive models for simulating the plastic response at different strain rates and temperatures. The model is given as follows

$$\sigma = \left(A + B\varepsilon_p^n\right)\left(1 + C\ln\left(\frac{\dot{\varepsilon}}{\dot{\varepsilon_0}}\right)\right)\left(1 - \left(\frac{T - T_r}{T_m - T_r}\right)^m\right). \tag{1.6}$$

In the JC model (1.6), σ is the von Mises stress ($\bar{\sigma}(\mathbf{s})$), ε_p is the equivalent plastic strain, $\dot{\varepsilon}$ is the strain rate, $\dot{\varepsilon_0}$ is the reference strain rate, T_m is the melting temperature and T_r is the reference temperature. A, B, n, C, m are model parameters.

This model is proposed by the direct empirical approach, based on experimental analysis. It is implemented in a large number of commercial finite element (FE) packages, and this provides significant convenience for modeling the thermo-mechanical response of different materials. However, it may not give relatively accurate results over a wide range of strain rates and temperatures.

1.2.2 The Khan-Huang-Liang model

The Khan-Huang-Liang (KHL) model was proposed by Khan and Liang [26] to describe the coupled work hardening dependence of flow stress on the strain, strain rate, and temperature. Later, it was modified to have closer predictions to the observed response [74]. The widely used KHL model is presented in the equation (1.7). Here, A, B, n_0, n_1, c, and m are model parameters; T_r is the reference temperature; T_m is the melting temperature; D_0 is the arbitrarily chosen upper bound of the strain rate; $\dot{\varepsilon}_0$ is the reference strain rate and generally chosen as 1

s^{-1}.

$$\sigma = \left\{ A + B \left[\left(1 - \frac{\ln \dot{\varepsilon}}{\ln D_0} \right) \right]^{n_1} \varepsilon_p^{n_0} \right\} \left(\frac{\dot{\varepsilon}}{\dot{\varepsilon}_0} \right)^c \left(\frac{T_m - T}{T_m - T_r} \right)^m \tag{1.7}$$

1.3 Dislocation-mechanics-based models

Another class of constitutive models refer to the dislocation-mechanics-based models. One of main factors affecting the plastic deformation is the motion of dislocations. The interaction of defects in materials with dislocations may result in obstacles to the dislocation motion. Forest dislocations, point defects, alloy elements, solution atoms, impurities, deposits, etc. can cause short-range obstacles; grain boundaries, far-field dislocation forests, and other microstructural elements with far-field influence may generate long-range obstacles. The flow stresses σ necessary to surmount these obstacles are reasonable to be separated into two components given in the expression (1.8). The athermal component σ_{ath} characterizes the long-range obstacles, which are believed temperature-insensitive. The thermal component σ_{th} mainly reflects the short-range obstacles overcome by the action of thermal activation.

$$\sigma = \sigma_{\text{ath}} + \sigma_{\text{th}} \tag{1.8}$$

The thermal component σ_{th} may be derived by different relations in dislocation kinetics, and the form of the athermal component σ_{ath} may be guided by experimental results. Hence, various versions of the constitutive models can be obtained.

1.3.1 The Nemat-Nasser's models

Nemat-Nasser and Isaacs [6] introduced a constitutive model with the physical background. Assuming the dependence of the athermal stress component on the dislocation density, they proposed a simple power-law representation shown below as a first approximation

$$\sigma_{\text{ath}} = a\varepsilon_p^n, \tag{1.9}$$

where ε_p is the equivalent plastic strain. a and n are model parameters. According to Orowan's equation of the plastic strain rate and Kock's relation on the energy required for a dislocation to overcome its short-range barrier by its thermal activation, the thermal part of flow stress σ_{th} is given as

$$\sigma_{\text{th}} = \sigma_0 \left[1 - \left(-\frac{kT}{G_0}\ln\frac{\dot{\varepsilon}}{\dot{\varepsilon}_0}\right)^{1/q}\right]^{1/p} H\left(1 + \frac{kT}{G_0}\ln\frac{\dot{\varepsilon}}{\dot{\varepsilon}_0}\right), \tag{1.10}$$

where σ_0 is the threshold stress above which the barrier is crossed by a dislocation without any assistance from thermal activation, and $\dot{\varepsilon}_0$ is regarded as a reference strain rate that characterizes the strain rate sensitivity and the parameter k/G_0 represents the temperature sensitivity of the material (k is the Boltzmann constant). The function $H(\cdot)$ is the Heaviside function. Parameters $0 < p \leqslant 1$ and $1 \leqslant q \leqslant 2$ define the profile of the short-range obstacles.

For metals with a BCC structure, the Peierls barriers are the main resistance to the dislocation motion, and the average dislocation spacing l may be denoted a certain constant. Thus, it is concluded that $\sigma_0 = \sigma_0(l)$ can be a material constant [6][14]. Consequently, the Nemat-Nasser-Isaacs (NNI) model can be written as

$$\sigma = a\varepsilon_p^n + \sigma_0 \left[1 - \left(-\frac{kT}{G_0}\ln\frac{\dot{\varepsilon}}{\dot{\varepsilon}_0}\right)^{1/q}\right]^{1/p} H\left(1 + \frac{kT}{G_0}\ln\frac{\dot{\varepsilon}}{\dot{\varepsilon}_0}\right). \tag{1.11}$$

In the NNI model (1.11), parameters $a, n, \sigma_0, k/G_0, \dot{\varepsilon}_0, q,$ and p are required to be determined.

For metals with a FCC structure, the Peierls barriers restrict the dislocation motion only at very low temperatures, and the dislocation forests which intersect the slip planes are the essential barriers for dislocations lying on the slip planes. Hence, the dislocation-density-dependent average spacing l, as well as the $\sigma_0(l)$, should be the function of the plastic strain ε_p and temperature T. Assuming $l \sim (1 + a_0(1 - (T/T_m)^2)\varepsilon_p^{n_0})^{-1}$, Nemat-Nasser and Li [31] proposed the NNL model as follows

$$\begin{gathered}\sigma = a\varepsilon_p^n + \sigma_0 f(\varepsilon_p, T)\left[1 - \left(-\tfrac{kT}{G_0}\ln\tfrac{\dot{\varepsilon} f(\varepsilon_p,T)}{\dot{\varepsilon}_0}\right)^{1/q}\right]^{1/p} H\left(1 + \tfrac{kT}{G_0}\ln\tfrac{\dot{\varepsilon} f(\varepsilon_p,T)}{\dot{\varepsilon}_0}\right), \\ f(\varepsilon_p, T) = 1 + a_0\left[1 - \left(\tfrac{T}{T_{\text{m}}}\right)^2\right]\varepsilon_p^{n_0}.\end{gathered} \tag{1.12}$$

In the NNL model (1.12), the parameters $a, n, \sigma_0, k/G_0, \dot{\varepsilon}_0, q, p, a_0, T_m,$ and n_0 are required to be established. T_m is the melting temperature. For OFHC Cu, the parameter n_0 is taken as $\frac{1}{2}$.

The NNL model was also implemented to Ti-6Al-4V with HCP structure, considering $n_0 = 1$ [32].

1.3.2 The Zerilli-Armstrong models

Referring to the activation energy expressed as $G = G_0 - \int_0^{\sigma_{\text{th}}} A^* b \, d\sigma'_{\text{th}}$, Zerilli and Armstrong proposed different physical-based models for metals with BCC, FCC [7] and HCP structure [33].

For BCC metals, where the Peierls stress is responsible for the thermal activation, the area of activation A^* is considered essentially independent of plastic strain ε_p. Consequently, the thermal component σ_{th} can be written without regard for the strain as follows

$$\sigma_{\text{th}} = B \exp\left(-\beta_0 T + \beta_1 T \ln \dot{\varepsilon}\right). \tag{1.13}$$

The final constitutive model can be presented in the form (1.14). The first term is the athermal component; the second term arises from a thermal activation analysis of the Peierls stress interactions; the third term exhibits a continual work hardening without saturation of flow stress at a large strain [75].

$$\sigma = \sigma_a + B \exp\left(-\beta_0 T + \beta_1 T \ln \dot{\varepsilon}\right) + B_0 \varepsilon_p^{n_0} \tag{1.14}$$

For FCC metals, where the intersection of dislocations is the main mechanism for the thermal activation behavior, the area of activation is believed to be dependent of plastic strain ε_p. The thermal component differs from that in (1.13) and has an additional multiplier $\varepsilon_p^{1/2}$. Then, the FCC model takes the form (1.15).

$$\sigma = \sigma_a + B \varepsilon_p^{1/2} \exp\left(-\beta_0 T + \beta_1 T \ln \dot{\varepsilon}\right) \tag{1.15}$$

For HCP metals, the final constitutive model is supposed to be

$$\sigma = \sigma_a + B \exp\left(-\beta_0 T + \beta_1 T \ln \dot{\varepsilon}\right) + B_0 \varepsilon_p^{1/2} \exp\left(-\alpha_0 T + \alpha_1 T \ln \dot{\varepsilon}\right). \tag{1.16}$$

In the above Zerilli-Armstrong models, the parameters $\sigma_a, B, B_0, \beta_0, \beta_1, \alpha_0, \alpha_1, n_0$ may need to be determined, depending on the structure type of considered metals.

1.4 Artificial Neural Network model

Artificial neural network (ANN) algorithms were mainly examined as solutions to approximation problems. The task of learning a mapping between an input and an output space can be viewed as the problem of creating an associative "memory" that finds the correct output when given the input and generalizes its output when presented with new inputs [76]. The classical approximation approach assumes a linear dependence of a suitable basis of functions $\Phi_i(\mathbf{x})$ of its vector argument $\mathbf{x}$ as follows, where $\mathbf{w}$ represents the weight coefficient vector with components w_i and repeated index i follows the Einstein summation convention.

$$F(\mathbf{w}, \mathbf{x}) = w_i \, \Phi_i(\mathbf{x}). \tag{1.17}$$

Spline interpolation and many approximation approaches, such as expansions in a series of orthogonal polynomials, belong to representation (1.17). Neural Network approach suggests a composition of functions, such as the active function $f(\cdot)$ and regression relations, to approximate needed functions, as shown in expression (1.18). This approach implies a multilayer network of units that sum their inputs with weight coefficients $w_1, ..., w_n, v_1, ..., v_i, u_1, ..., u_j$.

$$F(\mathbf{W}, \mathbf{x}) = \sum_n w_n f\left(\sum_i v_i f\left(\dots f\left(\sum_j u_j x_j\right)\dots\right)\right) \tag{1.18}$$

Machine learning algorithms, as an approximation (or hypersurface reconstruction) approach, are able to approximate constitutive models as functions of arguments $\varepsilon_p, \dot{\varepsilon}$, and T, i.e. $\sigma = F(\varepsilon_p, \dot{\varepsilon}, T)$. In this paper, we consider an ANN model with a sigmoid active function (1.20) and a linear regression relation (1.21) with a weight matrix $\mathbf{W}$ and a bias vector $\mathbf{b}$. The sigmoid function is monotonic and varies within the range $(0, 1)$. A normalization (or non-dimentionlisation) of arguments (or inputs) are performed by expression (1.22), where $[\cdot]_{\min}$ and $[\cdot]_{\max}$ are the lower and upper boundaries of the corresponding field. For an ANN model with N hidden layers, the function $\sigma = F(\mathbf{x})$ is approximated by relation (1.19). Technically, $\mathbf{W}^{(k)}$ and $\mathbf{b}^{(k)}$ are the weight matrix and bias vector of the k-th hidden layer. The component ${w_{ij}}^{(k)}$ of weight matrix $\mathbf{W}^{(k)}$ represents the associated weight parameter between the ith neuron of hidden layer k and the jth neuron of the hidden layer $(k-1)$. The dimension $n \times m$ of $\mathbf{W}^{(k)}$ corresponds to m neurons of the hidden layer $(k-1)$ and n neurons of hidden layer k. The hyper-parameters required to be predetermined are often referred to the total number of hidden layers, the number of neurons per hidden layer, and the activation function [77]. Values of "build-in" parameters including weight coefficients ${w_{ij}}^{(k)}$, components ${b_i}^{(k)}$ of bias vectors, components w_{0i} of the weight vector $\mathbf{w}_0$, and scalar parameter b_0 are determined by "learning" a given dataset, i.e. fitting the model to the dataset via an optimization algorithm. Gradient descent (GD) is a conventional optimization algorithm utilised in machine learning [78]. It operates by moving against the gradient at a predetermined rate controlled by the learning rate α to identify the extreme value point or the optimal parameter. However, traditional gradient descent very easily falls into the local optimal solution in the process of finding the extreme value, therefore, to increase the possibility of finding the global optimal solution, we choose stochastic gradient descent (SGD) [79] as the optimizer for neural network training. It follows the same way as GD in updating the model parameters, except that it adds randomness to the descent process, thus increasing the probability of finding the global optimal solution. The neural network architecture and the model inference[1] process with one hidden layer ($N=1$) and n neurons are shown in figure 1.1.

$$\begin{aligned}
\mathbf{y}^{(1)} &= \mathbf{W}^{(1)}\,\mathbf{x} + \mathbf{b}^{(1)}, \\
\mathbf{y}^{(k)} &= \mathbf{W}^{(k)}\,f\left(\mathbf{y}^{(k-1)}\right) + \mathbf{b}^{(k)}, k = 2...N \\
\sigma &= \mathbf{w}_0 \cdot f\left(\mathbf{y}^{(N)}\right) + b_0
\end{aligned} \tag{1.19}$$

In this thesis, we discuss an ANN model using a sigmoid active function (1.20) and a linear regression relation (1.21) with a weight matrix $\mathbf{W}$ and a bias vector $\mathbf{b}$.

$$f(\mathbf{x}) = \frac{1}{1+e^{-\mathbf{x}}} \tag{1.20}$$

$$\mathbf{y} = \mathbf{W}\,\mathbf{x} + \mathbf{b} \tag{1.21}$$

---

[1] The process of inputting unknown data into the model and outputting results through the calculation of the model is called model inference in the field of artificial intelligence.

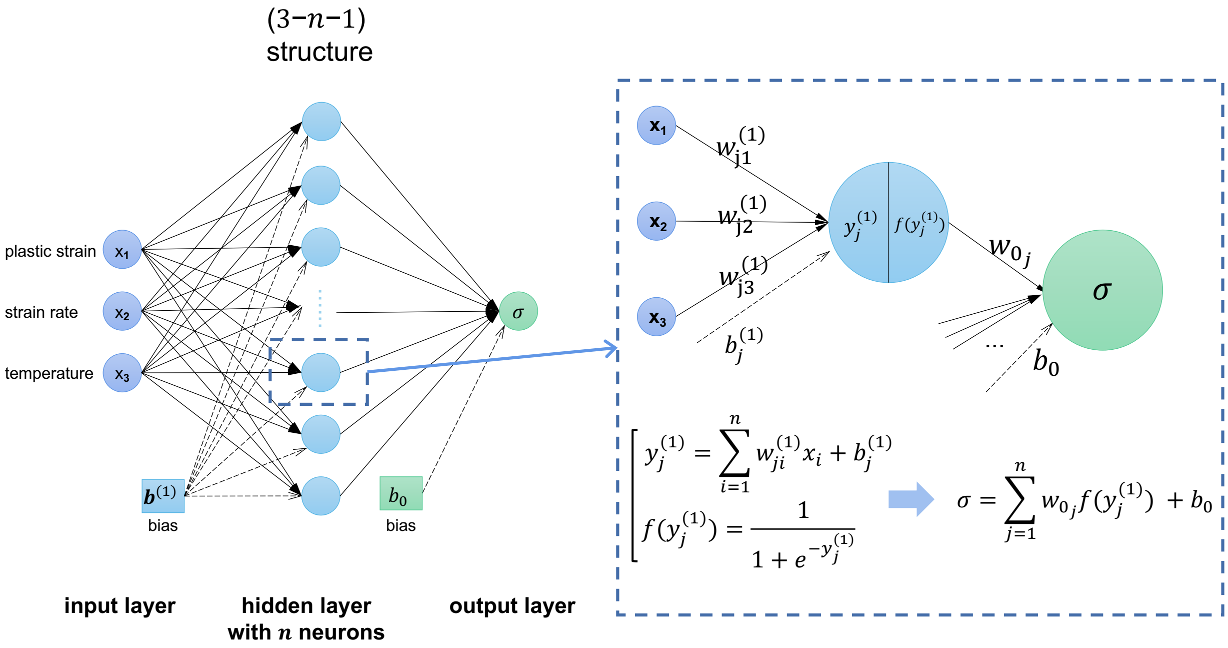

Figure 1.1: The architecture of the Neural Network model with 3-n-1 structure. Left: the global architecture of the model. Right: details of jth neuron and output layer. Three features (x_1, x_2, x_3) are contained in the input layer. The only hidden layer consists of n neurons, each of which includes the weight parameter vector $\left({w_{j1}}^{(1)}, {w_{j2}}^{(1)}, {w_{j3}}^{(1)}\right)$, the bias parameter ${b_j}^{(1)}$ and the sigmoid activation function $f(\cdot)$. The entire hidden layer then carries a weight matrix $\mathbf{W}^{(1)}$ with $n \times 3$ components ${w_{ji}}^{(1)}$ and bias vector $\mathbf{b}^{(\mathbf{1})}$ with n components ${b_j}^{(1)}$. Finally, the original 3 features are mapped to n implicit features ${y_j}^{(1)}$, which are transformed by hidden layer into a one-dimensional output σ using the weight parameter vector $\mathbf{w_0}$ and the bias parameter b_0.

$$
\begin{aligned}
x_1 &= \frac{\varepsilon^p - [\varepsilon^p]_{\min}}{[\varepsilon^p]_{\max} - [\dot{\varepsilon}^p]_{\min}} \\
x_2 &= \frac{\dot{\varepsilon} - [\dot{\varepsilon}]_{\min}}{[\dot{\varepsilon}]_{\max} - [\dot{\varepsilon}]_{\min}} \\
x_3 &= \frac{T - [T]_{\min}}{[T]_{\max} - [T]_{\min}}
\end{aligned}
\tag{1.22}
$$

Chapter 2

Relaxation model of plasticity and temperature-time correspondence

The study of dynamic yield phenomena has been the subject of numerous works [73] [80] [81] [82] [83]. Campbell derived a dynamic yield criterion in integral form (8), based on Cotrell's and Bilby's dislocation theory [53]. However, this criterion contradicts the quasi-static yield and fracture criteria $\sigma(t_c) = \sigma_c$, where σ_c represents either the static yield stress or the static critical strength. In light of this contradiction, Petrov and Gruzdkov proposed an integral yield criterion that incorporates an incubation time parameter τ and aligns with both static and dynamic experimental results [8]. Based on incubation time approach, Petrov's group proposed a relaxation model of plasticity and the temperature-time correspondence, which are discussed and developed in this work.

Results presented in the chapter are published in papers [72] [84] [85]

2.1 Development of the relaxation model of plasticity

2.1.1 Incubation time criterion of dynamic plasticity

The integral yield criterion proposed by Petrov and his group is expressed as follows:

$$I(t) = \frac{1}{\tau}\int_{t-\tau}^{t} \left(\frac{\sigma(s)}{\sigma_y}\right)^{\alpha} ds \leqslant 1, \tag{2.1}$$

where τ denotes the incubation time (or characteristic time), σ_y is the static yield stress, α is a dimensionless parameter (typically $\alpha \geqslant 1$). The incubation time τ characterizes the temporal or strain rate sensitivity of materials, while α reflects the material's sensitivity to the intensity level (amplitude) of local stress. Criterion (2.1) closely approximates the static yield condition $\sigma(t) \leqslant \sigma_y$ when the loading duration significantly exceeds the incubation time τ. In cases of impact loading, where the loading duration is comparable to or less than the incubation time, criterion (2.1) bears similarity to Campbell's criterion (8). This advantageous feature of criterion (2.1) permits a unified description of both quasi-static and dynamic yield conditions, rendering it suitable for investigating the strain-rate effect observed in numerous experiments.

According to inequality (2.1), the plastic process initiates only when $I(t_y) = 1$ occurs. For constant strain rate loading (i.e., $\sigma(t) = E\dot{\varepsilon}tH(t)$ where $H(t)$ denotes the Heaviside function), the relationship between the rate-dependent yield stress $\sigma_{dy} = \sigma(t_y)$ and the strain rate $\dot{\varepsilon}$ can be determined by equation (2.2) derived from (2.1) (see appendix A).

$$\sigma_{dy}^{1+\alpha} - (\sigma_{dy} - E\dot{\varepsilon}\tau)^{1+\alpha} H(\sigma_{dy} - E\dot{\varepsilon}\tau) = (1+\alpha)(E\dot{\varepsilon}\tau)\sigma_y^{\alpha}, \tag{2.2}$$

or by the following equivalent equations (2.3)

$$\begin{cases} \sigma_{dy}^{1+\alpha} - (\sigma_{dy} - E\dot{\varepsilon}\tau)^{1+\alpha} = (1+\alpha)(E\dot{\varepsilon}\tau)\sigma_y^{\alpha}, & \dot{\varepsilon} \leqslant \frac{\sigma_y(1+\alpha)^{\frac{1}{\alpha}}}{E\tau}; \\ \sigma_{dy} = \left((1+\alpha)(E\dot{\varepsilon}\tau)\sigma_y^{\alpha}\right)^{\frac{1}{1+\alpha}}, & \dot{\varepsilon} > \frac{\sigma_y(1+\alpha)^{\frac{1}{\alpha}}}{E\tau}. \end{cases} \tag{2.3}$$

For "rapid" loading, defined as $\dot{\varepsilon} > \frac{\sigma_y(1+\alpha)^{\frac{1}{\alpha}}}{E\tau}$, the yield stress has a simple and clear dependence on the strain rate as shown in equation (2.3). In contrast, for relatively "slow" loading where $\dot{\varepsilon} \leqslant \frac{\sigma_y(1+\alpha)^{\frac{1}{\alpha}}}{E\tau}$, the relationship is slightly more complex and can be solved using various numerical iteration methods.

Criterion (2.1) boasts several advantages: it is applicable to arbitrary loading forms, it provides a unified description of both quasi-static and dynamic yield conditions, and it determines the yield condition based on only a limited set of material constants (τ, α, σ_y). Moreover, it enables further investigations into the strain-rate effect, yield drop phenomenon, and work-hardening response, as detailed below.

2.1.2 Original relaxation model of plasticity

The relaxation model of plasticity (RP model), originally introduced by Petrov and his group [69] [71] [86] [70], allows for the prediction of the unstable behavior in the stress-strain relationship. In the original RP model, a dimensionless relaxation function $\gamma(t)$ is introduced, satisfying the identity (2.4) during the plastic stage $(t \geqslant t_y)$

$$\frac{1}{\tau}\int_{t-\tau}^{t}\left(\frac{\gamma(t)\Sigma(s)}{\sigma_y}\right)^{\alpha} ds \equiv 1, \tag{2.4}$$

where $\Sigma(t) = E\varepsilon(t)H(t)$ represents the elastic predictor of true stress. Consequently, $\gamma(t)$ varies within the interval $(0, 1]$ and is uniquely determined by the condition (2.5) derived from equation (2.4), with $I(t) = \frac{1}{\tau}\int_{t-\tau}^{t}(\Sigma(s)/\sigma_y)^{\alpha} ds$.

$$\gamma(t) = \begin{cases} 1, I(t) < 1 \\ I(t)^{-1/\alpha}, I(t) \geqslant 1 \end{cases} \tag{2.5}$$

In equation (2.5), the equality $\gamma(t) = 1$ corresponds to the accumulation of elastic deformation, while the gradual decrease in the relaxation function within the range $0 < \gamma(t) < 1$ signifies the material's transition into the plastic deformation stage. The stress-strain relationship is established by expression (2.6), where β represents the hardening parameter $(0 \leqslant \beta < 1)$ and the case $\beta = 0$ corresponds to perfect plasticity.

$$\sigma(t) = \Sigma(t)\gamma(t)^{1-\beta} = E\gamma(t)^{1-\beta}\varepsilon(t). \tag{2.6}$$

In the original RP model (2.4)-(2.6), all three parameters τ, α, β are assumed to remain invariant throughout the loading history, relying solely on structural transformations within the material. Consequently, a limited set of parameters (τ, α, β) can be used to simulate various stress-strain curves across a wide range of strain rates [87].

The original RP model (2.4)-(2.6) has been successfully employed to simulate strain-rate effects and yield drop phenomena within a broad range of strain rates [71] [86] [70]. However, the hardening parameter β assumed as a power of the relaxation function $\gamma(t)$ could limit the model's ability to describe work-hardening effects, and this is discussed in more detail in section 2.1.3. While the original RP model reliably characterizes and predicts the stress-strain behavior of certain materials within the strain range near the yield point (at the early stage of plasticity), it overlooks the influence of developed plastic deformation on subsequent plastic performance. These aspects may account for some deviations observed between model descriptions and experimental stress-strain curves during the hardening stage of plastic flow. Thus, a modification of the original RP model is necessary.

2.1.3 Framework of the modified relaxation model of plasticity

Dynamic stress intensity

In this work, we investigate the dynamic stress intensity derived from the integral dynamic yield criterion (2.1). To understand the difference and connection between the new dynamic stress intensity and the classical quasi-static shear stress intensity $\bar{\sigma}$ (the equivalent von Mises stress given in expression (2.7)), it is essential to explain Novozhilov's concept of the shear stress intensity (SSI). Novozhilov demonstrated in a spherical coordinate system that the SSI is a limit value obtained by taking an integral average (or the root mean square, the quadratic mean) of shear stresses σ_τ over the entire spherical surface Ω enclosing the point under consideration. This expression is given in equation (2.8), where r represents the radius of the sphere, $d\Omega$ denotes the area of an infinitesimal plane on the spherical surface Ω, and σ_τ represents the shear stress at that specific point on the plane $d\Omega$. For further details, refer to appendix B. In the classical theory of plasticity, the yield criterion is assumed to be

$$\bar{\sigma}(\mathbf{s}) \leqslant \sigma_y,$$

where $\mathbf{s}$ is the stress deviator tensor.

$$\bar{\sigma}(\mathbf{s}) = \sqrt{\frac{3}{2}\mathbf{s} : \mathbf{s}} = \sqrt{\frac{1}{2}\left[(\sigma_1 - \sigma_2)^2 + (\sigma_2 - \sigma_3)^2 + (\sigma_3 - \sigma_1)^2\right]} \tag{2.7}$$

$$\bar{\sigma} = \sqrt{\frac{15}{2}} \lim_{r \to 0} \left(\frac{1}{\Omega} \iint \sigma_\tau^2 d\Omega\right)^{\frac{1}{2}} \tag{2.8}$$

We now introduce a functional $M_\alpha(\sigma, t)$ in the form (2.9), which represents a mean integral value of stress $\sigma(t)$ in the time space and is considered as the dynamic stress intensity [1] within an incubation time interval $[t-\tau, t]$.

$$M_\alpha(\sigma, t) = \left(\frac{1}{\tau}\int_{t-\tau}^{t} \sigma^\alpha(s)\mathrm{d}s\right)^{1/\alpha} \tag{2.9}$$

In more general cases, the yield criterion is supposed to be summarised in the following form, similar to classical yield criterion

$$M_\alpha(\bar{\sigma}(\mathbf{s}), t) \leqslant \sigma_y \text{ or } \|\bar{\sigma}\|_\alpha \leqslant \sigma_y. \tag{2.10}$$

Hence, the criterion (2.1) can be stated as follows: the yield occurs when the dynamic stress intensity within an incubation time interval reaches a critical value.

The functional $M_\alpha(\sigma, t)$ characterises the stress intensity along the time axis and regards the strain-rate sensitivity as a manifestation of the time sensitivity. The strain-rate sensitivity refers to the reaction of the material behavior to the variation of the strain-rate, while the time sensitivity is related to the reaction of the material behavior to the variation of state variables along the time axis. Especially, the functional $M_\alpha(\sigma, t)$ focuses the variation of stress state in the time interval with a constant length τ. This means not only the strain rate, but also the development of stress state matter. In uniaxial tension or compression impact tests, a constant strain rate is often assumed. In this special case, the stress state is mainly characterised by the stress rate or the strain rate according to the Hook's law, and the criterion (2.10) derives the rate-dependent criterion (2.3).

The modified relaxation model of plasticity

At first, let us focus on the one-dimensional problem and discuss the framework of the modified RP model. In the original RP model, the parameter β is used to represent the hardening response. In the modified model, we introduce a hardening

---

[1] The dynamic stress intensity can also be a norm of the measurable function $\sigma(t)$ in the Lebesgue space (L^p space), as defined below, where $t' = t/\tau$ and $s' = s/\tau$.

$$M_\alpha(\sigma, t) = \|\sigma\|_\alpha = \left(\int_{t'-1}^{t'} \sigma^\alpha(s')\mathrm{d}s'\right)^{1/\alpha}, 1 \leqslant \alpha \leqslant \infty,$$

function $\sigma_c(t)$ into the identity (2.4) as follows:

$$\frac{1}{\tau}\int_{t-\tau}^{t}\left(\frac{\gamma(t)\Sigma(s)}{\sigma_c(t)}\right)^{\alpha} ds \equiv 1. \tag{2.11}$$

Now we reformulate the identity (2.11) using the notation $M_\alpha(\sigma, t)$ and introduce a strain hardening function $\sigma_c(\varepsilon_p(t))$, then we have

$$M_\alpha(\Sigma, t)\gamma(t) \equiv \sigma_c(\varepsilon_p(t)),\ \forall t \geqslant t_y, \tag{2.12}$$

where $\sigma_c(\varepsilon_p(t_y)) = \sigma_y$ and $\varepsilon_p(t) = 0,\ \forall t \leqslant t_y$. The Ludwik's hardening rule [88] expressed in equation (2.13) could be one choice for the function $\sigma_c(t)$. Additionally, a quadratic interpolation for the hardening rule [89] may also be utilized. Here, σ_y remains the meaning of yield stress, ε_p represents the plastic strain, while K and n are the hardening parameters. Parameter n is also known as the strain hardening exponent.

$$\sigma_c(\varepsilon_p(t)) = \sigma_y + K\varepsilon_p^n(t) \tag{2.13}$$

According to identity (2.12), the relaxation function $\gamma(t)$ is assumed to be

$$\gamma(t) = \frac{\sigma_c(\varepsilon_p(t))}{\widetilde{\Sigma}(t)} \tag{2.14}$$

where

$$\tilde{\Sigma}(t) = \begin{cases} \sigma_y, & t < t_y \\ M_\alpha(\Sigma, t), & t \geqslant t_y \end{cases}$$

Furthermore, according to equation (2.6), the true stress is now determined by equation (2.15):

$$\sigma(t) = \Sigma(t)\gamma(t) = \Sigma(t)\frac{\sigma_c(\varepsilon_p(t))}{\widetilde{\Sigma}(t)} = \sigma_c(\varepsilon_p(t))\left(\frac{\Sigma(t)}{\widetilde{\Sigma}(t)}\right) \tag{2.15}$$

An important characteristic of the modified model is its ability to describe both the elastic and plastic responses of materials under various strain rates simultaneously. In the case of elastic deformation ($t < t_y$), it is evident that $\sigma_c(\varepsilon_p(t)) = \tilde{\Sigma}(t) = \sigma_y$, and then $\sigma(t) = \Sigma(t) = E\varepsilon(t)$. At plastic deformation stage, we can have a framework of the modified RP model in a multiplicative form (2.16), which is actively used in this work. The modification of the RP model primarily involves the definition of the hardening behavior. Instead of using the hardening parameter β, we introduced a strain hardening function $\sigma_c\left(\varepsilon_p(t)\right)$ into the identity (2.4) to replace the single yield constant σ_y. The strain hardening function $\sigma_c(\varepsilon_p(t))$ can be defined by the experimentally measured quasi-static stress-strain curve, since in cases $\dot{\varepsilon}\tau \ll 1$ we have $M_\alpha(\Sigma, t) \approx \Sigma(t)$ and, then, $\sigma(t) \approx \sigma_c(\varepsilon_p(t))$. The second multiplier $\frac{\Sigma(t)}{M_\alpha(\Sigma,t)}$, or more precisely $M_\alpha(\Sigma, t)$, contributes to describing strain-rate effects. Therefore, the RP model regards the strain-rate sensitivity as a manifestation of the time sensitivity.

$$\sigma(t) = \sigma_c(\varepsilon_p(t))\left(\frac{\Sigma(t)}{M_\alpha(\Sigma, t)}\right), \forall t \geqslant t_y. \tag{2.16}$$

On the relaxation function $\gamma(t)$

During the plastic deformation, the true stress σ can be determined based on the plastic strain using equation (2.17), which involves a dimensionless function $\gamma(\varepsilon_p)$. This function γ, ranging from $(0, 1]$, characterizes the relaxation behavior of materials during plastic deformation. The plastic strain ε_p can be obtained using the hardening function $\sigma_c(\varepsilon_p, \dot{\varepsilon})$ (see equation (1.4)) through equation (2.18). Additionally, the relaxation function $\gamma(t) = \gamma(\varepsilon_p(t))$ can be determined using expression (2.19). For instance, in the case of a multiplicative hardening function $\sigma_c(\varepsilon_p, \dot{\varepsilon}) = f_1(\varepsilon_p)f_2(\dot{\varepsilon})$, the relaxation function γ at the quasi-static strain rate $\dot{\varepsilon}_0$ takes the value $\gamma(\varepsilon_p) = \frac{\sigma_c(\varepsilon_p,\dot{\varepsilon}_0)}{\Sigma(\varepsilon)} = \frac{f_1(\varepsilon_p)}{\Sigma(\varepsilon)} = \frac{\sigma_c(\varepsilon_p)}{\Sigma(\varepsilon)}$ with $f_2(\dot{\varepsilon}_0) = 1$. In the incubation time approach, instead of directly considering the strain rate $\dot{\varepsilon}$, we introduce a time functional $M_\alpha(\cdot)$ that incorporates the incubation or relaxation time parameter τ. Consequently, the relaxation function $\gamma(t)$ is assumed to be given by equation (2.20), consistent with classical theory, i.e. $\gamma(t) = \frac{\sigma_c(\varepsilon_p(t))}{M_\alpha(\Sigma,t)} \approx \frac{\sigma_c(\varepsilon_p(t))}{\Sigma(t)}$ when $\dot{\varepsilon}\tau = \dot{\varepsilon}_0\tau \ll 1$. Equation (2.20) may lead to the identity presented in equation (2.12). It should be noted that one of the drawbacks of the original RP model is the relaxation function $\gamma(t) = \frac{\sigma_y}{M_\alpha(\Sigma,t)}$ in equation (2.4) or (2.5) does not contain the plastic strain $\varepsilon_p(t)$, which limits its modeling ability over a wide strain range.

$$\sigma = E(\varepsilon - \varepsilon_p) = E\varepsilon(1 - \frac{\varepsilon_p}{\varepsilon}) = \Sigma(\varepsilon)\gamma(\varepsilon_p) \tag{2.17}$$

$$\sigma = \Sigma(\varepsilon)\gamma(\varepsilon_p) = \sigma_c(\varepsilon_p, \dot{\varepsilon}) \tag{2.18}$$

$$\gamma(t) = \frac{\sigma_c(\varepsilon_p(t), \dot{\varepsilon}(t))}{\Sigma(t)} \tag{2.19}$$

$$\gamma(t) = \frac{\sigma_c(\varepsilon_p(t))}{M_\alpha(\Sigma, t)} \tag{2.20}$$

The equation (2.18) can be the one-dimensional form of the yield surface equation (1.4). Similarly, the modified RP model (2.12), (2.15) can also be derived by the yield surface equation $f(\boldsymbol{\sigma}, \varepsilon_p, t) \equiv 0$ in the framework of the incubation time approach instead of being introduced empirically by following the multiplicative form $\sigma = f_1(\varepsilon_p, \dot{\varepsilon})f_2(\varepsilon_p, T)$. The shear stress intensity $\bar{\sigma}(t)$ given by the stress tensor $\boldsymbol{\sigma}$ could be regarded as a product of two functions $\bar{\sigma}(t) = \Sigma(t)\gamma(t)$, where $\Sigma(t)$ is the stress predictor and $\gamma(t)$ is the relaxation function ranging in $(0, 1]$. Then, following the equation (2.20), we expect an equation $f(\boldsymbol{\sigma}, \varepsilon_p, t) = M_\alpha(\Sigma, t)\gamma(t) - \sigma_c(\varepsilon_p(t)) \equiv 0$ to define the yield surface, and the identify (2.12) characterizes the plastic flow.

In subsequent sections of this work, our focus lies on the implementation and examination of the modified RP model. Specifically, we explore different versions of this model by considering various options for the strain hardening function $\sigma_c(\varepsilon_p(t))$ and the stress predictor $\Sigma(t)$. For the sake of simplicity and clarity in our discussions, we will primarily refer to the modified RP model (2.16) as the "RP model". It is important to note that whenever we mention the original RP model (2.6), we will denote it as the ORP model.

A simplified version of the relaxation model of plasticity

As is known, the strain rate almost remains constant in Hopkinson pressure bar experiments, thus we can derive a simplified version of RP model by assuming a linear stress predict $\Sigma(t) = E\varepsilon(t) = E\dot{\varepsilon}tH(t)$. Then the functional $M_\alpha(\Sigma, t)$ can be calculated as follows

$$\begin{aligned}
M_\alpha(\Sigma,t) &= \left(\frac{1}{\tau}\int_{t-\tau}^{t}(E\dot{\varepsilon})^\alpha H(s)ds\right)^{1/\alpha} = \frac{E\dot{\varepsilon}}{\tau^{1/\alpha}}\left(\left.\frac{s^{1+\alpha}H(s)}{1+\alpha}\right|_{t-\tau}^{t}\right)^{1/\alpha} \\
&= \frac{E\dot{\varepsilon}}{\tau^{1/\alpha}}\left(\frac{t^{1+\alpha}-(t-\tau)^{1+\alpha}H(t-\tau)}{1+\alpha}\right)^{1/\alpha} \\
&= E\left(\frac{\varepsilon^{1+\alpha}-(\varepsilon-\dot{\varepsilon}\tau)^{1+\alpha}H(\varepsilon-\dot{\varepsilon}\tau)}{\dot{\varepsilon}\tau(1+\alpha)}\right)^{1/\alpha}.
\end{aligned} \tag{2.21}$$

This leads to a rate-dependent simplified RP model (2.22) or the alternative version (2.23), which also confirms the rate sensitivity as a manifestation of the time sensitivity of materials. The function $g(t)$ denotes the multiplier $\frac{\Sigma(t)}{M_\alpha(\Sigma,t)}$.

$$\sigma(t) = \sigma_c\left(\varepsilon_p,T\right)g(\varepsilon,\dot{\varepsilon}) = \sigma_c\left(\varepsilon_p,T\right)\left(\frac{\dot{\varepsilon}\tau(1+\alpha)\varepsilon^\alpha}{\varepsilon^{1+\alpha}-(\varepsilon-\dot{\varepsilon}\tau)^{1+\alpha}H(\varepsilon-\dot{\varepsilon}\tau)}\right)^{1/\alpha} \tag{2.22}$$

$$\sigma(t) = \begin{cases} \sigma_c\left(\varepsilon_p,T\right)\left(\frac{\dot{\varepsilon}\tau(1+\alpha)}{\varepsilon}\right)^{1/\alpha}, & \frac{\varepsilon}{\dot{\varepsilon}\tau} \leqslant 1, \\ \sigma_c\left(\varepsilon_p,T\right)\left(\frac{\dot{\varepsilon}\tau(1+\alpha)\varepsilon^\alpha}{\varepsilon^{1+\alpha}-(\varepsilon-\dot{\varepsilon}\tau)^{1+\alpha}}\right)^{1/\alpha}, & \frac{\varepsilon}{\dot{\varepsilon}\tau} > 1. \end{cases} \tag{2.23}$$

At relatively low strain rates $\dot{\varepsilon}\tau \ll 1$ or $\xi = \frac{\varepsilon}{\dot{\varepsilon}\tau} \gg 1$, we have

$$\begin{aligned}
g(\varepsilon,\dot{\varepsilon}) = g(\xi) &= \left(\frac{1+\alpha}{\xi-(\xi-1)\left(1-\frac{1}{\xi}\right)^\alpha}\right)^{1/\alpha} \\
&= \left(\frac{1+\alpha}{(1+\alpha)-\frac{\alpha(\alpha+1)}{2}\xi^{-1}+\frac{(\alpha-1)\alpha(\alpha+1)}{6}\xi^{-2}-\frac{(\alpha-2)(\alpha-1)\alpha(\alpha+1)}{24}\xi^{-3}+o\left(\xi^{-4}\right)}\right)^{1/\alpha} \\
&\approx 1.
\end{aligned} \tag{2.24}$$

This verifies the correspondence between the simplified RP model and the classical quasi-static model, i.e. $\sigma(t) \approx \sigma_c\left(\varepsilon_p,T\right)$ under quasi-static conditions.

An incremental version of the relaxation model of plasticity

The RP model (2.16) may have different versions by choosing various strain hardening functions $\sigma_c(\varepsilon_p(t))$ and the form of the stress predictor $\Sigma(t)$. By introducing an incremental version of the stress predictor $\Sigma(t)$ defined in equation (2.25), we can derive the incremental version of the RP model (IRP model), which takes the development of the true stress account.

Let's consider a time sequence $\{t_k\}$, where $t_k - t_{k-1} = h$ and $t_0 = t_y$. Here, h represents the length of a time increment, and t_y indicates the start time of the plastic process ($M_\alpha(\Sigma, t_y) = \sigma_y$). During elastic deformation, $\Sigma(t)$ remains as the elastic stress $\Sigma(t) = E\varepsilon(t)$. However, during plastic deformation ($t \geqslant t_0 = t_y$), $\Sigma(t)$ is dependent on the time interval $[t_k, t_{k+1}]$ (or technically, the index k) and is determined as follows:

$$\Sigma(t) \overset{\text{def}}{=} \Sigma^{(k)}(t) = \begin{cases} \sigma(t), & t \leqslant t_k \\ \sigma\left(t_k\right) + E\left(\varepsilon(t) - \varepsilon\left(t_k\right)\right), & t \in \left(t_k, t_{k+1}\right] \end{cases}, k = 0, 1, 2, \ldots. \tag{2.25}$$

The graphical representation of the function $\Sigma(t)$ is represented in figure 2.1. The incremental version of the stress predictor $\Sigma(t)$ coincides with the true stress $\sigma(t)$ in past time increments and proposes an elastic increment only within the last time increment $[t_k, t_{k+1}]$, since $\Sigma(t) - \Sigma(t_k) = \Sigma(t) - \sigma(t_k) = E\left(\varepsilon(t) - \varepsilon\left(t_k\right)\right)$. The true stress at time t_{k+1}, for instance, can be obtained by $\sigma(t_{k+1}) = \Sigma^{(k+1)}(t_{k+1}) \cdot \gamma(t_{k+1})$ as shown in figure 2.1.

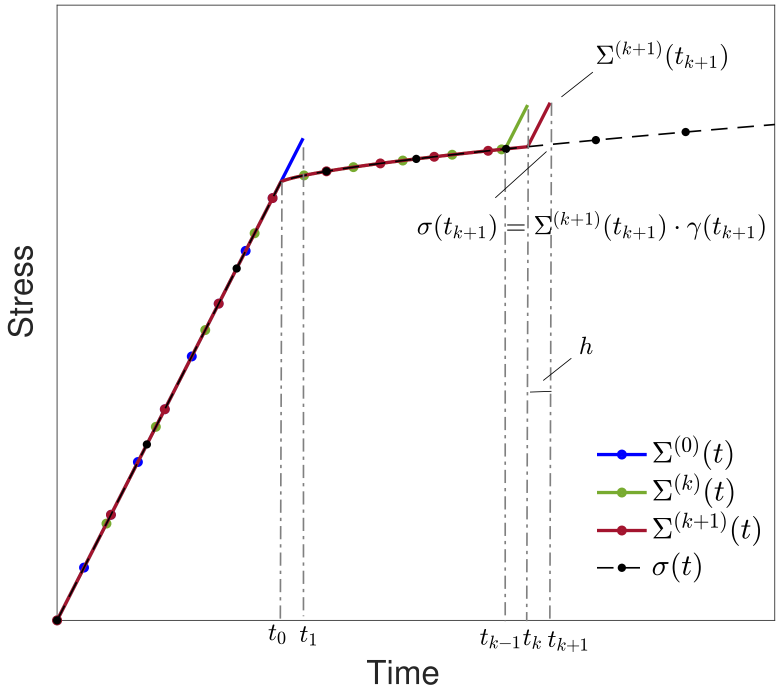

Figure 2.1: The time dependence of the stress predictor $\Sigma(t)$.

Based on numerous experimental data for various materials under dynamic loading, it has been observed that the ratio $m = t_y/h$ can be a constant for most metals. The dimensionless parameter m should also satisfy the logical relation $h \leqslant \tau$. In the quasi-static case, $h = \tau$ is required. The calculation scheme of the IRP model is illustrated in figure 2.2.

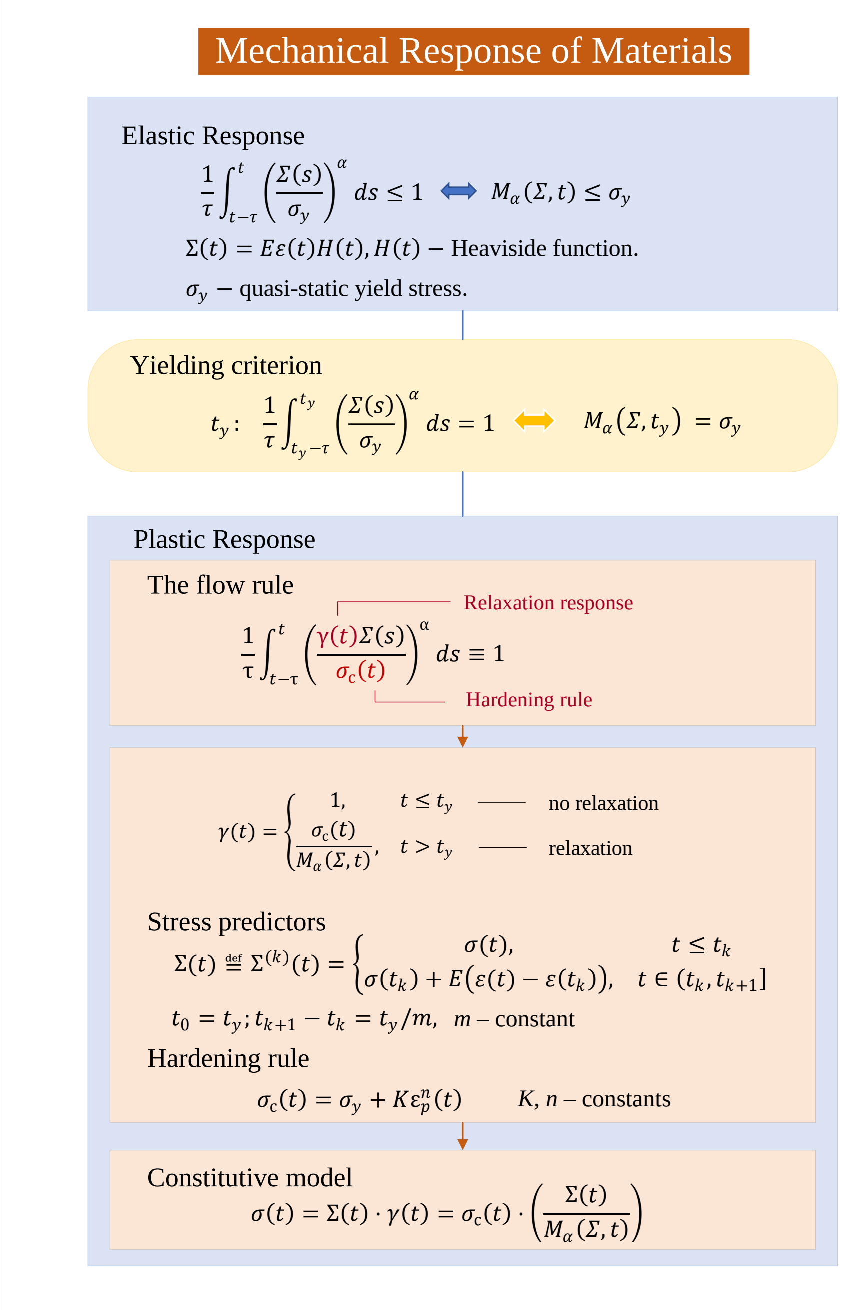

Figure 2.2: Calculation scheme of the IRP model

Possible scenarios of the IRP model

The IRP model allows one to simulate both the monotonic and non-monotonic behaviour of the elasto-plastic deformation due to the multiplier $\Sigma(t)/M_\alpha(\Sigma, t)$.

Since the strain-rate is believed to be nearly unchanged in most uniaxial tensile and compression tests, here the discussion is continued in the case of a constant strain-rate $\varepsilon(t) = \dot{\varepsilon} t H(t)$. The monotonic yield diagram under the quasi-static condition is considered. In a quasi-static case (not strictly speaking, $\dot{\varepsilon}\tau \ll 1$), it has been discussed above that there is no significant distinction between the value of the functional $M_\alpha\left(\Sigma, t\right)$ and the function $\Sigma(\mathrm{t})$. Thus, the strain-rate-dependent multiplier $\Sigma(t)/M_\alpha(\Sigma, t)$ is close to 1 and the Ludwik's hardening rule plays a crucial role, which corresponds with the classical model of plasticity and gives a monotonic stress-strain curve. The IRP model can also deal with the non-monotonic yield diagram under the dynamic or impact condition. Let us consider the simplest case when $\dot{\varepsilon}\tau \geqslant \frac{(1+\alpha)^{1/\alpha}\sigma_y}{E}$, i.e. $t_y \leqslant \tau$. According to equation (2.26), the following inequality (2.27) derives the relation $\Sigma\left(t_y\right)/M_\alpha\left(\Sigma, t_y\right) > \Sigma\left(t_y + h\right)/M_\alpha\left(\Sigma, t_y + h\right)$, which verifies the possibility of simulating the yield drop phenomenon. The inequality $\dot{\varepsilon}\tau \geqslant \frac{(1+\alpha)^{1/\alpha}\sigma_y}{E}$ is not considered a necessary condition of appearing the yield drop phenomenon. It just simplify the theoretical analysis of the non-monotonic behaviour of the multiplier $\Sigma(t)/M_\alpha\left(\Sigma, t\right)$.

$$\begin{gathered} M_\alpha\left(\Sigma, t_y\right) = \left(\frac{1}{\tau}\int_0^{t_y} (E\dot{\varepsilon}s)^\alpha ds\right)^{1/\alpha} = \left(\frac{(E\dot{\varepsilon})^\alpha}{\tau}\frac{{t_y}^{1+\alpha}}{1+\alpha}\right)^{1/\alpha}, \\ M_\alpha\left(\Sigma, t_y + h\right) = \left(\frac{(E\dot{\varepsilon})^\alpha}{\tau}\frac{(t_y+h)^{1+\alpha}}{1+\alpha}\right)^{1/\alpha} \end{gathered} \tag{2.26}$$

$$\left(t_y + h\right)^{1+\alpha} t_y^\alpha > t_y^{1+\alpha}\left(t_y + h\right)^\alpha \tag{2.27}$$

As for the JC model (1.6), it is clear that it shows only monotonic curves. Furthermore, due to the low increasing rate of the logarithm function $\ln\left(\frac{\dot{\varepsilon}}{\dot{\varepsilon}_0}\right)$, sometimes the JC model fails to show the difference between flow stress levels at intermediate- and high-rate loading.

2.2 Temperature-time correspondence

In the modified RP model (2.16), strain-rate effects are mainly characterized using the functional $M_\alpha\left(\Sigma, t_y\right)$, or more precisely, the relaxation time parameter τ. As relaxation process is obviously affected by temperature, its relaxation time should be temperature dependent. This section explores one of the main topics — the temperature-time correspondence and proposes a methodology for investigating this relationship. The introduction of the relative stress factor helps analyze the tendency of the temperature-time relationship. A possible explanation for different phenomenological relationships proposed previously is provided and further discussed in section 4.2. Additionally, the suitability of multiplicative models $\sigma = f_1(\varepsilon_p, \dot{\varepsilon})f_2(\varepsilon_p, T)$ for simulation over a wide range of temperatures and strain rates is examined.

2.2.1 Parameters τ and α

Understanding how parameters τ and α affect the behavior pattern of materials under different mechanical conditions is crucial for accurately modeling the thermo-mechanical response of considered materials. The expression (2.3) provides a simplified mathematical relation between the yield stress and two parameters τ and α. Nevertheless, the graphical demonstration of the stress-strain diagrams in figures 2.3 (a) and (b) directly show the capacity of τ and α to describe the strain-rate effect. In these examples, the IRP model is used to simulate the stress-strain diagrams in figures 2.3 (a) and (b) with different parameter values τ and α, where a constant strain rate, i.e. $\varepsilon(t) = \dot{\varepsilon}t$, is assumed. The values τ_0, α_0 are considered the reference. The $\dot{\varepsilon}_0$ represents the quasi-static strain rate, and the stress $\sigma(\varepsilon_p, \dot{\varepsilon}_0)$, equal to $\sigma_c(\varepsilon_p(t))$, is assumed the reference stress. In most cases, the parameters τ and α have an insignificant impact on the stress at the quasi-static strain rate $\dot{\varepsilon}_0$ [84], as shown in figures 2.3 (a) and (b), where dashed curves nearly overlap. In figures 2.3 (c) and (d), the relative stresses (RS), i.e. $\sigma(\varepsilon_p, \dot{\varepsilon})/\sigma(\varepsilon_p, \dot{\varepsilon}_0)$, at different strain rates and values of τ and α are demonstrated.

It is shown that, at fixed values of τ and α, the increasing strain rate ($\dot{\varepsilon} > \dot{\varepsilon}_0$) results in an elevated stress level; at the fixed strain rate $\dot{\varepsilon}$, the decreasing τ with the fixed α or increasing α with the fixed τ leads to a decreased stress value. It is more important to note that parameters τ and α, in fact, affect the relative relation of the stress value $\sigma(\varepsilon_p, \dot{\varepsilon})$ to their reference stress $\sigma(\varepsilon_p, \dot{\varepsilon}_0)$, i.e. the value of the RS, which is also discussed in detail in subsections 2.2.2 and 2.2.3. Therefore, we can conclude that the decreasing τ with the fixed α or increasing α with the fixed τ leads to a decreased value of RS at the fixed strain rate.

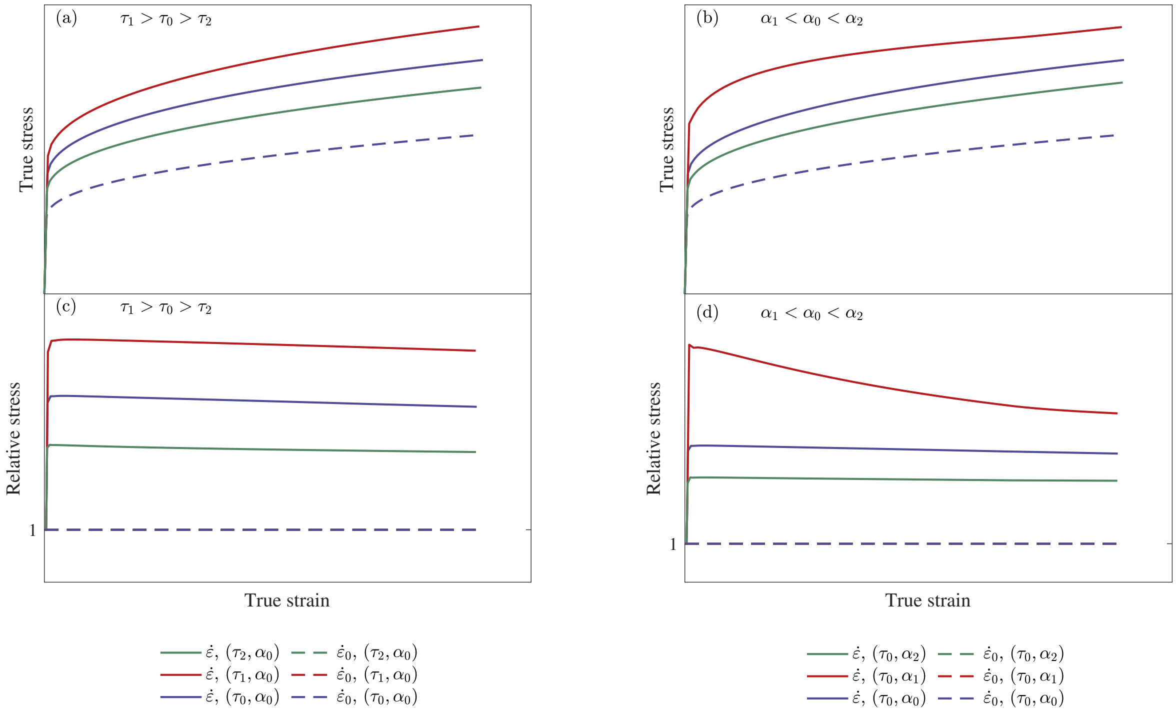

Figure 2.3: The stress-strain diagrams calculated by the IRP model (2.12)–(2.25) and the corresponding relative stress curves $\sigma(\varepsilon_p, \dot{\varepsilon})/\sigma(\varepsilon_p, \dot{\varepsilon}_0)$ under different strain rates and parameter values τ and α. In (a) and (c), parameters τ_0, τ_1 and τ_2 follow the relation $\tau_1 > \tau_0 > \tau_2$, while in (b) and (d), the parameters α_0, α_1 and α_2 satisfy $\alpha_1 < \alpha_0 < \alpha_2$. Stress curves at the quasi-static strain rate $\dot{\varepsilon}_0$ are depicted by dashed lines, while those at a higher strain rate, denoted by $\dot{\varepsilon}$, are shown using solid lines.

2.2.2 The temperature dependence of the parameter τ and/or α

It is experimentally observed that the increasing initial temperature T_0 of materials generally results in the relaxation of the flow stress, i.e. thermal softening. In addition, at high loading rates, the plastic deformation is accompanied by an approximately adiabatic temperature rise. Thus, the understanding of the thermal softening of materials under different loading conditions is important for its modeling. It is reasonable to expect that the relaxation function (2.20) is temperature-dependent, i.e. $\gamma(T,t) = \frac{\sigma_c(\varepsilon_p(t),T(t))}{M_\alpha(\Sigma,T,t)}$, since a thermal softening behavior leads to a stress relaxation. That means the hardening function $\sigma_c(\varepsilon_p(t),T(t))$ and/or the dynamic stress intensity $M_\alpha(\Sigma,T,t)$ should be temperature-dependent. Hence, the modified RP model (2.16) is expected to be the following one

$$\sigma(t) = \sigma_c(\varepsilon_p(t),T(t))\left(\frac{\Sigma(t)}{M_\alpha(\Sigma,T,t)}\right), \ \forall t \geqslant t_y. \tag{2.28}$$

The hardening function $\sigma_c(\varepsilon_p(t),T(t))$ (or $\sigma_c(\varepsilon_p,T)$) could take various forms depending on the quasi-static behavior of tested materials at different temperatures, for instance, the well-known forms (2.29) and (2.30). Here, A, B_0, B_1, n_0, n_1 and β_1 are model parameters; T_m is the melting temperature and T_r is the reference temperature.

$$\sigma_c(\varepsilon_p,T) = \left(A + B_0\varepsilon_p^{n_0}\right)\left(1 - \left(\frac{T-T_r}{T_m-T_r}\right)^{n_1}\right) \tag{2.29}$$

$$\sigma_c(\varepsilon_p,T) = A + B_0\varepsilon_p^{n_0} + B_1\exp\left(-\beta_1 T\right) \tag{2.30}$$

The dynamic stress intensity $M_\alpha(\cdot)$ shall also be temperature-dependent. According to Cottrell and Bilby's dislocation theory, Campbell derived an integral yield criterion [54]. In his criterion, α is temperature-dependent parameter shown in expression (2.35), where n is a model constant and k is the Boltzmann's constant. Gruzdkov and Petrov [9] introduced a temperature-dependent relation of the incubation time given in the expression (2.31), assuming that the parameter α is a constant and the incubation time is inversely proportional to the average dislocation velocity proposed by Johnson and Gilman [90]. Selyutina [10] suggested another temperature-time relation (2.33). In this work, we examine these relations along with two additional phenomenological relations (2.32) and (2.34) to analyze why different relations were used and how to determine the temperature-time correspondence for various materials. The results in figures 2.3 (a) and (b) suggest the possible temperature-dependent behavior of τ and/or α. On the other hand, assuming only one of them as temperature-dependent is more convenient for numerical modeling.

$$\tau = \tau_0 \exp\left(\frac{\beta_0}{T}\right), \ \alpha = \text{constant}. \tag{2.31}$$

$$\tau = \tau_0 \exp(-\beta_0 T), \ \alpha = \text{constant}. \tag{2.32}$$

$$\tau = \tau_0 \left(1 - \left(\frac{T - Tr}{Tm - Tr}\right)^{\beta_0}\right), \ \alpha = \text{constant}. \tag{2.33}$$

$$\tau = \tau_0 \left(\frac{Tm - T}{Tm - Tr}\right)^{\beta_0}, \ \alpha = \text{constant}. \tag{2.34}$$

The incubation time is a characteristic time of the relaxation nature of microscopic events. The softening of materials, as a relaxation event, is significantly affected by temperature. Higher temperatures can cause more noticeable softening, leading to a decrease in its characteristic time. The temperature-time correspondence can be mathematically summarised through the temperature dependency of the incubation time τ. In addition, the following temperature-dependences of parameter α are also concerned for comparison.

$$\alpha = (nkT)^{-1}, \ \tau = \text{constant}. \tag{2.35}$$

$$\alpha = \alpha_0 \exp(\beta_0 T), \ \tau = \text{constant}. \tag{2.36}$$

$$\alpha = \alpha_0 \left(\frac{Tm - Tr}{Tm - T}\right)^{\beta_0}, \ \tau = \text{constant}. \tag{2.37}$$

As concluded in the section 2.2.1, a decrease in τ or an increase in α results in a lower stress level, which seems to agree with the thermal softening (or relaxation) of the flow stress. However, according to the equation (2.28), the value of the reference stress (at the reference strain rate $\dot{\varepsilon}_0$) $\sigma_c(\varepsilon_p, T)$ significantly influences the value of the flow stress as well. Equation (2.28) suggests that with even the constant value of τ and α, one can technically model the decreasing tendency of the flow stress at an elevated temperature if the reference stress $\sigma_c(\varepsilon_p, T)$ decreases with the increasing temperature (see expressions (2.29) and (2.30)). Nevertheless, it should be noted that the parameters τ and α only affects the relative relation of the flow stress $\sigma(\varepsilon_p, \dot{\varepsilon}, T)$ to their reference stress $\sigma_c(\varepsilon_p, T)$ as shown in figures 2.3 (c) and (d). Hence, the temperature-dependent parameter τ or α should only reflect the variation of the relative stress (RS) at different temperatures, which is featured by the RS factor $\frac{\sigma(\varepsilon_p,\dot{\varepsilon},T)}{\sigma(\varepsilon_p,\dot{\varepsilon}_0,T)}$. In a wide temperature range, the RS factor generally decreases with increasing temperature for many materials, although its non-monotonic temperature dependence sometimes appears. The performance of RS factor for materials HSLA-65 steel and a Tungsten-based composite are discussed below in subsection 2.2.3. Different temperature-dependent relations of τ or α given in expressions (2.31)–(2.37) are considered in sections 2.2.3, 2.2.4 and 4.2.

2.2.3 The relative stress factor for HSLA-65 steel and Tungsten-based composite

In Nemat-Nasser and Guo's work [14], the thermo-mechanical response of the HSLA-65 steel was investigated over a wide range of strain rates and temperatures. The temperature dependence of the true stress at different strain rates and a true strain of 10%, 15% and 20% are demonstrated in figures 2.4 (a), (c) and (e), while figures 2.4 (b), (d) and (f) depict the corresponding temperature dependence of the RS factor $\sigma(\varepsilon, \dot{\varepsilon}, T)/\sigma(\varepsilon, \dot{\varepsilon}_0, T)$. The reference strain rate $\dot{\varepsilon}_0$ was taken as $0.001\, s^{-1}$. The symbols in the figures represent experimental data from the work [14] and the dash-dotted curves approximate experimental data using the spline algorithm to show the trend of their variation with increasing temperature. The results indicate that the mechanical response of HSLA-65 steel at low loading rates $\dot{\varepsilon} = 0.001\, s^{-1}, 0.1\, s^{-1}$ is temperature-insensitive at temperatures of 296–700 K, whereas the curves at high loading rates are temperature-sensitive in this temperature range. Nemat-Nasser and Guo suggest that the temperature-insensitivity range in high-loading cases may shift to even higher values of temperature due to the dynamic strain aging of the material. Some abnormal material responses caused by dynamic strain aging require additional attention and are not discussed in our paper. These responses include the unusual performance of the true stress at strain rate $0.1\, s^{-1}$, i.e. the stress at the temperature of 400–600 K being lower than that at lower strain rate $0.001\,s^{-1}$, and the abnormal behavior of the true stress at temperatures higher than 700 K, i.e. the stress at strain rate $3000\,s^{-1}$ increasing with elevated temperature. Hence, cases at strain rate $0.1\,s^{-1}$ and cases at temperatures higher 700 K are out of consideration.

The RS factors at high strain rates $3000\,s^{-1}$ and $8500\,s^{-1}$ and temperatures up to 700 K are studied in figures 2.4 (b), (d) and (f). Note that the values of left and right ends of curves at high strain rates are greater than the initial temperatures 77 K and 700 K, at which samples were tested. These are explained by the intensive adiabatic temperature rise discussed in section 1.1. Under impact loading, final temperatures of samples tested initially at temperatures of 77 K and 700 K have increased up to more than 105 K and 710 K, respectively, at the true strain of 10%. Results in figures 2.4 show that the RS factors are not only rate-dependent but also temperature-dependent. Over a wide temperature range, $T \in (250\,K, 600\,K)$, the RS factor decreases with increasing temperature, while in other temperature ranges, they might slightly increase. The tiny growth in RS factors at higher temperatures could be linked to the abnormal increase in stresses at the reference strain rate and temperatures of 400–650 K. This abnormal behavior can result in a noticeable drop of the RS factor within this temperature range, which in turn "causes" a slight increase in the RS factor at temperatures higher 650 K. The RS factors at lower temperatures seem also slightly increase. For the Tungsten-based composite, however, the mentioned here abnormal phenomena do not exist in a very wide temperature range.

Xu and Huang [16] conducted experiments on a Tungsten-based composite with a composition of 93W–4.9Ni–2.1Fe over a wide range of temperatures and strain rates. Figures 2.5 (a), (c), and (e) show the temperature dependence of the true stress at a plastic strain of 3%, 5%, and 8%, respectively, at different strain rates. Correspondingly, figures 2.5 (b), (d), and (f) display the temperature dependence of the RS factor $\sigma(\varepsilon_p, \dot{\varepsilon}, T)/\sigma(\varepsilon_p, \dot{\varepsilon}_0, T)$, where the reference strain rate $\dot{\varepsilon}_0$ is $0.001\,s^{-1}$. The symbols in figures 2.5 represent experimental data from the work [16] and the dash-dotted curves approximate experimental data using the spline algorithm to demonstrate their trend with increasing temperature. At the plastic strain of 8%, the lack of experimental data at strain rate $200\,s^{-1}$ is due to the materials fracturing. The tested Tungsten-based composes are less ductile than the HSLA-65

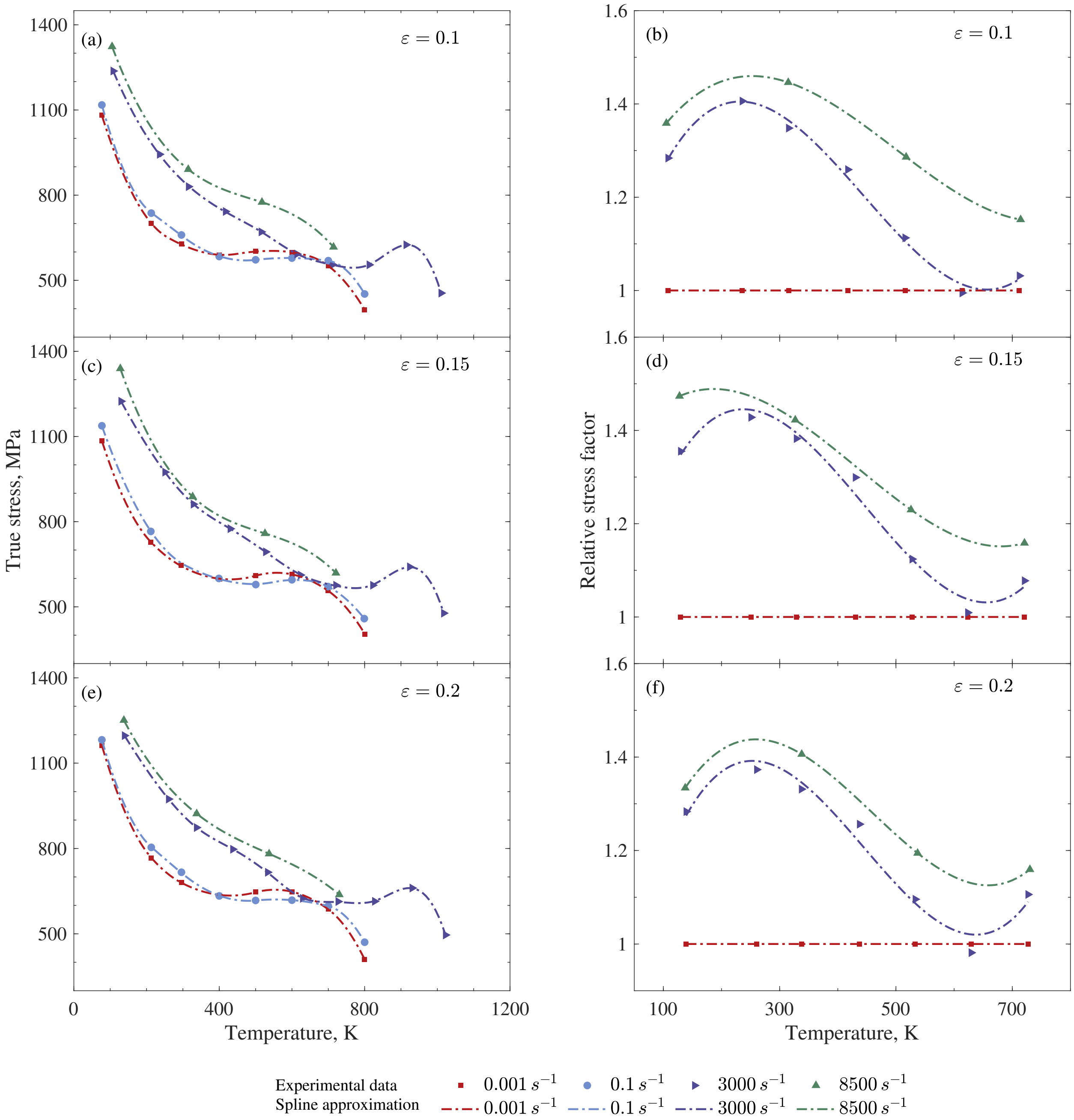

Figure 2.4: The effect of strain rates and temperatures on the true stress $\sigma(\varepsilon, \dot{\varepsilon}, T)$ at a true strain of 10%, 15% and 20% for HSLA-65 steel are presented in (a), (c) and (e), respectively. The symbols are experimental data taken from Nemat-Nasser and Guo's work [14] and dash-dotted lines are curves approximated by the spline algorithm. The corresponding temperature dependence of the relative stress factor $\sigma(\varepsilon, \dot{\varepsilon}, T)/\sigma(\varepsilon, \dot{\varepsilon}_0, T)$ at a true strain of 10%, 15% and 20% are illustrated in (b), (d) and (f), respectively, where $\dot{\varepsilon}_0 = 0.001\, s^{-1}$.

steel. Similar to conclusions drawn for HSLA-65 steel, the RS factor at low loading rates is less sensitive to temperature than at high loading rates. As suggested by Nemat-Nasser and Guo [14], we can expect that the temperature-insensitivity range for materials under dynamic loading conditions may shift to temperatures even higher than thoes under quasi-static loading conditions. Results indicate that, although a special point at strain rate $200\,s^{-1}$ and the room temperature appears, the RS factors at different strain rates are generally monotonically decreasing along the temperature axis.

As concluded in subsection 2.2.2, the decreasing τ with the fixed α or increasing α with the fixed τ leads to the decreasing value of the RS at the fixed strain rate. Hence, in most cases, the parameter τ has a negative correlation with the temperature, and α reveals a positive correlation with the temperature. The relations (2.31)–(2.34), and relations (2.36)–(2.37) agree with what has been observed and their comparison is discussed in section 4.2. The relation (2.35) suggests a negative correlation between α and the temperature and may be useful in some temperature ranges, such as temperatures higher than 600 K for HSLA-65 steel. In summary, at temperatures higher than room temperature, the RS factors of tested materials at different strain rates generally exhibit a monotonic decrease with increasing temperature. This implies that the temperature rise results in a monotonic decrease in τ or an increase in α. However, some special cases of non-monotonic behavior may occur due to, for instance, the dynamic strain aging, and a non-monotonic relation between τ or α and the temperature might be required. Nevertheless, we focus on simple monotonic relations in this paper.

The behavior of the RS factor at different temperatures suggests that it may be improper to model the strain-rate effect and thermal softening phenomenon separately using specific multipliers depending on the strain rate or the temperature over a wide temperature range. In other words, at least for considered here materials, the constitutive model could not be $\sigma = f_1(\varepsilon_p, \dot{\varepsilon}) f_2(\varepsilon_p, T)$. The widely used Johnson-Cook (JC) model (1.6) consists of three multipliers corresponding to the hardening work, the strain effect, and the temperature effect, respectively. It suggests a temperature-independent RS factor as follows

$$\frac{\sigma(\varepsilon_p, \dot{\varepsilon}, T)}{\sigma(\varepsilon_p, \dot{\varepsilon}_0, T)} = 1 + C \ln\left(\frac{\dot{\varepsilon}}{\dot{\varepsilon}_0}\right),$$

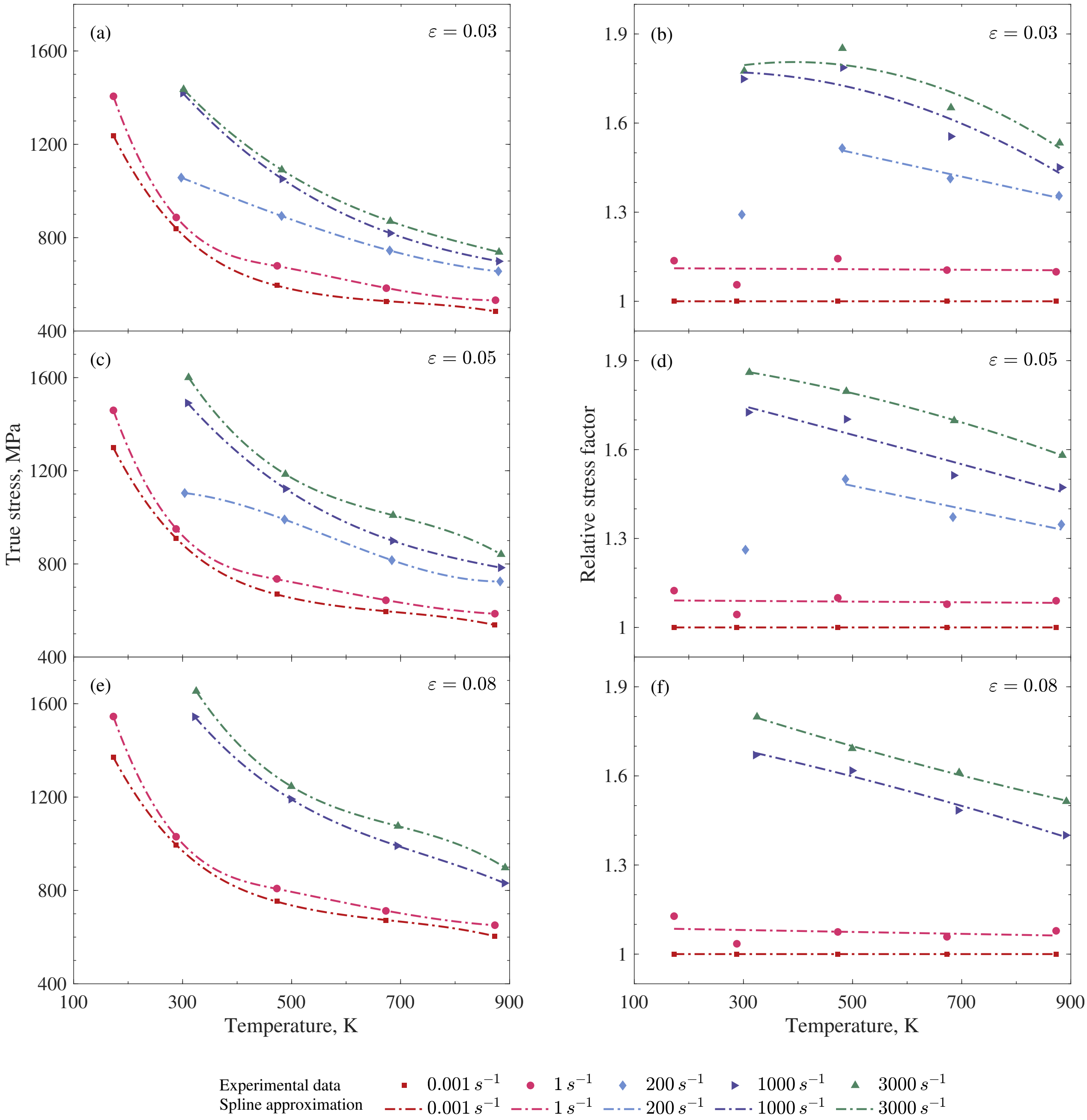

Figure 2.5: The effect of strain rates and temperatures on the true stress $\sigma(\varepsilon_p, \dot{\varepsilon}, T)$ at a plastic strain of 3%, 5% and 8% for the 93W–4.9Ni–2.1Fe Tungsten-based composite are presented in (a), (c) and (e), respectively. The symbols are experimental data taken from Xu and Huang's work [16] and dash-dotted lines are curves approximated by the spline algorithm. The corresponding temperature dependence of the relative stress factor $\sigma(\varepsilon_p, \dot{\varepsilon}, T)/\sigma(\varepsilon_p, \dot{\varepsilon}_0, T)$ at a plastic strain of 3%, 5% and 8% are illustrated in (b), (d) and (f), respectively, , where $\dot{\varepsilon}_0 = 0.001\,s^{-1}$

which does not follow the behavior pattern of the RS factor observed by analyzing existing experimental facts. Similarly, some modifications of the JC model [21] [22] [23] [25] shown in expressions (2.38) could not be suitable for simulations in a wide temperature range as well. These models follow the relation $\sigma = f_1(\varepsilon_p, \dot{\varepsilon}) f_2(\varepsilon_p, T)$, which is derived from the direct empirical fitting approach and results in a temperature-independent RS factor. In these models, dynamic relations are conventionally constructed in the way of direct extrapolation of static notions into dynamic cases using special terms incorporated into well-known static formula. Nevertheless, they are still very convenient for engineering problems where the temperature does not vary significantly. On the other hand, the modified RP model follows the relation $\sigma = f(\varepsilon_p, T, t)$, which is derived from the incubation time approach and concerns the rate-dependent phenomena as manifestation of the time sensitivity of materials.

$$\begin{gathered}
\sigma = \left(A + B\varepsilon_p^n\right) \exp\left(C_0 \ln\left(\frac{\dot{\varepsilon}}{\dot{\varepsilon}_0}\right)\right)\left(1 - \left(\frac{T - T_r}{T_m - T_r}\right)^m\right), \\
\sigma = \left(A + B\varepsilon_p^n\right)\left[1 + C_1 + C_2 \sin\left(\frac{\ln\dot{\varepsilon} - C_3}{C_4}\pi\right)\ln\left(\frac{\dot{\varepsilon}}{\dot{\varepsilon}_0}\right)\right]\left(1 - \left(\frac{T - T_r}{T_m - T_r}\right)^m\right), \\
\sigma = \left(A + B_1\varepsilon_p + B_2\varepsilon_p^2 + B_3\varepsilon_p^3\right)\left[1 + (C_1 + C_2\varepsilon_p)\ln\left(\frac{\dot{\varepsilon}}{\dot{\varepsilon}_0}\right)\right]\left(1 - \left(\frac{T - T_r}{T_m - T_r}\right)^{m_1 + m_2\varepsilon_p}\right).
\end{gathered} \tag{2.38}$$

$$\sigma(t) = \left(A + B_0\varepsilon_p^{n_0}\right)\left(\frac{\Sigma(t)}{M_\alpha(\Sigma, T, t)}\right)\left(1 - \left(\frac{T - T_r}{T_m - T_r}\right)^{n_1}\right), \ \forall t \geqslant t_y. \tag{2.39}$$

The modified relaxation model of plasticity (2.28) can be reformulated in the expression (2.39) closely resembling the well-known Johnson-Cook model in the structure if the hardening function $\sigma_c(\varepsilon_p(t), T(t))$ takes the form (2.29). Beyond that similarity, the model (2.39) is rather different from the JC model. The "strain-rate dependent" term in the model (2.39), represented by $\Sigma(t)/M_\alpha(\Sigma, T, t)$, is a time function and does not explicitly include the strain rate. It accounts for the time sensitivity, characterized by the incubation time parameter τ. Instead, the JC model approximates the rate-dependent behavior through an analytical logarithm function of strain rate, which is based on empirical analysis. This is a direct empirical approach, which is convenient for numerical simulations, such as finite element simulations, but has a negative feature of the single model performance. It has limitations in describing non-monotonic stress-strain behavior, abnormal work-hardening response, and other complex phenomena. To address these limitations, new additional terms (2.38) should be introduced into the JC basis, or the logarithm function should be replaced with other empirical functions depending on the strain rate. In contrast, the modified relaxation model of plasticity (2.28) is derived from the incubation time approach. The "strain-rate dependent" term $\Sigma(t)/M_\alpha(\Sigma, T, t)$ reflects not only the rate-dependent behavior of materials, but also the temperature-dependent pattern of the RS factor.

2.2.4 The determination of parameters τ and α

The hardening function $\sigma_c(\varepsilon_p(t), T(t))$ and its associated parameters need to be determined using quasi-static stress-strain curves. Although the incubation time τ has a physical basis [69, 71], in this work, we treat it as a model parameter (phenomenological parameter). The parameters τ and α at specific temperatures should be established by fitting dynamic diagrams. Common curve fitting algorithms may not converge to determine both τ and α simultaneously. However, they can be separately defined. Assuming the value of parameter α is fixed, then the value of the parameter τ is not difficult to be found using least square method, in particular, the Levenberg–Marquardt algorithm (also called the damped least-squares method). Technically, a value of τ that gives less than 5% description error in dynamic curves (see equation (4.1) is considered suitable. In this work, for the sake of simplicity, the parameter α is taken as an integer, and its value generally varies from 3 to 35 for studied metals. The value of α leading to a less than 5% description error with found value of τ is regard suitable for modeling. We often obtain a range of values for τ at a fixed α suitable for modeling and vice versa, as discussed later in section 4.2 and illustrated in figures 4.4 (b), (c) and 4.8. Sometimes, the value range for τ may be relatively wide, suggesting that slight variations in τ may not significantly impact the final results. In such cases, any temperature-time relationship falling within these value ranges may be considered technically suitable. As a result, different temperature-time correspondences have been suggested and verified to be applicable for modeling dynamic stress-strain diagrams. It is worth noting that a simple linear relationship could also be used. However, this may result in a negative value for τ. Hence, exponential or power phenomenological relationships, as shown in equations (2.31)–(2.34) and (2.35)–(2.37), are preferable choices to avoid negative values.

2.3 Conclusions to the chapter

In this chapter, a comprehensive analysis of the framework of the modified RP model is given. The new understanding of the relaxation function, the time-dependent yield surface equation and a methodology of investigating the temperature-time correspondence are discussed. The following main conclusions are made.

1. A simplified version and incremental version of the RP model are proposed. The incubation time approach considers the rate sensitivity as a manifestation of time sensitivity of materials. The modified RP model can be derived from the proposed yield surface equation instead of using the empirical fitting approach by following the multiplicative form $\sigma = f_1(\varepsilon_p, \dot{\varepsilon}) f_2(\varepsilon_p, T)$.

2. The relative stress (RS) factor can be used to analyze the tendency of the temperature-time relationship. For studied HSLA-65 steel and Tungsten-based composite, the RS factors at different strain rates generally exhibit a monotonic decrease with increasing temperature. This implies that the temperature rise results in a monotonic decrease in τ. Some special cases of non-monotonic behavior may also occur due to, for instance, the dynamic strain aging, and a non-monotonic relation between τ and the temperature might be required.

3. Multiplicative models $\sigma = f_1(\varepsilon_p, \dot{\varepsilon}) f_2(\varepsilon_p, T)$ is not suitable for simulation over a wide range of temperatures and strain rates, while they still provide a power tool for many engineering problems in cases with a limited temperature variation.

Chapter 3

Simulation Methodology: finite element method for dynamic plasticity problems

This chapter provides an introduction to essential concepts related to the finite element (FE) method and presents potential solutions for dynamic plasticity problems. Additionally, a calculation scheme is proposed for performing FE analysis using a simplified version of the RP model. Some algorithms discussed in this chapter have been utilized by the author in their published works [91], [92], [93] and [94].

3.1 A basic background on finite element method

The fundamental basis of the finite element method has been extensively discussed in the works of Professor Belytschko and Zienkiewicz [95, 96, 97]. This section aims to recapitulate certain essential aspects of their works for solving dynamic plasticity problems.

Lagrangian formulations utilize meshes that employ Lagrangian descriptions, where the dependent variables are expressed as functions of both the material (Lagrangian) coordinates $\mathbf{X}$ and time t. The nodes and elements within the mesh move in accordance with the material, while boundaries and interfaces align with the edges of the elements, simplifying their treatment. There are two classifications of Lagrangian meshes: updated Lagrangian formulations and total Lagrangian formulations. In the updated Lagrangian formulation, derivatives are taken with respect to the spatial (Eulerian) coordinates $\mathbf{x}$, and the weak form involves integrals over the current configuration. Conversely, the total Lagrangian formulation performs integrals over the reference configuration and takes derivatives with respect to the material coordinates $\mathbf{X}$. For solving dynamic plasticity problems, we adopt the updated Lagrangian formulation, which expresses the governing equations in terms of the Eulerian coordinates $\mathbf{x}$ and the Cauchy stress $\boldsymbol{\sigma}$. Subsequently, we introduce the principle of virtual power, a weak form for the governing equations.

Weak form: principle of virtual power

The weak form, often called a variational form, reduces the continuity requirements on the basis functions used for approximation which gives way to using lesser degree polynomials. This approach converts the differential equation into an integral form which is usually easier to solve comparatively. The displacement function $u(\mathbf{X}, t) = x(\mathbf{X}, t) - \mathbf{X}$ is required to satisfy all displacement boundary conditions and to be smooth enough so that all derivatives in the momentum equation are well-defined. Additionally, variations in displacement or velocity, denoted as δu or δv, are assumed to exhibit sufficient smoothness to guarantee well-definedness throughout the subsequent steps and vanish at the prescribed displacement boundary Γ_u, i.e. $\delta u = \delta v = 0, \forall \mathbf{x} \in \Gamma_u$. This is the standard, classical way of developing a weak form.

By integrating the product of the momentum equation with a variation of velocity δv over the current configuration, we can have the equation (3.1), where $\mathbf{b}$ is the body force, ρ represents the mass density, and Ω denotes the volume in the current configuration. The equivalent formulation in the form of components is demonstrated in equation (3.2).

$$\int_{\Omega} \delta \mathbf{v} \cdot (\nabla \cdot \boldsymbol{\sigma} + \rho \mathbf{b} - \rho \dot{\mathbf{v}}) \, d\Omega = 0 \tag{3.1}$$

$$\int_{\Omega} \delta v_i \left(\frac{\partial \sigma_{ji}}{\partial x_j} + \rho b_i - \rho \dot{v}_i \right) d\Omega = 0 \tag{3.2}$$

The derivative product rule gives

$$\int_{\Omega} \delta v_i \frac{\partial \sigma_{ji}}{\partial x_j} d\Omega = \int_{\Omega} \left[\frac{\partial}{\partial x_j} (\delta v_i \sigma_{ji}) - \frac{\partial (\delta v_i)}{\partial x_j} \sigma_{ji} \right] d\Omega. \tag{3.3}$$

According to the traction condition $\mathbf{n} \cdot \boldsymbol{\sigma} = \mathbf{t}^*$ on the boundary Γ_t, the first term in expression (3.3) can be converted by Gauss's theorem as follows, where $\Gamma = \Gamma_u \cup \Gamma_t$

is the boundary of the volume Ω.

$$\int_{\Omega} \frac{\partial}{\partial x_j} \left(\delta v_i \sigma_{ji}\right) d\Omega = \int_{\Gamma} \delta v_i n_j \sigma_{ji} d\Gamma = \int_{\Gamma_t} \delta v_i t_i^* d\Gamma. \tag{3.4}$$

Equations (3.2)–(3.4) derive the weak form for the momentum equation and the traction boundary conditions. It is known as the principle of virtual power.

$$\int_{\Omega} \frac{\partial \left(\delta v_i\right)}{\partial x_j} \sigma_{ji} d\Omega - \int_{\Omega} \delta v_i \rho b_i d\Omega - \int_{\Gamma_t} \delta v_i t_i^* d\Gamma + \int_{\Omega} \delta v_i \rho \dot{v}_i d\Omega = 0 \tag{3.5}$$

It is also important to note that items in the weak form (3.5) have physical background. Considering the symmetry of Cauchy stress tensor and rewriting the term

$$\frac{\partial \left(\delta v_i\right)}{\partial x_j} \sigma_{ij} = \delta L_{ij} \sigma_{ij} = \left(\delta D_{ij} + \delta W_{ij}\right) \sigma_{ij} = \delta D_{ij} \sigma_{ij} = \delta \mathbf{D} : \boldsymbol{\sigma},$$

we can derive the virtual internal power in the form (3.6), where $\mathbf{L} = \frac{\partial \mathbf{v}}{\partial \mathbf{x}} = \left(\nabla \mathbf{v}\right)^T$ is the spatial velocity gradient, $\mathbf{D} = \frac{1}{2}\left(\mathbf{L} + \mathbf{L}^T\right)$ is rate of deformation tensor and $\mathbf{W} = \frac{1}{2}\left(\mathbf{L} - \mathbf{L}^T\right)$ is the spin tensor.

$$\delta P^{\text{int}} = \int_{\Omega} \delta D_{ij} \sigma_{ij} d\Omega = \int_{\Omega} \frac{\partial \left(\delta v_i\right)}{\partial x_j} \sigma_{ij} d\Omega \equiv \int_{\Omega} \delta L_{ij} \sigma_{ij} d\Omega = \int_{\Omega} \delta \mathbf{D} : \boldsymbol{\sigma} d\Omega \tag{3.6}$$

The second and third terms of the weak form gives the virtual external power arising from the external body forces $\mathbf{b}$ and prescribed tractions $\mathbf{t}^*$.

$$\delta P^{\text{ext}} = \int_{\Omega} \delta v_i \rho b_i d\Omega + \int_{\Gamma_t} \delta v_i t_i^* d\Gamma = \int_{\Omega} \delta \mathbf{v} \cdot \rho \mathbf{b} d\Omega + \int_{\Gamma_t} \delta \mathbf{v} \cdot \mathbf{t}^* d\Gamma \tag{3.7}$$

The last term in the weak form represents the virtual inertial (or kinetic) power.

$$\delta P^{\text{kin}} = \int_{\Omega} \delta v_i \rho \dot{v}_i d\Omega = \int_{\Omega} \delta \mathbf{v} \cdot \rho \dot{\mathbf{v}} d\Omega \tag{3.8}$$

Consequently, the weak form (3.5) can be reformulated as the following virtual power equation

$$\delta P = \delta P^{\text{int}} - \delta P^{\text{ext}} + \delta P^{\text{kin}} = 0. \tag{3.9}$$

Updated Lagrangian finite element discretization

Let the current domain Ω be subdivided into elements Ω_e, i.e. $\Omega = \bigcup_e \Omega_e$, which contains N_e nodes with the motion $\mathbf{x}_I(t)$, $I = 1$ to N_e. The approximation of the motion field $\mathbf{x}(\mathbf{X}, t)$ for the element Ω_e is assumed to be defined by the interpolation (or shape) functions $N_I(\mathbf{X})$ and motion of node $\mathbf{X}_I$ as follows

$$\mathbf{x}(\mathbf{X}, t) = N_I(\mathbf{X})\mathbf{x}_I(t) \text{ or } x_i(\mathbf{X}, t) = N_I(\mathbf{X})x_{iI}(t). \tag{3.10}$$

$x_{iI}(t)$ denotes the coordinates of node $\mathbf{x}_I(t)$ in the current configuration. In the reference configuration, we have

$$\mathbf{X} = \mathbf{x}(\mathbf{X}, 0) = N_I(\mathbf{X})\mathbf{x}_I(0) = N_I(\mathbf{X})\mathbf{X}_I. \tag{3.11}$$

Then, the equality $\mathbf{X}_J = N_I(\mathbf{X}_J)\mathbf{X}_I$ derives the condition (3.12), where δ_{IJ} is the Kronecker delta.

$$N_I\left(\mathbf{X}_J\right) = \delta_{IJ} \tag{3.12}$$

The displacement field $\mathbf{u}(\mathbf{X}, t)$ can be derived by

$$\mathbf{u}(\mathbf{X}, t) = \mathbf{x}(\mathbf{X}, t) - X = N_I(\mathbf{X})\mathbf{x}_I(t) - N_I(\mathbf{X})\mathbf{X}_I = N_I(\mathbf{X})\mathbf{u}_I(t), \tag{3.13}$$

where $\mathbf{u}_I(t) = \mathbf{x}_I(t) - \mathbf{X}_I$ is the displacement of node $\mathbf{X}_I$. The velocities are obtained by taking the material time derivative of the displacements, giving

$$\mathbf{v}(\mathbf{X}, t) = N_I(\mathbf{X})\dot{\mathbf{u}}_I(t) = N_I(\mathbf{X})\mathbf{v}_I(t) \text{ or } v_i(\mathbf{X}, t) = \frac{Du_i(\mathbf{X}, t)}{Dt} = N_I(\mathbf{X})v_{iI}(t). \tag{3.14}$$

Similarly, the accelerations $\mathbf{a}(\mathbf{X}, t)$ are defined by

$$\mathbf{a}(\mathbf{X}, t) = N_I(\mathbf{X})\dot{\mathbf{v}}_I(t) = N_I(\mathbf{X})\mathbf{a}_I(t) \text{ or } a_i(\mathbf{X}, t) = \frac{Dv_i(\mathbf{X}, t)}{Dt} = N_I(\mathbf{X})a_{iI}(t). \tag{3.15}$$

In the updated Lagrangian formulation, it is important to note that the shape functions are expressed with respect to the material coordinates, despite using the weak form in the current configuration. This choice is essential for Lagrangian meshes as it ensures that the time dependency in the finite element approximation of motion is solely attributed to the nodal variables.

The spatial velocity gradient $\mathbf{L}$ and rate of deformation tensor $\mathbf{D}$ are yielded by

$$\mathbf{L} = \mathbf{v}_I \nabla N_I = \mathbf{v}_I \frac{\partial N_I}{\partial \mathbf{x}} \text{ or } L_{ij} = v_{iI} \frac{\partial N_I}{\partial x_j}, \tag{3.16}$$

$$\mathbf{D} = \frac{1}{2}\left(\mathbf{v}_I \frac{\partial N_I}{\partial \mathbf{x}} + \frac{\partial N_I}{\partial \mathbf{x}} \mathbf{v}_I\right) \text{ or } D_{ij} = \frac{1}{2}\left(v_{iI} \frac{\partial N_I}{\partial x_j} + \frac{\partial N_I}{\partial x_j} v_{iI}\right). \tag{3.17}$$

Variations are approximated as

$$\delta \mathbf{v}(\mathbf{X}) = \delta \mathbf{v}_I N_I(\mathbf{X}) \text{ or } \delta v_i(\mathbf{X}) = \delta v_{il} N_I(\mathbf{X}). \tag{3.18}$$

As a results of these approximations, the principle of virtual power (3.5) is reformulated by

$$\delta v_{iI} \int_\Omega \frac{\partial N_I}{\partial x_j} \sigma_{ji} d\Omega - \delta v_{iI} \int_\Omega N_I \rho b_i d\Omega - \delta v_{iI} \int_{\Gamma_t} N_I t_i^* d\Gamma + \delta v_{iI} \int_\Omega N_I \rho \dot{v}_i d\Omega = 0. \tag{3.19}$$

The arbitrariness of the virtual nodal velocities δv_{iI} on the boundary Γ / Γ_u derives

$$\int_\Omega \frac{\partial N_I}{\partial x_j} \sigma_{ji} d\Omega - \int_\Omega N_I \rho b_i d\Omega - \int_{\Gamma_t} N_I t_i^* d\Gamma + \int_\Omega N_I \rho \dot{v}_i d\Omega = 0, \forall (I, i) \notin \Gamma_u. \tag{3.20}$$

Now we define nodal forces $\mathbf{f}^{int}$, $\mathbf{f}^{ext}$ and $\mathbf{f}^{kin}$ corresponding to the virtual internal, external and kinetic powers. The virtual power equations (3.6)–(3.8) yield

$$\delta P^{\text{int}} = \delta v_{iI} f_{iI}^{\text{int}} = \int_\Omega \frac{\partial (\delta v_i)}{\partial x_j} \sigma_{ji} d\Omega = \delta v_{iI} \int_\Omega \frac{\partial N_I}{\partial x_j} \sigma_{ji} d\Omega, \tag{3.21}$$

$$\delta P^{\text{ext}} = \delta v_{iI} f_{iI}^{\text{ext}} = \delta v_{iI} \int_\Omega N_I \rho b_i d\Omega + \delta v_{iI} \int_{\Gamma_t} N_I t_i^* d\Gamma, \tag{3.22}$$

$$\delta P^{\text{kin}} = \delta v_{iI} f_{iI}^{\text{kin}} = \delta v_{iI} \int_\Omega N_I \rho \dot{v}_i d\Omega. \tag{3.23}$$

This leads to the definition of internal and externalnodal forces $\mathbf{f}^{int}$ and $\mathbf{f}^{ext}$, giving

$$\mathbf{f}_I^{\text{int}} = \int_\Omega \nabla N_I \cdot \boldsymbol{\sigma} d\Omega \text{ or } f_{iI}^{\text{int}} = \int_\Omega \frac{\partial N_I}{\partial x_j} \sigma_{ji} d\Omega, \tag{3.24}$$

$$\mathbf{f}_I^{\text{ext}} = \int_\Omega N_I \rho \mathbf{b} d\Omega + \int_{\Gamma_t} N_I \mathbf{t}^* d\Gamma \text{ or } f_{iI}^{\text{ext}} = \int_\Omega N_I \rho b_i d\Omega + \int_{\Gamma_t} N_I t_i^* d\Gamma. \tag{3.25}$$

The kinetic forces are defined by

$$\mathbf{f}_I^{\text{kin}} = \int_\Omega \rho N_I \dot{\mathbf{v}} d\Omega = \mathbf{I} \int_\Omega \rho N_I N_J d\Omega \cdot \dot{\mathbf{v}}_J, \tag{3.26}$$

where $\mathbf{I} = \delta_{ij} e_i \otimes e_j$ is the unit tensor of second order. Introducing a mass matrix (or tensor) (3.27), we obtain the final form (3.28) of the kinetic forces.

$$\mathbf{M}_{IJ} = \mathbf{I} \int_{\Omega} \rho N_I N_J d\Omega \text{ or } M_{ijIJ} = \delta_{ij} \int_{\Omega} \rho N_I N_J d\Omega \tag{3.27}$$

$$\mathbf{f}_I^{\text{kin}} = \mathbf{M}_{IJ} \dot{\mathbf{v}}_J \text{ or } f_{iI}^{\text{kin}} = M_{ijIJ} \dot{v}_{jJ} \tag{3.28}$$

Consequently, we can concisely write the discrete approximation to the virtual power equation (3.9) as

$$\mathbf{M}_{IJ}\mathbf{a}_J + \mathbf{f}_I^{\text{int}} - \mathbf{f}_I^{\text{ext}} = 0, \ I \text{ and } J = 1 \text{ to } N_e. \tag{3.29}$$

In the process of assembling the finite element system, which involves converting local matrices and vectors from individual elements Ω_e into global ones for the entire domain Ω, the connectivity matrix $\mathbf{L}_e$ plays a crucial role. The connectivity matrix is a Boolean matrix that aids in this conversion process. A detailed discussion on this procedure can be found in the work by Belytschko [95][1]. For the sake of brevity, we will omit any node and element numbers in the following discussion and focus solely on the final governing equation (3.30) for the entire domain Ω, where $\mathbf{P}$ is the global internal nodal forces and $\mathbf{f}$ denotes the vector of the global external nodal forces.

$$\mathbf{M}\,\mathbf{a} + \mathbf{P} - \mathbf{f} = 0. \tag{3.30}$$

3.2 Nonlinear dynamic analysis

This section focuses on addressing the potential solutions for a dynamic problem involving physical/material nonlinearity, specifically plasticity. Mathematically, this nonlinearity manifests itself in the constitutive relations (equations (1.1)–(1.4)), thereby influencing the internal nodal forces $\mathbf{P}$ within the governing equation (3.30). By examining the constitutive relations, we gain insight into how this nonlinearity affects the overall behavior of the system (3.30). The equation (3.30) is also called the semidiscrete momentum equations since they have not been discretized in time. Below we introduce some time integration algorithms for discretization of time.

---

[1] Section 2.5: Element and Global Matrices.

3.2.1 Time integration algorithms

Time integration algorithms enables the simulation of a physical system's behavior through the discretization of time into smaller intervals or time steps. At each time step, the algorithm evaluates the system's current state based on its previous state and the governing equations. To perform these calculations, the algorithm relies on the current time, state variables, their relevant time derivatives, etc. By iteratively executing this process, the algorithm updates the quantities for subsequent time steps until the desired simulation time is reached. As a result, it effectively traces the system's evolution over time. Different time integration algorithms are available, including explicit methods like forward Euler or central difference method, and implicit methods such as the backward Euler method, Runge-Kutta methods, the Newmark β-method, the α-method [2] [98] etc. These methods enable the numerical solution of the system of differential equations at time t_{k+1}, represented by equation (3.31), by transforming it into a system of algebraic equations, which can be either linear or nonlinear in nature. This transformation allows for the application of efficient numerical techniques to obtain approximate solutions to the dynamic equilibrium problem. Here, we will provide a brief introduction to two methods: one explicit and one implicit.

$$\mathbf{M}\,\mathbf{a}_{k+1} + \mathbf{P}_{k+1}(\mathbf{u}_{k+1}) - \mathbf{f}_{k+1} = 0 \tag{3.31}$$

Explicit central difference method

The central difference method is a commonly used approach for time integration systems. This explicit calculation scheme can be represented as follows

$$\begin{aligned} \mathbf{u}_{k+1} &= \mathbf{u}_k + \Delta t\,\mathbf{v}_k + \frac{1}{2}\Delta t^2\,\mathbf{a}_k = \tilde{\mathbf{u}}_{k+1}, \\ \mathbf{v}_{k+1} &= \mathbf{v}_k + \frac{1}{2}\Delta t\,\left(\mathbf{a}_k + \mathbf{a}_{k+1}\right) = \tilde{\mathbf{v}}_{k+1} + \frac{1}{2}\Delta t\,\mathbf{a}_{k+1}, \end{aligned} \tag{3.32}$$

where $\tilde{\mathbf{u}}_{k+1}$ and $\tilde{\mathbf{v}}_{k+1}$ are values relying only on the solution at $t = t_k$. Compared to the forward Euler method, the central difference method allows for $\mathbf{P}_{k+1}(\mathbf{u}_{k+1})$ to be calculated by using values only from the previous time step, i.e. without depending on $\mathbf{a}_{k+1}$. Consequently, it may transform dynamic equations (3.31) to

---

[2] The α-method is available in ABAQUS/Standard package.

linear algebraic equations with one unknown value $\mathbf{a}_{k+1}$. This characteristic sets it apart as a more convenient approach for dynamic analysis. Thus, it is widely used in many commercial simulation packages, for in stance, in ABAQUS/Explicit package. Nevertheless, explicit schemes are conditionally stable only when the time step Δt fulfils $\Delta t \leq \Delta t_{crit}$. Here, Δt_{crit} is determined by the minimum time required for "wave propagation" across any element or, alternatively, the highest "frequency" present in the finite element mesh [96] [3].

Newmark β-method

The Newmark β-method as a method of time integration is specifically designed to solve systems of second-order differential equations. It finds applications in various fields, including physical and/or engineering problems, and provides an effective approach for numerically solving complex systems such as dynamic response systems. It enables calculation of displacements, velocities and accelerations with the use of

$$\begin{aligned}
\mathbf{u}_{k+1} &= \mathbf{u}_k + \int_0^{\Delta t} \mathbf{v}(t')\, dt' \\
&= \mathbf{u}_k + \Delta t\, \mathbf{v}_k + \left(\frac{1}{2} - \beta\right) \Delta t^2\, \mathbf{a}_k + \beta \Delta t^2\, \mathbf{a}_{k+1} = \tilde{\mathbf{u}}_{k+1} + \beta \Delta t^2\, \mathbf{a}_{k+1}, \\
\mathbf{v}_{k+1} &= \mathbf{v}_k + \int_0^{\Delta t} \mathbf{a}(t')\, dt' \\
&= \mathbf{v}_k + (1-\gamma)\Delta t\, \mathbf{a}_k + \gamma \Delta t\, \mathbf{a}_{k+1} = \tilde{\mathbf{v}}_{k+1} + \gamma \Delta t\, \mathbf{a}_{k+1},
\end{aligned} \tag{3.33}$$

where β and γ are parameters, $\tilde{\mathbf{u}}_{k+1}$ and $\tilde{\mathbf{v}}_{k+1}$ are values relying only on the solution at $t = t_k$. Parameters β and γ are chosen to ensure the accuracy and stability. The implicit scheme is unconditionally stable for $\beta \geq \frac{\gamma}{2} \geq \frac{1}{4}$. It transforms dynamic equations (3.31) to non-linear algebraic equations with one unknown value $\mathbf{a}_{k+1}$, which may be solved by, for instance, Newton-Raphson method and its modifications. For more detailed discussions on cases with conditional stability, refer to the work by Belytschko [95] [4]. Notably, the explicit central difference and undamped trapezoidal methods are special cases of Newmark β-method, where $\beta = 0, \gamma = \frac{1}{2}$ and $\beta = \frac{1}{4}, \gamma = \frac{1}{2}$, respectively.

In addition to time integration algorithms, accurately calculating the constitutive

---

[3] chapter 2: Galerkin Method of Approximation, page 31

[4] chapter 6: Solution Methods and Stability, page 339

equations within $\mathbf{P}_{k+1}(\mathbf{u}_{k+1})$ is also crucial for solving the equations (3.31). Specifically, it is necessary to compute the stress increments $\Delta\boldsymbol{\sigma}$ with a given value of $\Delta\mathbf{u}$, therefore, the strain increment $\Delta\boldsymbol{\varepsilon}$.

3.2.2 Computation of stress increments in problems of isotropic plasticity J_2

Elastomeric-plastic problem has a non-linear characteristic due to non-linear constitutive relations. In terms of the elasto-plastic modulus matrix $\mathbf{D}^{\star}_{\text{ep}}(\boldsymbol{\sigma}, \boldsymbol{\varepsilon})$ given by Zienkiewicz [96] [5], this means that the stresses have to be integrated as $\Delta\boldsymbol{\sigma} = \int_0^{\Delta\varepsilon} \mathbf{D}^{\star}_{\text{ep}}(\boldsymbol{\sigma}, \boldsymbol{\varepsilon}')\mathrm{d}\boldsymbol{\varepsilon}'$. In the case of isotropic J_2 plasticity, we solve the following governing differential equations (3.34)–(3.36) equivalent to relations (1.1)–(1.3) with initial conditions (3.37) and a norm of a tensor giving $|\mathbf{s}| = (\mathbf{s} : \mathbf{s})^{\frac{1}{2}}$. The predictor-corrector algorithm – the return mapping algorithm – is commonly used to integrate governing equations (3.34)–(3.36). The von-Mises yield surface equation (3.38) (or 1.4) can be solved by Newton–Raphson method.

$$\begin{aligned} \dot{\mathbf{s}} &= 2G\,\mathrm{dev}\,(\dot{\boldsymbol{\varepsilon}} - \dot{\boldsymbol{\varepsilon}}^p) = 2G\,\mathrm{dev}\,\dot{\boldsymbol{\varepsilon}} - 2G\dot{\boldsymbol{\varepsilon}}^p \\ &= 2G\,\mathrm{dev}\,\dot{\boldsymbol{\varepsilon}} - 2G\gamma\mathbf{n} \end{aligned} \tag{3.34}$$

$$\dot{T} = \frac{\eta\gamma}{\rho C_v}\boldsymbol{\sigma} : \mathbf{n} \tag{3.35}$$

$$\begin{aligned} \dot{\bar{\varepsilon}}^p &= \left(\frac{2}{3}\dot{\boldsymbol{\varepsilon}}^p : \dot{\boldsymbol{\varepsilon}}^p\right)^{\frac{1}{2}} = \sqrt{\frac{2}{3}}\gamma(\mathbf{n} : \mathbf{n})^{\frac{1}{2}} \\ &= \sqrt{\frac{2}{3}}\gamma \end{aligned} \tag{3.36}$$

$$\mathbf{s}(t_k) = \mathbf{s}_k,\ T(t_k) = T_k,\ \bar{\varepsilon}^p(t_k) = \bar{\varepsilon}^p_k \tag{3.37}$$

$$f(\gamma) = \sqrt{\frac{3}{2}}|\mathbf{s}| - \sigma^y(\gamma) = 0 \tag{3.38}$$

Return mapping algorithm for the time integration of stress

Based on the backward Euler algorithm, the return mapping algorithm increments

---

[5] chapter 4: Inelastic and Nonlinear Materials, page 95

the stress tensor $\boldsymbol{\sigma}$, plastic strain tensor $\boldsymbol{\varepsilon}^p$ and the equivalent plastic strain $\bar{\varepsilon}^p$. It introduces a trial deviatoric stress tensor $\mathbf{s}_{k+1}^{\mathrm{tr}}$ (the stress predictor at time t_{k+1}) shown inexpression (3.39) and utilizes the coaxiality between tensors $\mathbf{s}_{k+1}$, $\mathbf{s}_{k+1}^{\mathrm{tr}}$ and $\dot{\boldsymbol{\varepsilon}}_{k+1}^p$. In isotropic J_2 plasticity problems, a proportional factor $m = \frac{|\mathbf{s}_{k+1}|}{|\mathbf{s}_{k+1}^{\mathrm{tr}}|}$ arising due to the coaxiality of tensors $\mathbf{s}_{k+1}$ and $\mathbf{s}_{k+1}^{\mathrm{tr}}$ plays a crucial role in simplifying the calculation procedure.

$$\mathbf{s}_{k+1}^{\mathrm{tr}} = \mathbf{s}_k + 2G\,\mathrm{dev}(\Delta\boldsymbol{\varepsilon}_{k+1}) \tag{3.39}$$

Using the backward Euler method (3.40), the governing equations (3.34)–(3.36) can be integrated as given in equations (3.41)–(3.43), where $\Delta\bar{\varepsilon}_{k+1}^p = \bar{\varepsilon}_{k+1}^p - \bar{\varepsilon}_k^p$ and $\sigma_{k+1}^y = \sigma^y(t_{k+1})$.

$$y_{k+1} = y_k + \int_0^{\Delta t} f(t,y)dt \approx y_k + \Delta t f\left(t_{k+1}, y_{k+1}\right) \tag{3.40}$$

$$\begin{aligned} \mathbf{s}_{k+1} &= \mathbf{s}_k + 2G\,\mathrm{dev}(\Delta\boldsymbol{\varepsilon}_{k+1}) - 2G\Delta t\gamma_{k+1}\mathbf{n}_{k+1} \\ &= \mathbf{s}_{k+1}^{\mathrm{tr}} - \sqrt{6}G\Delta\bar{\varepsilon}_{k+1}^p\mathbf{n}_{k+1} \end{aligned} \tag{3.41}$$

$$\begin{aligned} T_{k+1} &= T_k + \frac{1}{\rho C_v}\int_0^{\Delta t} \eta\gamma|\mathbf{s}|dt' = T_k + \frac{\eta_{k+1}}{\rho C_v}\Delta t\gamma_{k+1}|\mathbf{s}_{k+1}| \\ &= T_k + \frac{\eta_{k+1}}{\rho C_v}\Delta\bar{\varepsilon}_{k+1}^p\sigma_{k+1}^y \end{aligned} \tag{3.42}$$

$$\begin{aligned} \bar{\varepsilon}_{k+1}^p &= \bar{\varepsilon}_k^p + \sqrt{\frac{2}{3}}\Delta t\gamma_{k+1} \\ &= \bar{\varepsilon}_k^p + \Delta\varepsilon_{k+1}^p \end{aligned} \tag{3.43}$$

Equation (3.42) utilizes the equality $\boldsymbol{\sigma} : \mathbf{n} = \mathbf{s} : \mathbf{n} = |\mathbf{s}|$. The coaxiality of tensors $\mathbf{s}_{k+1}$ and $\mathbf{s}_{k+1}^{\mathrm{tr}}$ is demonstrated in equation (3.41), yielding the relation

$$|\mathbf{s}_{k+1}| = |\mathbf{s}_{k+1}^{\mathrm{tr}}| - \sqrt{6}G\Delta\bar{\varepsilon}_{k+1}^p.$$

Subsequently, the von-Mises yield surface equation (3.38) can be derived as shown in equation (3.44), where $\bar{\sigma}_{k+1}^{\mathrm{tr}} = \left(\frac{3}{2}\mathbf{s}_{k+1}^{\mathrm{tr}} : \mathbf{s}_{k+1}^{\mathrm{tr}}\right)^{\frac{1}{2}} = \sqrt{\frac{3}{2}}\left|\mathbf{s}_{k+1}^{\mathrm{tr}}\right|$.

$$f(\Delta\bar{\varepsilon}_{k+1}^p) = \bar{\sigma}_{k+1}^{\mathrm{tr}} - 3G\Delta\bar{\varepsilon}_{k+1}^p - \sigma^y(\Delta\bar{\varepsilon}_{k+1}^p) = 0 \tag{3.44}$$

As a result, the solution to the set of governing equations (3.34)–(3.38) is reformulated as the solution to an algebraic scalar equation (3.44) with respect to the scalar variable $\Delta\overline{\varepsilon}^p_{k+1}$. The coaxiality of tensors $\mathbf{s}_{k+1}$ and $\mathbf{s}^{\mathrm{tr}}_{k+1}$, along with the von-Mises yield surface equation, also gives

$$\mathbf{s}_{k+1} = \frac{|\mathbf{s}_{k+1}|}{|\mathbf{s}^{\mathrm{tr}}_{k+1}|}\mathbf{s}^{\mathrm{tr}}_{k+1} = \frac{\sigma^y_{k+1}}{\bar{\sigma}^{\mathrm{tr}}_{k+1}}\mathbf{s}^{\mathrm{tr}}_{k+1} = m\,\mathbf{s}^{\mathrm{tr}}_{k+1}.$$

The proportional factor $m = \frac{\sigma^y_{k+1}}{\bar{\sigma}^{\mathrm{tr}}_{k+1}}$ can be used to calculate the plastic strain increment tensor as follows

$$\Delta\boldsymbol{\varepsilon^p}_{k+1} = \frac{\mathbf{s}^{\mathrm{tr}}_{k+1} - \mathbf{s}_{k+1}}{2G} = \frac{1-m}{2G}\mathbf{s}^{\mathrm{tr}}_{k+1}.$$

Therefore, a simple return mapping algorithm can be summarized in the following scheme:

1. Solve the algebraic scalar equation (3.44) to find the increment of equivalent plastic strain $\Delta\overline{\varepsilon}^p_{k+1}$. Update the equivalent plastic strain $\overline{\varepsilon}^p_{k+1}$ and its rate $\dot{\overline{\varepsilon}}^p_{k+1} = \Delta\overline{\varepsilon}^p_{k+1}/\Delta t$.
2. Calculate the trial stress tensor $\mathbf{s}^{\mathrm{tr}}_{k+1}$, value of isotropic hardening function $\sigma^y_{k+1} = \sigma^y(\Delta\overline{\varepsilon}^p_{k+1})$ and the proportional factor $m = \frac{\sigma^y_{k+1}}{\bar{\sigma}^{\mathrm{tr}}_{k+1}}$.
3. Determine the increment of plastic strain tensor $\Delta\boldsymbol{\varepsilon^p}_{k+1}$ by the value of m and $\mathbf{s}^{\mathrm{tr}}_{k+1}$ and update the deviatoric stress tensor $\mathbf{s}_{k+1}$ and plastic strain tensor $\boldsymbol{\varepsilon^p}_{k+1}$.
4. Update the temperature T varied in response to the plastic dissipation, following equation (3.42).
5. Switch to the next time step.

Newton–Raphson method for solution of the yield surface equation

Several iterative methods exist to solve the yield surface equation (3.44) with one variable $\Delta\overline{\varepsilon}^p_{k+1}$. Among these methods, the Newton-Raphson (NR) method is widely used due to its effectiveness. However, before delving into the details of the NR method, it would be helpful to provide a brief introduction to the explicit method for finding a preliminary solution, which can also serve as a way of providing the initial approximation for the NR method. The hardening function $\sigma^y(\overline{\varepsilon}^p, \dot{\overline{\varepsilon}}^p, T)$

can be expanded as

$$\sigma^y_{k+1} \approx \sigma^y_k + \frac{\partial \sigma^y_k}{\partial \bar{\varepsilon}^p}\Delta \bar{\varepsilon}^p + \frac{\partial \sigma^y_k}{\partial \dot{\bar{\varepsilon}}^p}\Delta\left(\dot{\bar{\varepsilon}}^p\right) + \frac{\partial \sigma^y_k}{\partial T}\Delta T,$$

resulting in equation (3.45). To simplify the solution, the expression (3.46) instead of (3.42) is used. This substitution eliminates the dependence of η_{k+1} and σ^y_{k+1} on the value $\Delta\bar{\varepsilon}^p_{k+1}$. Consequently, the increment of equivalent plastic strain can be approximated calculated using equation (3.47). This explicit method requires the condition $f(\Delta\bar{\varepsilon}^p_{k+1}) \approx 0$ to be satisfied at each time step in order to ensure satisfactory accuracy.

$$f(\Delta\bar{\varepsilon}^p_{k+1}) \approx \bar{\sigma}^{\mathrm{tr}}_{k+1} - 3G\Delta\bar{\varepsilon}^p_{k+1} - (\sigma^y_k + \frac{\partial \sigma^y_k}{\partial \bar{\varepsilon}^p}\Delta \bar{\varepsilon}^p + \frac{\partial \sigma^y_k}{\partial \dot{\bar{\varepsilon}}^p}\Delta\left(\dot{\bar{\varepsilon}}^p\right) + \frac{\partial \sigma^y_k}{\partial T}\Delta T) \approx 0 \quad (3.45)$$

$$T_{k+1} = T_k + \frac{\sigma^y_k \eta_k}{\rho C_v}\Delta\bar{\varepsilon}^p_{k+1} \quad (3.46)$$

$$\Delta\bar{\varepsilon}^p_{k+1} = \frac{\bar{\sigma}^{\mathrm{tr}}_{k+1} - \sigma^y_k}{3G + \frac{\partial \sigma^y_k}{\partial \bar{\varepsilon}^p} + \frac{1}{\Delta t}\frac{\partial \sigma^y_k}{\partial \dot{\bar{\varepsilon}}^p} + \frac{\eta_k}{\rho C_v}\sigma^y_k\frac{\partial \sigma^y_k}{\partial T}} \quad (3.47)$$

The Newton-Raphson method is based on the iterative procedure (3.48), where x denotes the variable $\Delta\bar{\varepsilon}^p_{k+1}$ and x_n represents the value of x at n-th iteration, i.e. $x_n = \Delta\bar{\varepsilon}^{p(n)}_{k+1}$. The derivative function $f'(x)$ is given in expression (3.49). Solution of the explict method (3.47) can serve as the initial approximation of the iterative method as shown in expression (3.50). Hence, equations (3.48)–(3.50) establish the NR method.

$$x_{n+1} = x_n - \frac{f(x_n)}{f'(x_n)} \quad (3.48)$$

$$f'(x) = -3G - \frac{\partial \sigma^y}{\partial \bar{\varepsilon}^p} - \frac{1}{\Delta t}\frac{\partial \sigma^y}{\partial \dot{\bar{\varepsilon}}^p} - \frac{\sigma^y \eta}{\rho C_v}\frac{\partial \sigma^y}{\partial T} \quad (3.49)$$

$$x_0 = \frac{\bar{\sigma}^{\mathrm{tr}}_{k+1} - \sigma^y_k}{3G + \frac{\partial \sigma^y_k}{\partial \bar{\varepsilon}^p} + \frac{1}{\Delta t}\frac{\partial \sigma^y_k}{\partial \dot{\bar{\varepsilon}}^p} + \frac{\eta_k}{\rho C_v}\sigma^y_k\frac{\partial \sigma^y_k}{\partial T}} \quad (3.50)$$

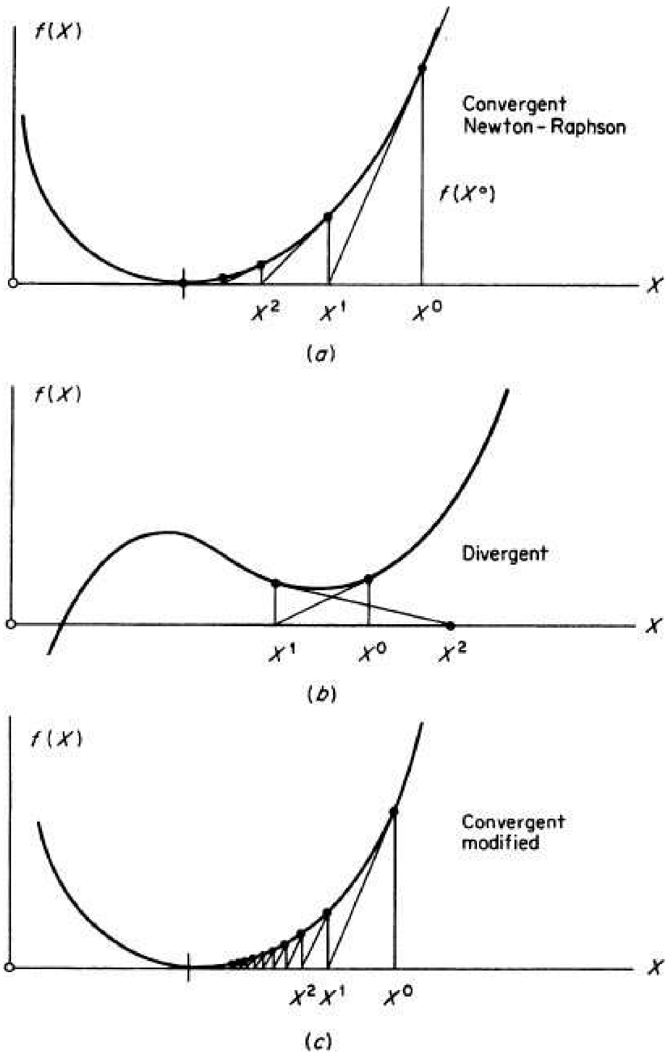

Figure 3.1: Example of convergence and divergence cases for the Newton-Raphson Method [99]

3.3 A calculation scheme suitable for the RP model

The Newton-Raphson (NR) method is renowned for its convenience and rapid convergence rate. However, certain challenges can arise when employing the NR method. One such challenge occurs when the function $f(x)$ is non-monotonic, and its derivative $f'(x)$ vanishes at certain points during the iteration process as shown in figure 3.1 [99]. Additionally, difficulties may arise when $f(x)$ lacks a derivative at specific points, such as in the case of a piecewise function. For dynamic plasticity problems, a non-monotonic behavior of $f(x)$ may arise due to the yield drop phenomenon, thermal softening under impact loads, etc. Thus, a safe version of NR method [100] is used in my work.

3.3.1 Safe version of the Newton–Raphson method

The safe version of the Newton-Raphson (NR) method combines both the NR procedure and the bisection method to ensure reliable convergence [100]. The bisection method utilizes an interval $[x_{\mathrm{min}}, x_{\mathrm{max}}]$ at each iterative step and considers the midpoint $x_{\mathrm{mid}} = \frac{x_{\mathrm{max}}+x_{\mathrm{min}}}{2}$ as the new boundary for the subsequent interval. The determination of the upper or lower boundary is based on the sign of the product $f(x_{\mathrm{mid}})f(x_{\mathrm{min}})$. In the safe version of the NR method, after each iteration, the interval is adjusted by replacing one of its boundaries with the newly computed solution. If the obtained solution from the NR method at the current iteration, defined in equation (3.48), falls outside the interval bounds, it is considered invalid. In such cases, a bisection step is performed to bring the solution back within the interval, i.e. x_{mid} is the new boundary. This iterative process guarantees that subsequent iterations remain within the specified interval range, ensuring convergence towards the desired solution.

3.3.2 Implementation in commercial software package

The commercial software package ABAQUS/Explicit incorporates the explicit central difference method, as discussed in Section 3.2.1, for solving the dynamic equation (3.31). To facilitate this solution approach, the subroutine VUMAT is available, allowing users to integrate their own custom programs responsible for computing stress increments with the ABAQUS/Explicit procedure. This combination of user-defined programs and ABAQUS/Explicit functionality enhances the flexibility and versatility of the software package for a wide range of applications. In the present study, the safe version of the Newton-Raphson (NR) method has been integrated into a Fortran-based VUMAT subroutine. The hardening function $\sigma_y(\cdot)$ follows the simplified version of the RP model (2.22). It is important to highlight certain key aspects of the RP model that are particularly relevant to implementation of the subroutine.

At first, scalar variables $\sigma, \dot{\varepsilon}, \dot{\varepsilon}_p$ need be related to invariants of tensors $\boldsymbol{\sigma}, \dot{\boldsymbol{\varepsilon}}, \dot{\boldsymbol{\varepsilon}}^p$. In cases of one-dimension stress state, we have following stress and strain tensors, where $\dot{\theta} = \mathrm{tr}\,\dot{\boldsymbol{\varepsilon}} = \mathrm{tr}\,\dot{\boldsymbol{\varepsilon}}^e$ characterises the change of element volume, ν is the Poisson's ratio.

$$\boldsymbol{\sigma} = \sigma\mathbf{e}_1\mathbf{e}_1, \dot{\boldsymbol{\varepsilon}} = \dot{\varepsilon}\mathbf{e}_1\mathbf{e}_1 + \frac{1}{2}\left(\dot{\theta} - \dot{\varepsilon}\right)\mathbf{e}_2\mathbf{e}_2 + \frac{1}{2}\left(\dot{\theta} - \dot{\varepsilon}\right)\mathbf{e}_3\mathbf{e}_3,$$
$$\dot{\boldsymbol{\varepsilon}}^e = \dot{\varepsilon}_e\mathbf{e}_1\mathbf{e}_1 - \nu\dot{\varepsilon}_e\mathbf{e}_2\mathbf{e}_2 - \nu\dot{\varepsilon}_e\mathbf{e}_3\mathbf{e}_3, \dot{\boldsymbol{\varepsilon}}^p = \dot{\varepsilon}_p\mathbf{e}_1\mathbf{e}_1 - \frac{1}{2}\dot{\varepsilon}_p\mathbf{e}_2\mathbf{e}_2 - \frac{1}{2}\dot{\varepsilon}_p\mathbf{e}_3\mathbf{e}_3.$$

According to expressions (3.36) and (3.38), invariants $\bar{\sigma}(\mathbf{s}) = \left(\frac{3}{2}\mathbf{s} : \mathbf{s}\right)^{\frac{1}{2}}$ and $\dot{\bar{\varepsilon}}^p$ yield

$$\begin{aligned} \bar{\sigma}(\mathbf{s}) &= \left(\frac{3}{2}\mathbf{s} : \mathbf{s}\right)^{\frac{1}{2}} = \sigma, \\ \dot{\bar{\varepsilon}}^p &= \left(\frac{2}{3}\dot{\boldsymbol{\varepsilon}}^p : \dot{\boldsymbol{\varepsilon}}^p\right)^{\frac{1}{2}} = \dot{\varepsilon}_p. \end{aligned} \tag{3.51}$$

The volume change described by θ is not considered in the one-dimensional plasticity problem, thus the scalar variable $\dot{\varepsilon}$ is not equal to $\left(\frac{2}{3}\dot{\boldsymbol{\varepsilon}} : \dot{\boldsymbol{\varepsilon}}\right)^{\frac{1}{2}}$. Nevertheless, we may have

$$\dot{\bar{\varepsilon}} = \frac{\dot{\theta}}{3} + \left(\frac{2}{3}\operatorname{dev}\dot{\boldsymbol{\varepsilon}} : \operatorname{dev}\dot{\boldsymbol{\varepsilon}}\right)^{\frac{1}{2}} = \dot{\varepsilon}. \tag{3.52}$$

Consequently, we solve the equations (3.34)–(3.38), where the hardening function σ^y is defined by

$$\begin{gathered} \sigma^y\left(\bar{\varepsilon}, \bar{\varepsilon}^p, \dot{\bar{\varepsilon}}, T\right) = \sigma_c\left(\bar{\varepsilon}^p, T\right) g(\bar{\varepsilon}, \dot{\bar{\varepsilon}}, T), \\ g(\bar{\varepsilon}, \dot{\bar{\varepsilon}}, T) = \begin{cases} \left(\frac{\dot{\bar{\varepsilon}}\tau(1+\alpha)}{\bar{\varepsilon}}\right)^{1/\alpha}, & \frac{\bar{\varepsilon}}{\dot{\bar{\varepsilon}}\tau} \leqslant 1, \\ \left(\frac{\dot{\bar{\varepsilon}}\tau(1+\alpha)\bar{\varepsilon}^{\alpha}}{\bar{\varepsilon}^{1+\alpha} - (\bar{\varepsilon} - \dot{\bar{\varepsilon}}\tau)^{1+\alpha}}\right)^{1/\alpha}, & \frac{\bar{\varepsilon}}{\dot{\bar{\varepsilon}}\tau} > 1. \end{cases}, \ \tau = \tau(T). \end{gathered} \tag{3.53}$$

In the model (3.53), the value $\bar{\varepsilon}^{\alpha}$ or $\bar{\varepsilon}^{1+\alpha}$ can be extremely minor, especially during the initial stages of plastic deformation when ε is much less than 1 and α is relatively large. In contrast, the value of $\sigma_c\left(\bar{\varepsilon}^p, T\right)$ is significantly larger than $\bar{\varepsilon}^{\alpha}$ or $\bar{\varepsilon}^{1+\alpha}$. The stark difference in magnitude between these values can lead to notable cumulative imprecision in the iterative calculation procedure. Therefore, it is necessary to adjust the form of the function $g(\bar{\varepsilon}, \dot{\bar{\varepsilon}}, T)$ to mitigate inaccuracies that may arise during the calculation process.

Let's denote a dimensionless value $\frac{\bar{\varepsilon}}{\dot{\bar{\varepsilon}}\tau}$ by ξ. Then, the function $g(\bar{\varepsilon}, \dot{\bar{\varepsilon}}, T)$ can be reformulated as $g(\xi)$ given in equation (3.54), where $\xi = \xi(\bar{\varepsilon}, \dot{\bar{\varepsilon}}, T) = \frac{\bar{\varepsilon}}{\dot{\bar{\varepsilon}}\tau(T)}$. Partial derivatives used in the safe version of NR method are shown in expression (3.55).

$$g(\xi) = \left(\frac{(1+\alpha)\xi^{\alpha}}{\xi^{1+\alpha} - (\xi-1)^{1+\alpha}H(\xi-1)}\right)^{1/\alpha} = \begin{cases} \left(\frac{1+\alpha}{\xi}\right)^{1/\alpha}, & \xi \le 1 \\ \left(\frac{1+\alpha}{\xi-(\xi-1)\left(1-\frac{1}{\xi}\right)^{\alpha}}\right)^{1/\alpha}, & \xi > 1 \end{cases} \tag{3.54}$$

$$\begin{aligned} &\frac{\partial\sigma}{\partial\bar{\varepsilon}} = \sigma_c\frac{\partial g}{\partial\bar{\varepsilon}}, \quad \frac{\partial\sigma}{\partial\bar{\varepsilon}^p} = \frac{\partial\sigma_c}{\partial\bar{\varepsilon}^p}g, \\ &\frac{\partial\sigma}{\partial\dot{\bar{\varepsilon}}} = \sigma_c\frac{\partial g}{\partial\dot{\bar{\varepsilon}}}, \quad \frac{\partial\sigma}{\partial T} = \frac{\partial\sigma_c}{\partial T}g + \sigma_c\frac{\partial\tau}{\partial T}\frac{\partial g}{\partial\tau}, \end{aligned} \tag{3.55}$$

Values $\frac{\partial g(\xi)}{\partial\xi}$, $\frac{\partial g(\xi)}{\partial\dot{\bar{\varepsilon}}}$ and $\frac{\partial g(\xi)}{\partial\tau}$ can be calculated in two cases. If $\xi \le 1$, we may have

$$\begin{aligned} \frac{dg(\xi)}{d\xi} &= (1+\alpha)^{1/\alpha}\left(-\frac{1}{\alpha}\right)\xi^{-1/\alpha-1} = -\frac{(1+\alpha)^{1/\alpha}}{\alpha\xi^{1+1/\alpha}} = -\frac{g(\xi)}{\alpha\xi}, \\ \frac{\partial g(\xi)}{\partial\bar{\varepsilon}} &= \frac{1}{\tau\dot{\bar{\varepsilon}}}\frac{dg(\xi)}{d\xi} = \frac{1}{\tau\dot{\bar{\varepsilon}}}\left(-\frac{g(\xi)}{\alpha\xi}\right) = -\frac{g(\xi)}{\alpha\bar{\varepsilon}}, \\ \frac{\partial g(\xi)}{\partial\dot{\bar{\varepsilon}}} &= -\frac{\xi}{\dot{\bar{\varepsilon}}}\frac{dg(\xi)}{d\xi} = \frac{(1+\alpha)^{1/\alpha}}{\alpha\dot{\bar{\varepsilon}}}\left(\frac{1}{\xi}\right)^{1/\alpha} = \left(\frac{1+\alpha}{\xi}\right)^{1/\alpha}(\alpha\dot{\bar{\varepsilon}})^{-1} = \frac{g(\xi)}{\alpha\dot{\bar{\varepsilon}}}, \\ \frac{\partial g(\xi)}{\partial\tau} &= -\frac{\xi}{\tau}\frac{dg(\xi)}{d\xi} = \left(\frac{1+\alpha}{\xi}\right)^{1/\alpha}(\alpha\tau)^{-1} = \frac{g(\xi)}{\alpha\tau}. \end{aligned} \tag{3.56}$$

In case of $\xi > 1$, the following equation is derived

$$\begin{aligned} \frac{dg(\xi)}{d\xi} &= -\frac{\xi-(\xi+\alpha)\left(1-\frac{1}{\xi}\right)^{\alpha}}{\xi-(\xi-1)\left(1-\frac{1}{\xi}\right)^{\alpha}}\frac{g(\xi)}{\alpha\xi}, \\ \frac{\partial g(\xi)}{\partial\bar{\varepsilon}} &= \frac{1}{\tau\dot{\bar{\varepsilon}}}\frac{dg(\xi)}{d\xi} = -\frac{\xi-(\xi+\alpha)\left(1-\frac{1}{\xi}\right)^{\alpha}}{\xi-(\xi-1)\left(1-\frac{1}{\xi}\right)^{\alpha}}\frac{g(\xi)}{\alpha\bar{\varepsilon}}, \\ \frac{\partial g(\xi)}{\partial\dot{\bar{\varepsilon}}} &= -\frac{\xi}{\dot{\bar{\varepsilon}}}\frac{dg(\xi)}{d\xi} = \frac{\xi-(\xi+\alpha)\left(1-\frac{1}{\xi}\right)^{\alpha}}{\xi-(\xi-1)\left(1-\frac{1}{\xi}\right)^{\alpha}}\frac{g(\xi)}{\alpha\dot{\bar{\varepsilon}}}, \\ \frac{\partial g(\xi)}{\partial\tau} &= -\frac{\xi}{\tau}\frac{dg(\xi)}{d\xi} = \frac{\xi-(\xi+\alpha)\left(1-\frac{1}{\xi}\right)^{\alpha}}{\xi-(\xi-1)\left(1-\frac{1}{\xi}\right)^{\alpha}}\frac{g(\xi)}{\alpha\tau}. \end{aligned} \tag{3.57}$$

In summary, we have partial derivatives given in equations (3.58), (3.59) and (3.60).

$$\frac{\partial g(\xi)}{\partial \bar{\varepsilon}} = \begin{cases} -\frac{g(\xi)}{\alpha \bar{\varepsilon}}, & \xi \leq 1 \\ -\frac{\xi - (\xi+\alpha)\left(1-\frac{1}{\xi}\right)^{\alpha}}{\xi - (\xi-1)\left(1-\frac{1}{\xi}\right)^{\alpha}} \frac{g(\xi)}{\alpha \bar{\varepsilon}}, & \xi > 1 \end{cases} \tag{3.58}$$

$$\frac{\partial g(\xi)}{\partial \dot{\bar{\varepsilon}}} = \begin{cases} \frac{g(\xi)}{\alpha \dot{\bar{\varepsilon}}}, & \xi \leq 1 \\ \frac{\xi - (\xi+\alpha)\left(1-\frac{1}{\xi}\right)^{\alpha}}{\xi - (\xi-1)\left(1-\frac{1}{\xi}\right)^{\alpha}} \frac{g(\xi)}{\alpha \dot{\bar{\varepsilon}}}, & \xi > 1 \end{cases} \tag{3.59}$$

$$\frac{\partial g(\xi)}{\partial \tau} = \begin{cases} \frac{g(\xi)}{\alpha \tau}, & \xi \leq 1 \\ \frac{\xi - (\xi+\alpha)\left(1-\frac{1}{\xi}\right)^{\alpha}}{\xi - (\xi-1)\left(1-\frac{1}{\xi}\right)^{\alpha}} \frac{g(\xi)}{\alpha \tau}, & \xi > 1 \end{cases} \tag{3.60}$$

Calculation flowchart of the safe version of NR method for dynamic plasticity problem with the RP model is illustrated in figure 3.2. The initial point x_0 of NR method for the RP model differs from that discussed in equation (3.50), giving

$$x_0 = \frac{\bar{\sigma}^{\mathrm{tr}}_{k+1} - \sigma^y_k - \frac{\partial \sigma^y_k}{\partial \bar{\varepsilon}} \Delta \bar{\varepsilon}}{3G + \frac{\partial \sigma^y_k}{\partial \bar{\varepsilon}^p} + \frac{1}{\Delta t}\frac{\partial \sigma^y_k}{\partial \dot{\bar{\varepsilon}}^p} + \frac{\eta_k}{\rho C_v} \sigma^y_k \frac{\partial \sigma^y_k}{\partial T}}. \tag{3.61}$$

3.4 Conclusion to the chapter

In this chapter, time integration algorithms, return mapping algorithm for time integration of stress and a safe version of the Newton–Raphson method for solving algebraic equations are discussed. A calculation scheme suitable for the simplified version of RP model is presented. The developed calculation approaches are used to perform simulation of dynamic plasticity problems. The results are discussed in section 4.3.

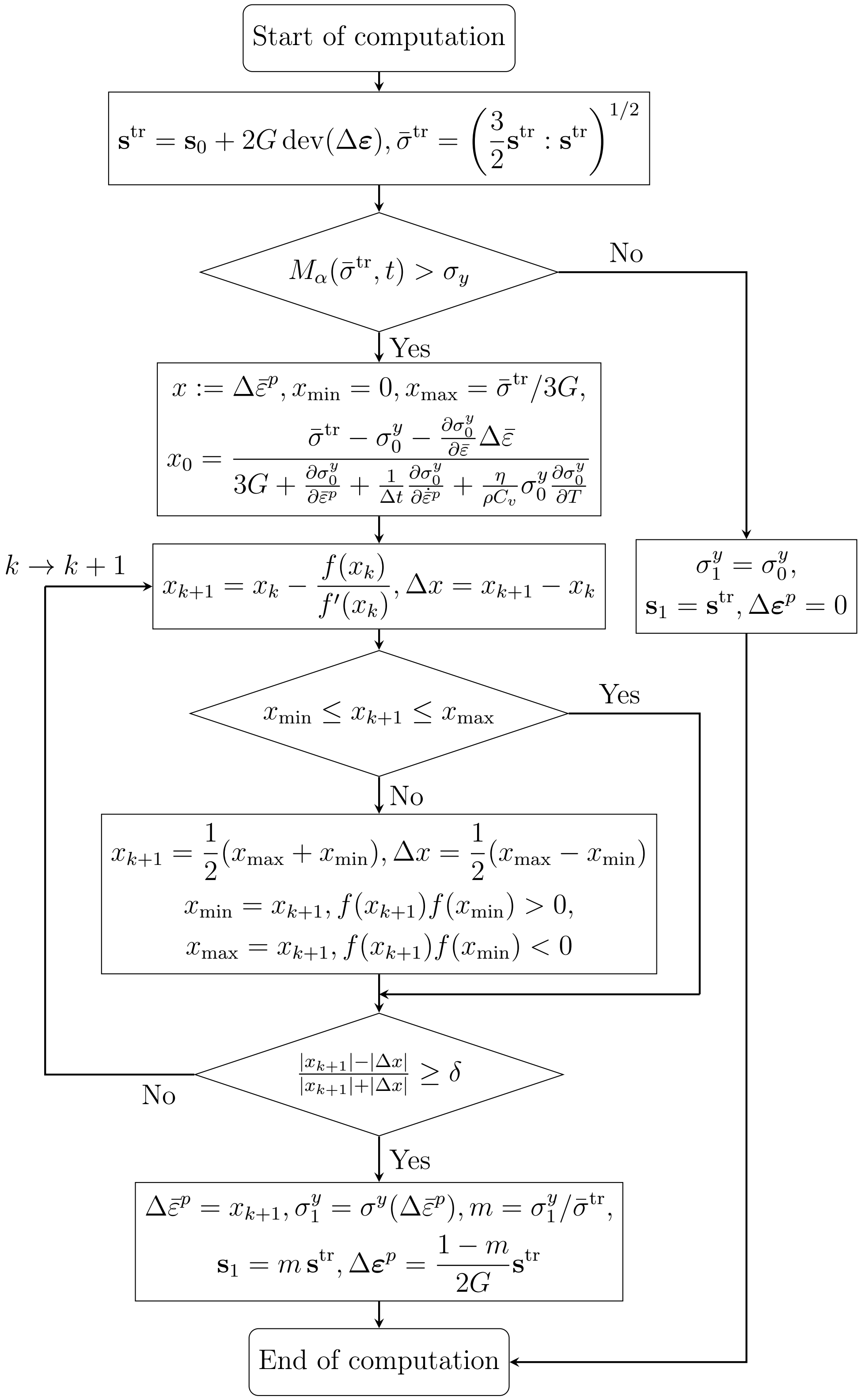

Figure 3.2: Calculation flowchart of the safe version of NR method for dynamic plasticity problem with the simplified version of RP model 3.53

Chapter 4

Simulation results from different models and comparative analysis

In this chapter, behaviors of the original and modified RP models are firstly compared based on aluminium alloys 6082-T6 and 2519A and titanium alloy Ti-6Al-4V without considering the thermal softening phenomenon. Then, the thermo-mechanical responses of HSLA-65 steel, the commercial 93W–4.9Ni–2.1Fe Tungsten-based composite and Ti-6Al-4V over a wide range of strain rates and temperatures are simulated by IRP model, different phenomenological, dislocation-mechanism-based and artificial neural network models discussed in chapter 1. Main differences between different types of models are examined. Moreover, we compare the temperature-time correspondences within our simulations. Finally, to validate the calculation scheme developed in chapter 3 and illustrated in figure 3.2, we perform finite element analysis using a simplified version of the RP model. This analysis serves as an essential step towards confirming the accuracy and reliability of our computational approach.

Most of results presented in the chapter are published in papers [72] [84].

4.1 Comparison of results: IRP and ORP models

The validation of the model performance in describing the strain rate effects is given in this section. The elasto-plastic response of aluminium alloys 6082-T6, 2519A and titanium alloy Ti-6Al-4V in a wide range of strain rates are simulated by the IRP model, the ORP model and the JC model. It is important to note that this section does not specifically address the thermal softening behavior, but only focuses on the strain rate effects. Therefore, all simulations are performed within a true strain limit of 0.15. Additionally, we assume constant strain rates throughout the simulations. Theoretical results under uniaxial loading conditions are obtained and compared with experimental data to assess the accuracy of our models.

4.1.1 Aluminium alloys 6082-T6 and 2519A

Mocko W., Rodriguez-Martinez J. A. et al. conducted a group of experiments to study the compressive plastic response of 6082-T6 aluminium alloy (AA6082-T6) in a wide range of strain rates at room temperature [101]. The low-rate compression experiments ($10^{-4}\ \mathrm{s}^{-1} < \dot{\varepsilon} < 10^{-1}\ \mathrm{s}^{-1}$) were conducted by a servo-hydraulic testing machine, the intermediate- and high-rate compression experiments ($950\ \mathrm{s}^{-1} < \dot{\varepsilon} < 4500\ \mathrm{s}^{-1}$) were performed by a conventional split pressure Hopkinson bars (SPHB) arrangement and very-high-rate compression experiments ($2 \times 10^4\ \mathrm{s}^{-1} < \dot{\varepsilon} < 4 \times 10^4\ \mathrm{s}^{-1}$) were carried out using a miniaturised direct impact compression tests (MDICT) configuration. In addition, some of Winzer's experimental results [102] on the dynamic compressive behaviour of AA6082-T6 were mentioned in Mocko's research. One of the main characteristics of SPHB experiments, compared with other high-rate test techniques, is that a high strain rate deformation is imposed while the tested material is approximately in a dynamic equilibrium. Thus, the SPHB experiments are convenient for studying the rate-dependent constitutive behaviour of tested materials without considering the wave propagation. The mechanism of material response at very-high-rate loading could be different, so the very-high-rate compression experiments are not interested in the current paper.

Experimental results obtained under uniaxial compression with a wide strain-rate range and the performance of the IRP, JC and ORP models are illustrated in figures 4.1 (a), (b) and (c). The determined parameter values are shown in tables 4.1, 4.2 and 4.3. The Young's modulus at temperature $T = 0$ K and its temperature dependence are given in the work [101], where the Young's modulus at room temperature can be derived. According to the experimental results, the strain-rate effect is pronounced, i.e. the flow stress level is elevated with the increasing strain rate. The IRP model and JC model are compared firstly. It is evident in figures 4.1 (a) and 4.1 (b) that both models can well depict the strain-rate effect due to their strain-rate dependent multipliers, $\Sigma(t)/\widetilde{\Sigma}(t)$ and $1+C\ln\left(\frac{\dot{\varepsilon}}{\dot{\varepsilon}_0}\right)$, respectively. In the quasi-static case ($\dot{\varepsilon} = 0.01\ \mathrm{s}^{-1}$), the experimental data and simulated curves of both IRP and JC models nearly overlap. However, in dynamic cases ($950\ \mathrm{s}^{-1} < \dot{\varepsilon} < 4500\ \mathrm{s}^{-1}$), the IRP model outperforms the JC model.

Three key points are noteworthy. First, there are three flow stress levels observed in experiments, corresponding to the low- ($\dot{\varepsilon} = 0.01\ \mathrm{s}^{-1}$), intermediate- ($\dot{\varepsilon} = 950\ \mathrm{s}^{-1}$ and $1100\ \mathrm{s}^{-1}$) and high-rate compression conditions ($\dot{\varepsilon} = 3900\ \mathrm{s}^{-1}$ and $4500\ \mathrm{s}^{-1}$), respectively. At intermediate strain rates, the flow stress level obtained by the IRP model is closer to the experimental data than that acquired by the JC model. Besides, the stress-strain curves modelled by the JC model at intermediate strain rates distinctly overestimate the experimental results, and they are almost identical to those curves at high strain rates. In contrast, the curves acquired by the IRP model at intermediate and high strain rates are separated, and only the curve at strain rate 1100 s^{-1} locates slightly above the experimental one. Moreover, the IRP model simulates three stress levels, which are in good agreement with experimental facts. Nevertheless, the JC model acquires only two stress levels (the quasi-static and dynamic ones). Second, in the high-rate compression test, an obvious yield drop effect is found. As the plastic deformation commences, the dynamic stress-strain curves ascend slightly at first and then descends to be lower than the yield stress ultimately. As presented in figure 4.1 (b), the flow stress levels simulated by the JC model at high loading rates are consistent with the experimental results when the true strain exceeds 4%. Notwithstanding, in the strain range approaching the yield point, the JC model may fail to work. At an approximately constant strain rate, both ORP and IRP models can describe and predict the non-monotonic material behaviour. At last, in a numerical simulation (for instance, the finite element analysis), in addition to the rate-dependent hardening law, the plastic criterion is equally crucial in the yield function. The yield stress vs. strain rate curves simulated by IRP (or ORP) and JC models are shown in figure 4.1 (d). The value $C = 0.01$ is determined by fitting stress values at different strain rates. In this way, the rate-dependent flow stress levels are acceptably described, as given in figure 4.1 (b). However, the rate dependence of the yield stress ($\varepsilon_p = 0$) can not be well characterised. It can be seen in figure 4.1 (d) that the IRP model provides a better description of rate-dependent yield stresses than Johnson-Cook's plastic criterion does. In the current case, the Johnson-Cook's criterion $\sigma \leq A\left(1 + C\ln\left(\frac{\dot{\varepsilon}}{\dot{\varepsilon}_0}\right)\right)$ is not suitable for the yield stress prediction since the plastic deformation simulated by the JC model takes place ear-

Table 4.1: Determined parameter values of different materials in the IRP model.

Materials	Elasticity	Plasticity					
	E (GPa)	σ_y (MPa)	K (MPa)	n	τ (μs)	α	m
AA 6082T6	30 [101]	306.52	116.48	0.408	2.10	3	5.5
Ti-6Al-4V	114 [82]	773.99	322.75	0.370	459	22	12
Al 2519A	78 [103]	424.30	241.00	0.433	0.65	5	4

Table 4.2: Determined parameter values of different materials in the Johnson-Cook model.

Materials	A (MPa)	B (MPa)	n	C	$\dot{\varepsilon}_0$ (s^{-1})
AA 6082T6	306.52	116.48	0.408	0.01	0.01
Ti-6Al-4V	773.99	322.75	0.370	0.016	0.001
Al 2519A	424.30	241.00	0.433	0.008	0.001

lier than that in experiments. As a consequence, the JC model may provide a less accurate result in a simulation of a complex dynamic system. It might be believed that the Johnson-Cook's plastic criterion is still available if the value of parameter C is well adjusted to fit the rate-dependent yield stresses. The adjustment is summarised in figure 4.1 (d), where $C = 0.0176$. As a consequence of adopting the JC model, the simulated flow stress levels overestimate the experimental ones, shown in figure 4.1 (e). Thus, if the JC model is implemented, a compromise should be made between describing the flow stress level and the yield stress.

The flow stress levels predicted by the ORP model align well with experimental results when subjected to intermediate- and high-rate loading conditions. However, when exposed to a low strain rate, the model overestimates the flow stress compared to the experimental data. This discrepancy highlights a limitation of the ORP model in accurately capturing the hardening behavior across different strain rates. Specifically, this deficiency arises from the absence of a functional relationship between the relaxation function $\gamma(t)$ and the plastic strain $\varepsilon_p(t)$ within the model as discussed in section 2.1.3.

Table 4.3: Determined parameter values of different materials in the ORP model.

Materials	Elasticity	Plasticity			
	E (GPa)	σ_y (MPa)	τ (μs)	α	β
AA 6082T6	30 [101]	306.52	2.10	3	0.09
Ti-6Al-4V	114 [82]	773.99	459	22	0.45
Al 2519A	78 [103]	424.3	0.65	5	0.09

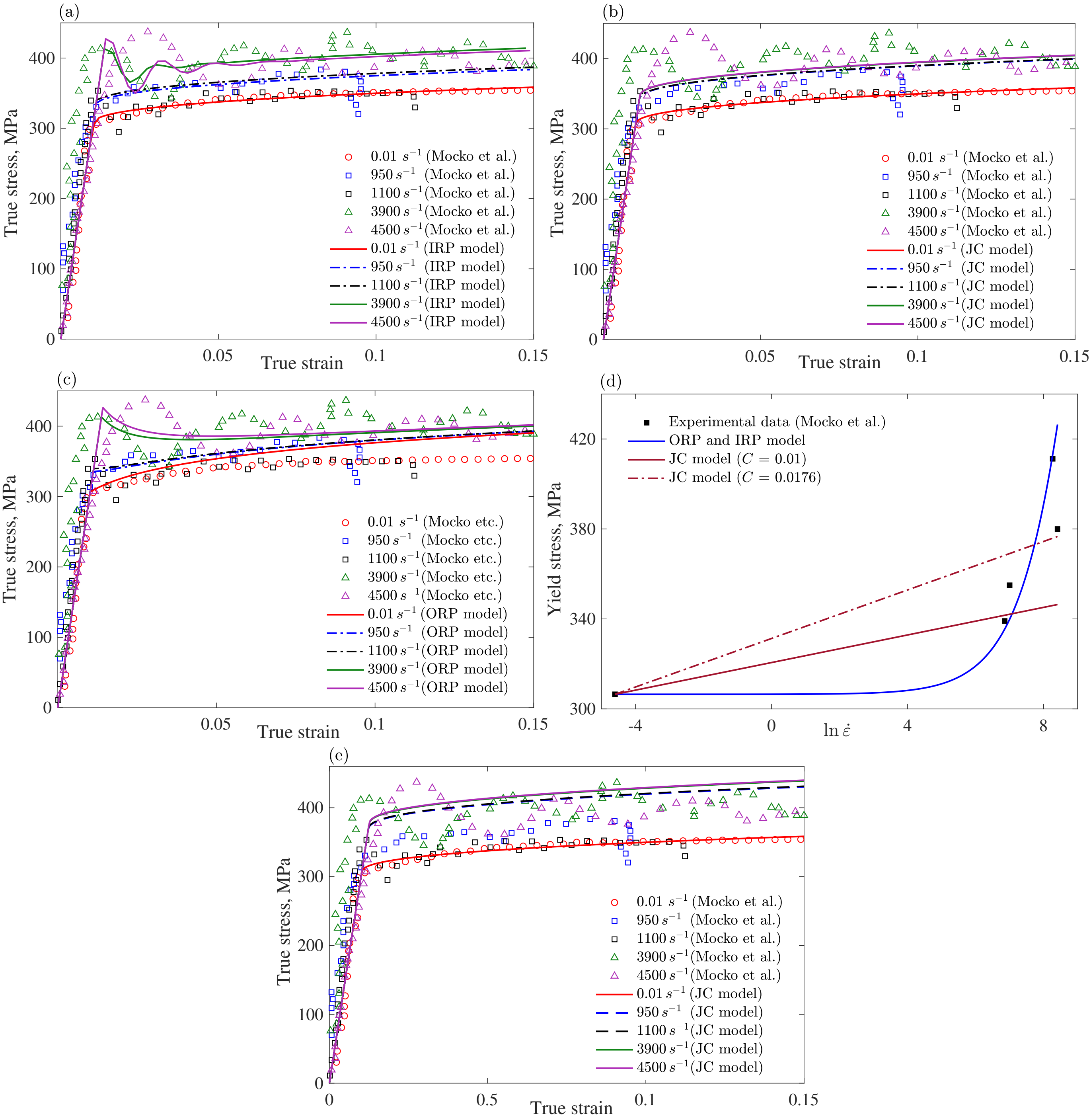

Figure 4.1: Comparison between stress-strain curves of the AA 6082T6 measured in compression tests [101] and those simulated at room temperature and various strain rates by (a) IRP model (b) JC model with $C = 0.01$, (c) ORP model and (e) JC model with $C = 0.0176$. (d) The strain rate dependence of the yield stress acquired by experiments, the ORP or IRP model and the JC model. The symbols represent experimental data, and lines are model description.

The stress-strain relations of the 2519A aluminium alloy (Al 2519A) at room temperature and various strain rates are investigated experimentally in the work [89]. The compression tests and simulated results are given in figures 4.2 (a), (b) and (c). The determined parameter values are shown in tables 4.1, 4.2 and 4.3. The Young's modulus is provided in the work [103]. The IRP and ORP models show the separating flow stress levels at high loading rates, while the flow curves simulated by the JC model are nearly overlapping. Figure 4.2 (d) illustrates that the yield stress vs. strain rate relation is better described by the ORP and IRP models.

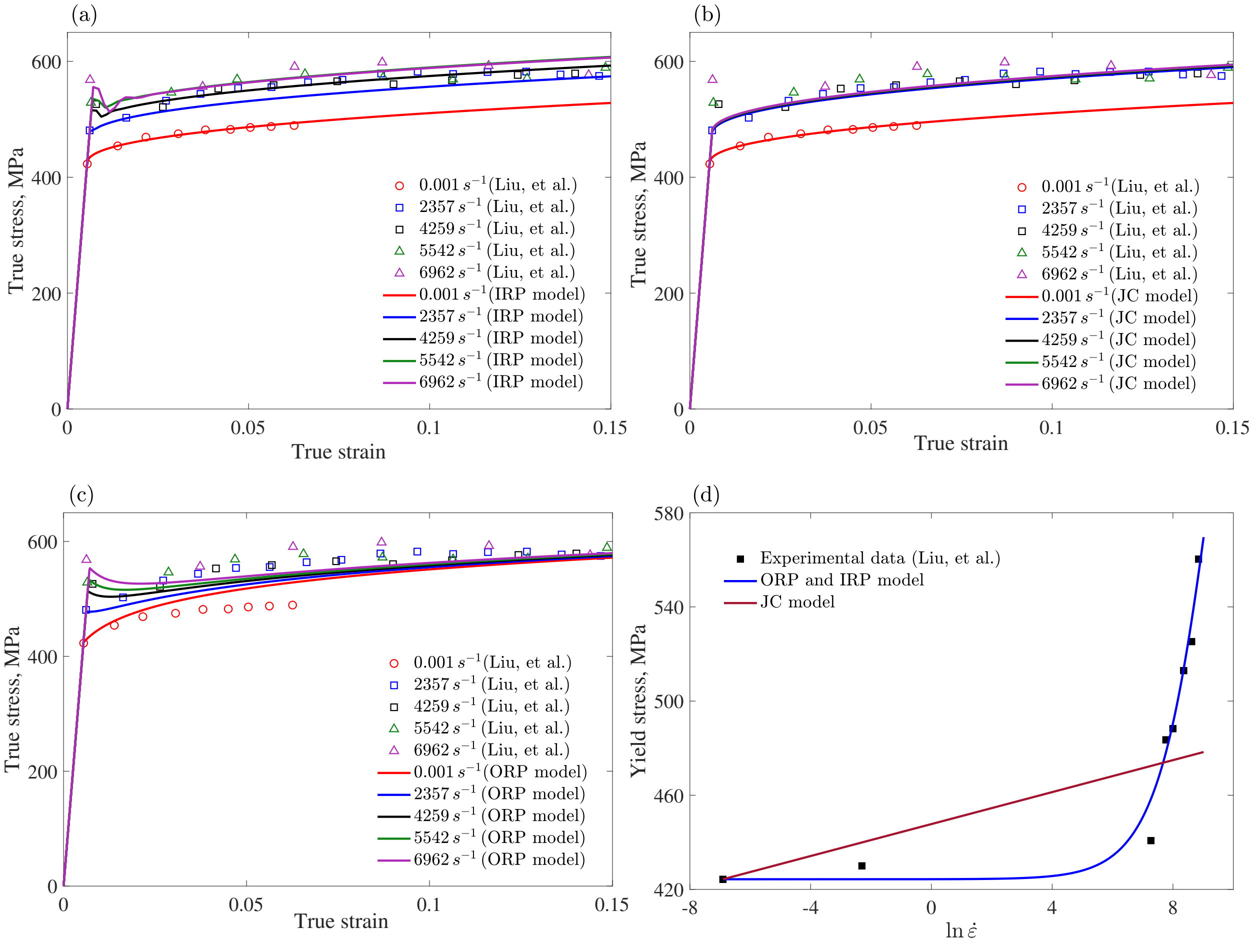

Figure 4.2: Comparison between stress-strain curves of the Al 2519A measured in compression tests [89] and those simulated by (a) IRP model (b) JC model and (c) ORP model at room temperature and various strain rates. (d) The strain rate dependence of the yield stress acquired by experiments, the ORP or IRP model and the JC model. The symbols represent experimental data, and lines are model description.

4.1.2 Titanium alloy Ti-6Al-4V

In the research [73], a series of tension experiments were carried out by Hu et al. to investigate both quasi-static and dynamic plastic response of a commercial Ti-6Al-4V Titanium alloy under various loading conditions and temperatures. The MTS testing machine and the split Hopkinson pressure bar (SHPB) technique are used to achieve a wide range of strain rates (MTS machine for quasi-static tests, SHPB for dynamic tests). A sequence of effects, including strain-rate effect, work-hardening effect, stress state effect and temperature influence, were discussed in detail. Here, the stress state effect and temperature influence are temporarily out of consideration.

The tensile experimental results and the model description are illustrated in figures 4.3 (a), (b) and (c). The parameter values are shown in tables 4.1, 4.2 and 4.3. The Young's modulus is provided in the work [82]. Under impact loads, the yield drop is observed in experiments, the tendency of which can be described by the IRP model. All three models give satisfactory flow stress levels at high strain rates. However, it is noticeable in experiments that at high strain rates the work hardening response is not obvious. Under dynamic loading conditions, the flow stress curves generally go steadily with the increase of deformation, although a visible strain hardening response is observed under the quasi-static loading condition. The JC model doesn't make a distinction between strain hardening responses at different strain rates, while the ORP model and the IRP model provide a better characterisation of the stable work-hardening response of the material under dynamic conditions. At the low strain rate $\dot{\varepsilon} = 1\ \mathrm{s}^{-1}$, the JC model performs better than other models.

To sum up, the JC model gives acceptable flow stress levels at different strain rates at the expense of the accuracy of the predicted yield stress in the case of yield drop. Besides, the JC model cannot simulate the non-monotonic behaviour of stress-strain curves. The ORP model, on the contrary, can more precisely predict the yield stress and describe the yield drop effect, but it is slightly inferior to the JC model in the work-hardening simulation at low strain rates. The IRP model demonstrates better performance.

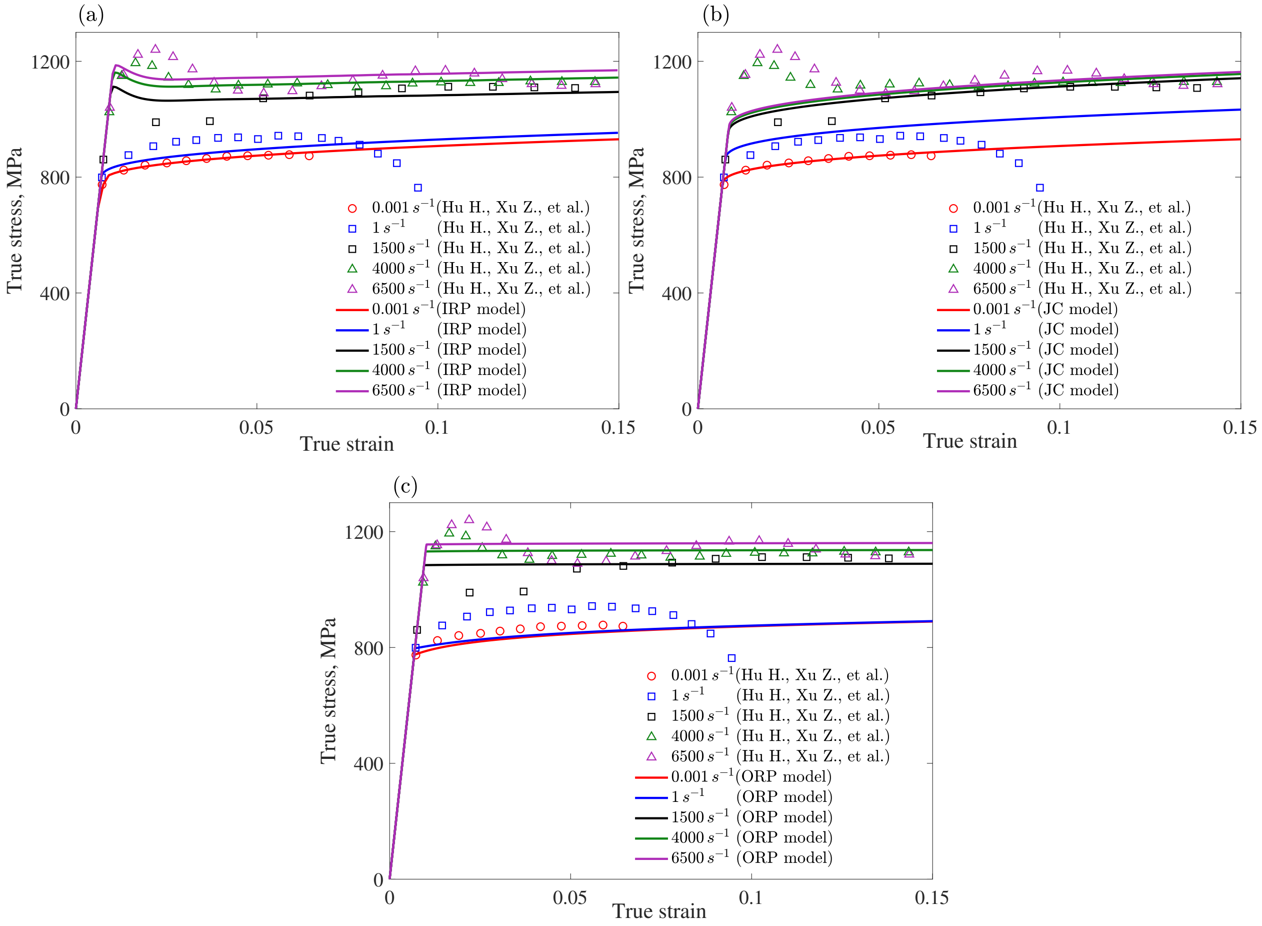

Figure 4.3: Comparison between stress-strain curves of the Ti-6Al-4V measured in tensile tests [73] and those simulated by (a) IRP model (b) JC model and (c) ORP model at room temperature and various strain rates. (d) The strain rate dependence of yield stress. The symbols represent experimental data, and lines are model description.

4.2 Comparison of results: IRP and other existing models

In this section, the thermo-mechanical responses of HSLA-65 steel, the commercial 93W–4.9Ni–2.1Fe Tungsten-based composite and Ti-6Al-4V over a wide range of strain rates and temperatures are simulated by the IRP model considering different temperature-time correspondences. The descriptive abilities of various models mentioned in chapter 1 are compared. All simulations are performed assuming a constant strain rate. The initial values of the model constants are determined through physical definitions or experimental data fitting. These values are then optimized using a constrained optimization procedure to minimize the errors between model descriptions and experimental results. The ability of the studied models to accurately describe the experimental data was quantitatively assessed using the following error measure

$$\Delta = \frac{1}{N}\sum_{i=1}^{N}\left|\frac{\sigma_i^{\exp} - \sigma_i^{\mathrm{mod}}}{\sigma_i^{\exp}}\right| \times 100\%, \tag{4.1}$$

where N is the total number of experimental data, $\sigma_i^{\exp}$ is the experimental measured true stress and σ_i^{mod} is the true stress described by models. The results are deemed to be relatively accurate when the descriptive error Δ is less than 5%, which is commonly accepted in engineering practice.

To investigate the negative hardening at low temperatures and high strain rates, experimental data on HSLA-65 steel are considered. In the section 4.2.5, we specifically examine the main differences between the artificial neural network (ANN) model and constitutive models using experimental data from the tungsten-based composite. Additionally, the temperature-time correspondence that provides better results for the HSLA-65 steel and tungsten-based composite is validated through experimental data for Ti-6Al-4V.

4.2.1 Taylor–Quinney coefficient

Plastic deformation produces heat that can either be dissipated to the surroundings or retained within the material, thereby raising its temperature. If the rate of heat generation surpasses the rate of heat dissipation, the temperature of the material increases. At high strain rates, the adiabatic process occurs where most of the heat generated by rapid plastic deformation is retained within the material. The rapid and continuous temperature rise during plastic deformation leads to a simultaneous decrease in the flow stress of the material. The temperature rise is generally determined by the equation (1.3), which derives the equation (4.2) in the one-dimensional case.

$$\Delta T = \frac{\eta}{\rho C_{\nu}}\int_{\varepsilon_p}^{\varepsilon_p+\Delta\varepsilon_p} \sigma \mathrm{d}\varepsilon_p \tag{4.2}$$

4.2.2 HSLA-65 steel

As mentioned in the section 2.2.3, Nemat-Nasser, and Guo conducted a comprehensive study [14] on the thermo-mechanical behavior of HSLA-65 steel with a BCC structure. The compression tests were carried out over a wide range of strain rates from $0.001\,s^{-1}$ to $8500\,s^{-1}$ and temperatures ranging from 77 to 1000 K. For quasi-static loading rates of $0.001\,s^{-1}$ and $0.1\,s^{-1}$, experiments were performed using an Instron hydraulic testing machine at temperatures of 77 to 800 K. The high loading rates tests were conducted using the enhanced compression recovery Hopkinson technique, over the temperature range of 77 to 1000 K. Elevated temperatures were achieved using a high-intensity quartz lamp in a radiant-heating furnace of an argon environment. The low temperature of 77 K was achieved by immersing the specimen and the testing fixture (AL_2O_3 ceramic bars) in a bath of liquid nitrogen. At temperatures above 700 K, the flow stress increased significantly with increasing temperature due to dynamic strain aging. This abnormal phenomenon is not considered in the current paper. Therefore, the modeling is only conducted within the temperature range of 77–700 K. Young's modulus of HSLA-65 steel at different temperatures was given in the work [104]. Over the temperature range of 296–700 K, the temperature dependence of Young's modulus can be described by the relation (4.3) mentioned in the work [38]. E_0 is Young's modulus at $T = 0$ K, T_m is the melting temperature, and θ^* is the characteristic homologous temperature. The model description and the experimentally measured elastic modulus are displayed in figure 4.4 (a), and used parameter values are shown in table 4.4. The adiabatic temperature rise was a concern by Nemat-Nasser and Guo [14]. The value of the mass density ρ of HSLA-65 steel and the Taylor–Quinney coefficient η are shown in table 4.4. The heat capacity C_ν is taken 0.5 J/gK.

$$E(T) = E_0 \left\{ 1 - \frac{T}{T_m} \exp\left[\theta^* \left(1 - \frac{T_m}{T} \right) \right] \right\} \tag{4.3}$$

The experimental stress-strain diagrams of HSLA-65 steel at quasi-static strain rates can be well described by the relation (2.30). Thus, in this case, the relation (2.30) is incorporated into the IRP model (2.28). By fitting the corresponding experimental stress-strain diagrams given in the work [14], the value ranges for τ and α at different temperatures, which provides a less than 5 % relative error in describing the dynamic stress-strain diagrams, can be established. These ranges are denoted by green vertical lines in figures 4.4 (b) and (c). Figure 4.4 (b) shows the temperature dependence of the incubation time τ with a fixed value $\alpha = 15$, while figure 4.4 (c) illustrates the temperature dependence of the parameter α with a

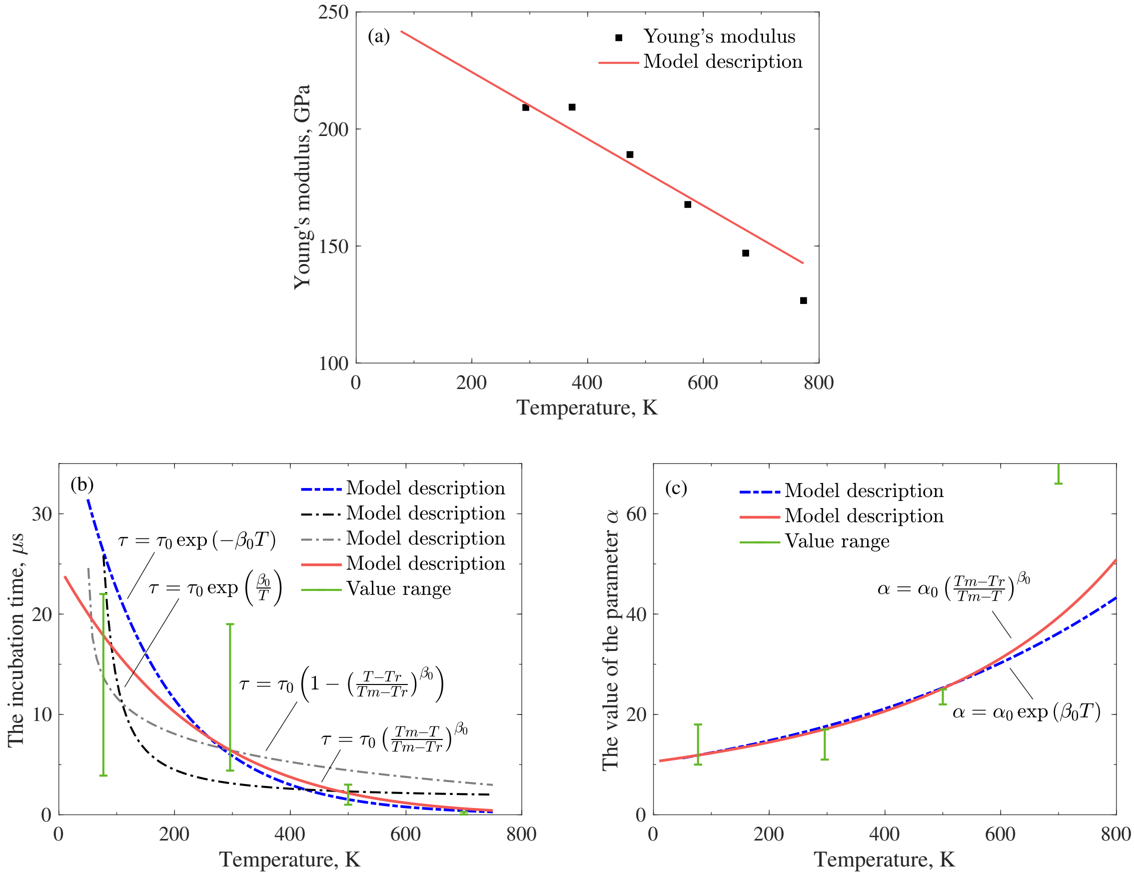

Figure 4.4: The temperature dependence of the Young's modulus (a), the incubation time τ with fixed $\alpha = 15$ (b) and the parameter α with fixed $\tau = 6.44\,\mu s$ (c) for HSLA-65 steel. The symbols are the experimentally measured Young's modulus (a). The value ranges for τ (b) and α (c) obtained by fitting the IRP model to the experimental data are denoted by green vertical lines. The solid and dash-dotted lines in (b) and (c) are corresponding model descriptions.

fixed value $\tau = 6.44\,\mu$s. The relations (2.34) and (2.37) more accurately describe the temperature dependence of parameters τ and α compared to others. Although the relation (2.37) can not perfectly fall within the value range for α at the temperature of 700 K, it still provides a satisfactory stress-strain diagrams shown below in figure 4.5 (b). Additionally, this paper does not focus on the temperature dependence of the parameter α.

Figures 4.5 and 4.6 illustrate the stress-strain diagrams obtained from experiments and simulations using different phenomenological and dislocation-mechanics-based models. Figure 4.5 presents simulation results at temperatures of 77, 296, 500, and 700 K and high loading rates of 3000 and 8500 s^{-1}. Figures 4.5 (a) and (b) show the performance of the IRP model incorporating the relation (2.34) and (2.37),

Table 4.4: Parameters determining the Young's modulus, the mass density, the plastic work-heat conversion factor and the melting temperature of tested materials.

Materials	E_0 (GPa)	T_m (K)	θ^*	ρ (g/cc)	η
HSLA-65 Steel [38][14]	252.80	1773	0	7.8	1
Tungsten [16]	370	1730	0.5	17.8	0.9
Ti-6Al-4V [105] [74]	109	1941	0.29	4.428	0.9

respectively. The parameter values used in the IRP model are provided in table 4.5 and table 4.6 or 4.7. Parameter values of the JC model, KHL model [1], NNI model and ZA model are given in tables 4.8, 4.9, 4.10 and 4.11, respectively. Figure 4.6 demonstrates the quasi-static response of the HSLA-65 steel under different loading conditions and their corresponding modelling. The description error (4.1) of different models is graphically presented in figure 4.7.

At the temperature of $77\,K$ and high-rate loadings, the negative hardening due to thermal softening induced by the rapid plastic dissipation are observed. The dislocation-mechanics-based models show good agreement with experimental data at different strain rates, whereas the negative hardening is only partially featured. The JC and KHL models satisfactorily describe some curves at high loading rates, but at the expense of their performance at low loading rates. The experimental data are more accurately described by the IRP model, NNI model, and ZA model. Specifically, the IRP model captures the negative hardening tendency due to the equation (1.3) and the temperature-time correspondence following the temperature-dependent behavior of the RS factor. It appears that the temperature-dependent relations (2.34) and (2.37) can give similar results. The parameter values of the NNI model are given in the work [14]. The initial parameter values of other models are determined through experimental data fitting, and then these values are optimized using a constrained optimization procedure to minimize the errors between descriptive and experimental results.

4.2.3 93W–4.9Ni–2.1Fe Tungsten-based composite

Xu and Huang conducted a series of compression tests on the commercial 93W–4.9Ni–2.1Fe Tungsten-based composite [16] with a BCC structure over a wide range

---

[1] Since there is a lack of data at the strain rate of 1 s^{-1}, the parameters of the KHL model for HSLA65 steel are determined by considering all available curves and minimizing the relative error. This approach may not yield optimal performance for the KHL model. It would be preferable to have experimental diagrams at a strain rate of 1 s^{-1} to enhance the accuracy and reliability of the parameter estimation.

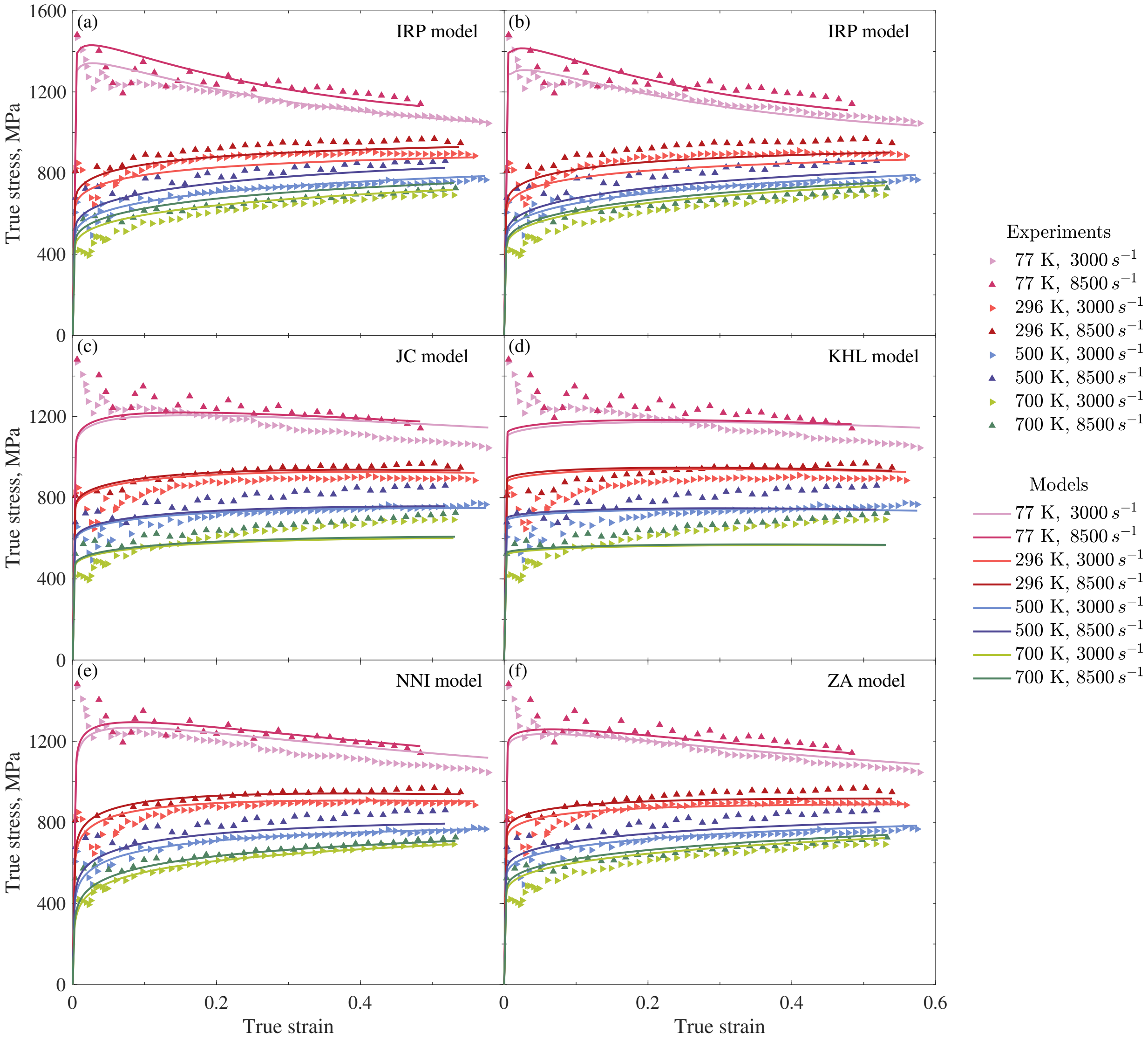

Figure 4.5: The stress-strain diagrams of the HSLA-65 steel at 4 temperatures and 2 high loading rates and the corresponding simulation performed by the IRP model with the temperature-dependent τ (a), the IRP model with the temperature-dependent α (b), JC model (c), KHL model (d), NNI model for BCC metals (e) and the ZA model for BCC metals (f).

Table 4.5: Parameters determining the flow stress at quasi-static loading rate following the relation (2.29) or (2.30).

Materials	σ_0 (MPa)	B_0 (MPa)	n_0	B_1 (MPa)	β_1 (K^{-1})	n_1	T_r (K)
HSLA-65 Steel	361.74	386.12	0.35	1049.81	8e-3	–	–
Tungsten	248.06	1023.17	0.42	2062.87	5.40e-3	–	–
Ti-6Al-4V	759.84	211.08	0.28	–	–	0.72	296

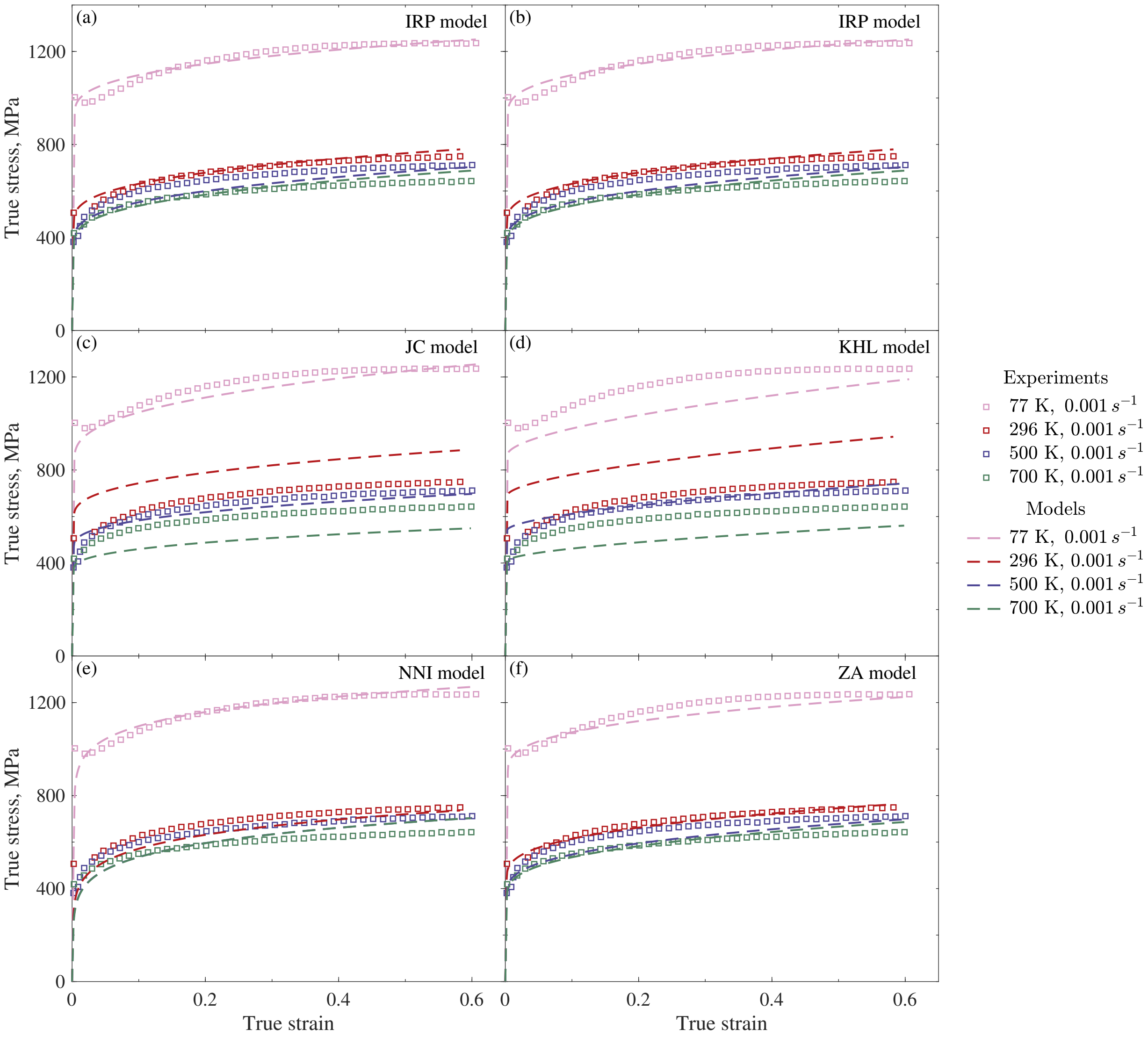

Figure 4.6: The stress-strain diagrams of the HSLA-65 steel at 4 temperatures and the quasi-static loading rate and the corresponding simulation performed by the IRP model with the temperature-dependent τ (a), the IRP model with the temperature-dependent α (b), JC model (c), KHL model (d), NNI model for BCC metals (e) and the ZA model for BCC metals (f).

Table 4.6: Parameters used in the IRP model with the temperature-dependent τ following the relation (2.34).

Materials	τ_0 (μs)	β_0	α	m	Tr (K)
HSLA-65 Steel	6.44	7.38	15	1	296
Tungsten	118	2.08	10	1	173
Ti-6Al-4V	1300	2.35	25	5	296

Table 4.7: Parameters used in the IRP model with the temperature-dependent α following the relation (2.37).

Materials	τ (μs)	α_0	β_0	m	Tr (K)
HSLA-65 Steel	6.44	17.05	2.62	1	296
Tungsten	110	9.98	0.94	1	173
Ti-6Al-4V	1300	24.97	0.70	5	296

Table 4.8: Determined parameters of different materials in the Johnson-Cook model.

Materials	A (MPa)	B (MPa)	n	C	$\dot{\varepsilon}_0$ (s^{-1})	m	T_r (K)
HSLA-65 Steel	969.30	570.98	0.382	0.015	1e-3	0.494	50
Tungsten [16]	1011.10	1601.50	0.4982	0.0305	1	0.7263	173
Ti-6Al-4V	759.84	211.08	0.28	0.02	0.001	0.72	296

Table 4.9: Determined parameters of different materials in the KHL model.

Materials	A (MPa)	B (MPa)	n_0	n_1	D_0 (s^{-1})	$\dot{\varepsilon}_0$ (s^{-1})	C	m	T_r (K)
HSLA-65 Steel	772.93	337.38	0.584	0.333	1e6	1	0.016	1.64	296
Tungsten [16]	264.6	1533.7	0.2172	3.9588	1e6	1	0.2196	1.1444	288
Ti-6Al-4V	851.79	91.94	0.087	2.45	1e6	1	0.032	1.50	296

Table 4.10: Determined parameters of different materials in the NNI or NNL model.

Materials	a (MPa)	n	σ_0 (MPa)	a_0	n_0	k/G_0 (K^{-1})	$\dot{\varepsilon}_0$ (s^{-1})	q	p
HSLA-65 Steel [14]	760	0.15	1450	–	–	10.6e-5	4e8	2	2/3
Tungsten [16]	1154.4	0.2635	2061.4	–	–	3.89e-5	2e10	3/2	1/2
Ti-6Al-4V	685	0.05	1037.59	0	1	6.2e-5	1.32e10	2	1

Table 4.11: Determined parameters of different materials in the ZA model.

Materials	σ_a (MPa)	B (MPa)	β_0 (K^{-1})	β_1 (K^{-1})	B_0 (MPa)	n	α_0 (K^{-1})	α_1 (K^{-1})
HSLA-65 Steel	361.74	1049.81	6.39e-3	3.23e-4	386.12	0.35	–	–
Tungsten [16]	230.50	1864.60	4.01e-3	2.49e-4	1083.10	0.4355	–	–
Ti-6Al-4V	513.73	1167.99	3.49e-3	1.54e-4	2812.71	–	0.31	0

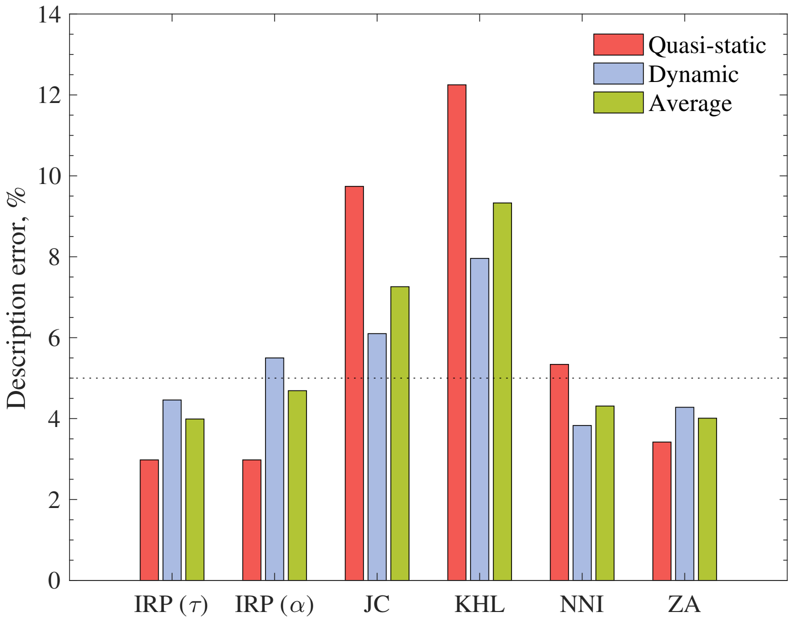

Figure 4.7: Comparison of different constitutive models in describing the stress-strain diagrams of HSLA-65 Steel.

of strain rates from $0.001\,s^{-1}$ to $3000\,s^{-1}$ and temperature from 173 to 873 K. The quasi-static compression tests, including strain rates $0.001\,s^{-1}$ and $1\,s^{-1}$, were performed using a MTS servo-hydraulic testing machine. Dynamic compression tests, at strain rates of $200\,s^{-1}$, $1000\,s^{-1}$, and $3000\,s^{-1}$, were conducted using the revised split Hopkinson pressure bar technique. These dynamic tests were performed at elevated temperatures of 288–873 K using electro-thermal cells. The temperature was measured by a thermocouple arrangement in the furnace for quasi-static tests, while during dynamic tests a thermocouple was directly attached to the specimen. Young's modulus of tested materials at different temperatures was given in Xu and Huang's work. The temperature dependence of Young's modulus was also described by the relation (4.3). The value of required parameters, as well as the mass density ρ of tested samples and its Taylor–Quinney coefficient η, are shown in table 4.4. The temperature-dependent heat capacity C_ν is assumed a function as $C_\nu = 162.92 - 0.00995T + 1.74 \times 10^{-5}\ \mathrm{T}^2\ \left(\times 10^{-3}\ \mathrm{J/gK},\ \text{for } 0°\mathrm{C} \leqslant T \leqslant 1000°\mathrm{C}\right)$ [16].

The value ranges for τ and α, which were obtained by fitting the experimental data to the IRP model, are displayed in figures 4.8. Equations (2.34) and (2.37) provide satisfactory descriptions of the temperature dependence of τ and α, respectively. Although the relation (2.32) also agrees with value ranges for τ, it gives a slightly

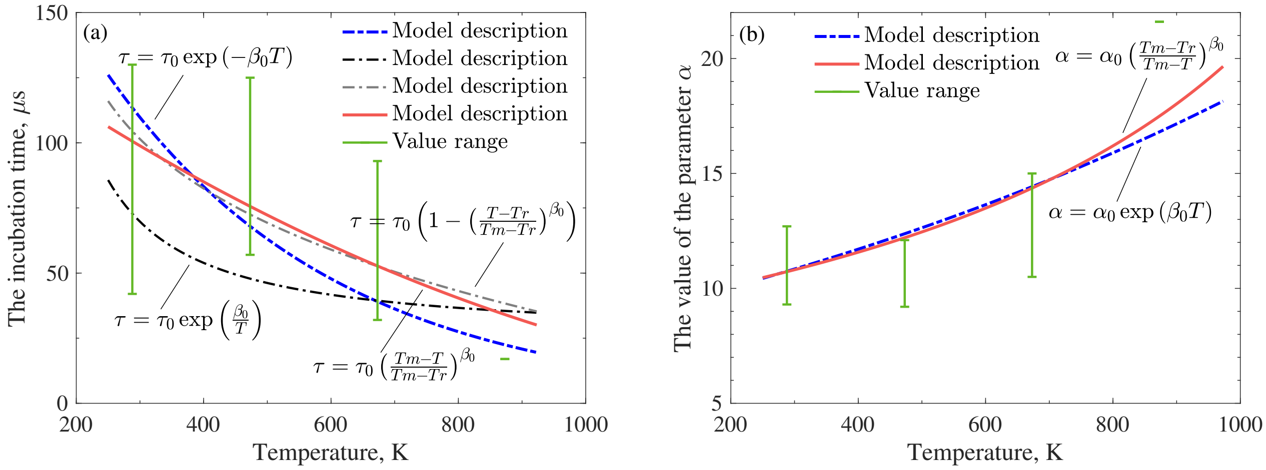

Figure 4.8: The temperature dependence of the incubation time τ with fixed $\alpha = 10$ (a) and the parameter α with fixed $\tau = 101\,\mu s$ (b) for the 93W–4.9Ni–2.1Fe Tungsten-based composite. The value ranges for τ and α obtained by fitting the IRP model to the experimental data are denoted by green vertical lines. The solid and dash-dotted lines are corresponding model descriptions.

higher error in describing the stress-strain diagrams compared to the relation (2.34). At the temperature of 873 K, the IRP model can only provides modelling with the description error approximately equal to 6–7 %. Thus, a single green point, instead of a value range, is illustrated. The parameter values are shown in tables 4.6 and 4.7. The stress-strain diagrams and model descriptions at various strain rates and temperatures are presented in figures 4.9 and 4.10, respectively. The stress-strain diagrams at quasi-static strain rates are well described by the relation (2.30) used in the IRP model. The parameter values are shown in table 4.5. The parameter values of the JC, KHL, NNI and ZA models are provided in the work [16]. The final parameter values used in the JC, KHL, NNI and ZA model are given in tables 4.8, 4.9, 4.10 and 4.11, respectively.

The experimental data are also described by the ANN model with 1 hidden layer and 512 neurons, i.e. structure 3–512–1 in figure 1.1. The total number of build-in parameters is 2561, and the model performance is illustrated in figures 4.11 (a), (b), and (c). The training dataset of the ANN model includes experimental data obtained at static strain rates of $0.001\,s^{-1}$ and $1\,s^{-1}$, as shown in 4.11 (a), and dynamic strain rates of $200\,s^{-1}$ and $3000\,s^{-1}$ given in 4.11 (b). The number of data points for training is 3600, since a sufficient number of points meeting our needs can always be obtained from stress-strain curves, and part of them are demonstrated in 4.11 (a) and (b). The model validation is performed using experimental data at a strain rate of $1000\,s^{-1}$, and the results is demonstrated in 4.11 (c). The experimental data are represented by symbols, and the solid lines indicate the model descriptions. The description errors of different models are reported in figure 4.12 (a), among which the more accurate description is provided by the IRP model, the ZA model, and the ANN model. Notice that the ANN model has the best descriptive ability, as a large number of parameters can always achieve relatively accurate data fitting. The description errors of different models on the validation dataset are illustrated in figure 4.12 (b), where the ANN model seems to lose its superiority. The description error of ANN model higher than many other models, shown in figure 4.12 (b), is explainable and discussed in detail in section 4.2.5, along with the main differences between the ANN model and constitutive models.

4.2.4 Ti-6Al-4V

As discussed in sections 4.2.2 and 4.2.3, the temperature dependences of τ in (2.34) and α in (2.37) provide better results for HSLA-65 steel and Tungsten-based composite. Hence, these relations are validated using experimental data of the widely used Ti-6Al-4V. Meanwhile, the function (2.29) is validated as well, although the relation (2.30) can also accurately describe the thermal softening at quasi-static loading rates.

In the study [82], Xu and Huang conducted a series of experiments to examine the quasi-static and dynamic plastic responses of the Ti-6Al-4V alloy, which has an HCP structure, under various thermo-mechanical loading conditions. To achieve a wide range of strain rates and temperatures, they employed the MTS testing machine for quasi-static tests and the split Hopkinson pressure bar (SHPB) technique equipped with a temperature control system for dynamic tests. The study discussed in detail the strain-rate effect, work-hardening effect, stress-state effect, and temperature influence. However, the stress state effect is not considered in the current paper. Here, we focus on the tension tests from the study [82], which revealed intriguing non-monotonic behavior. The work [105] provided Young's modulus values for the tested Ti-6Al-4V at different temperatures. The temperature dependence of Young's modulus can be accurately described using relation (4.3), as shown in figure 4.13 (a). Table 4.4 displays the required parameters, as well as the mass density (ρ) of the tested samples and its Taylor–Quinney coefficient (η) given by Khan [74]. Moreover, the work [74] used a temperature-dependent heat capacity ($C_{\mathrm{v}} =$

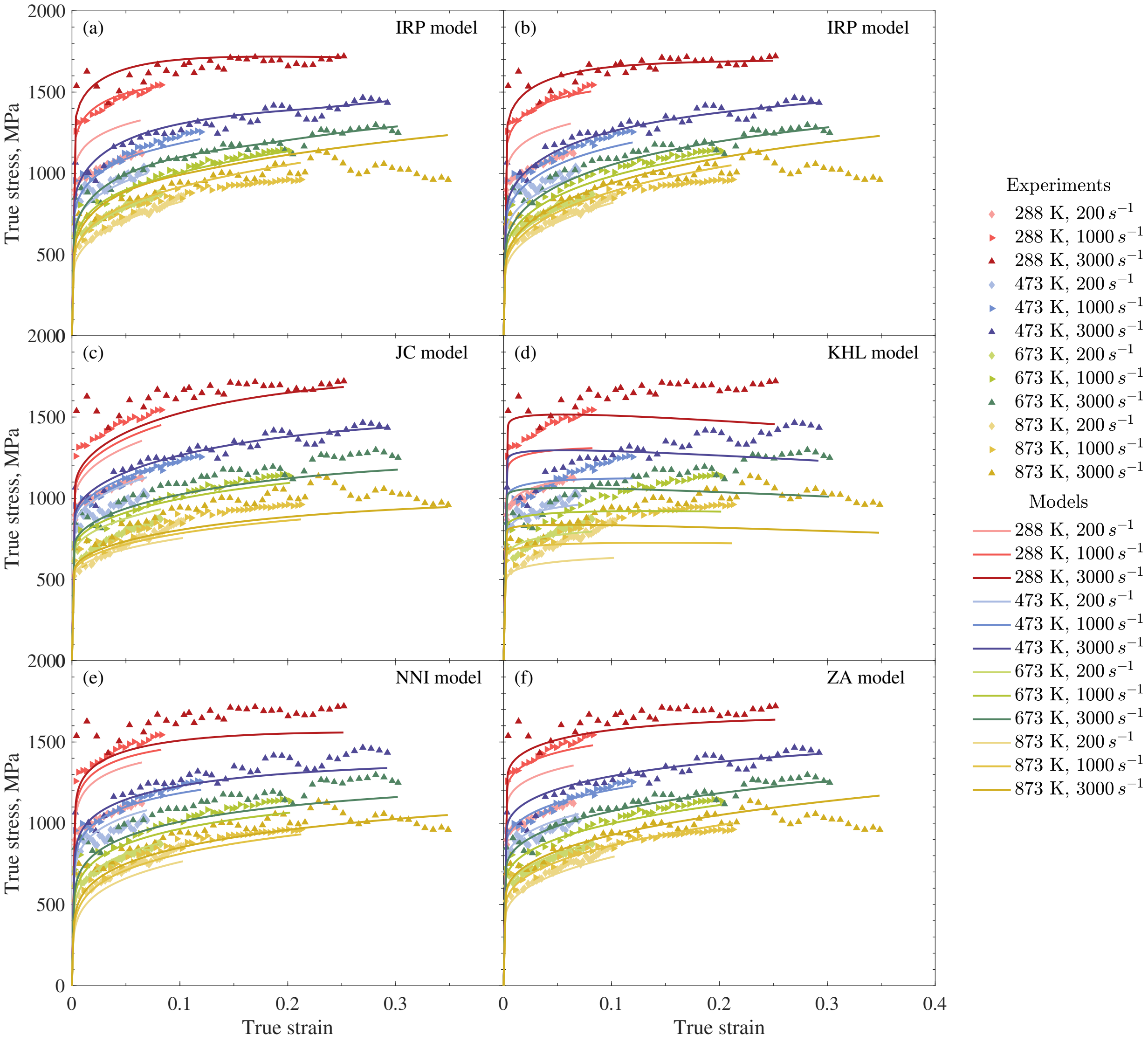

Figure 4.9: The stress-strain diagrams of the commercial 93W–4.9Ni–2.1Fe Tungsten-based composite at 4 temperatures and 3 high loading rates and the corresponding simulation performed by the IRP model with the temperature-dependent τ (a), the IRP model with the temperature-dependent α (b), JC model (c), KHL model (d), NNI model for BCC metals (e) and the ZA model for BCC metals (f).

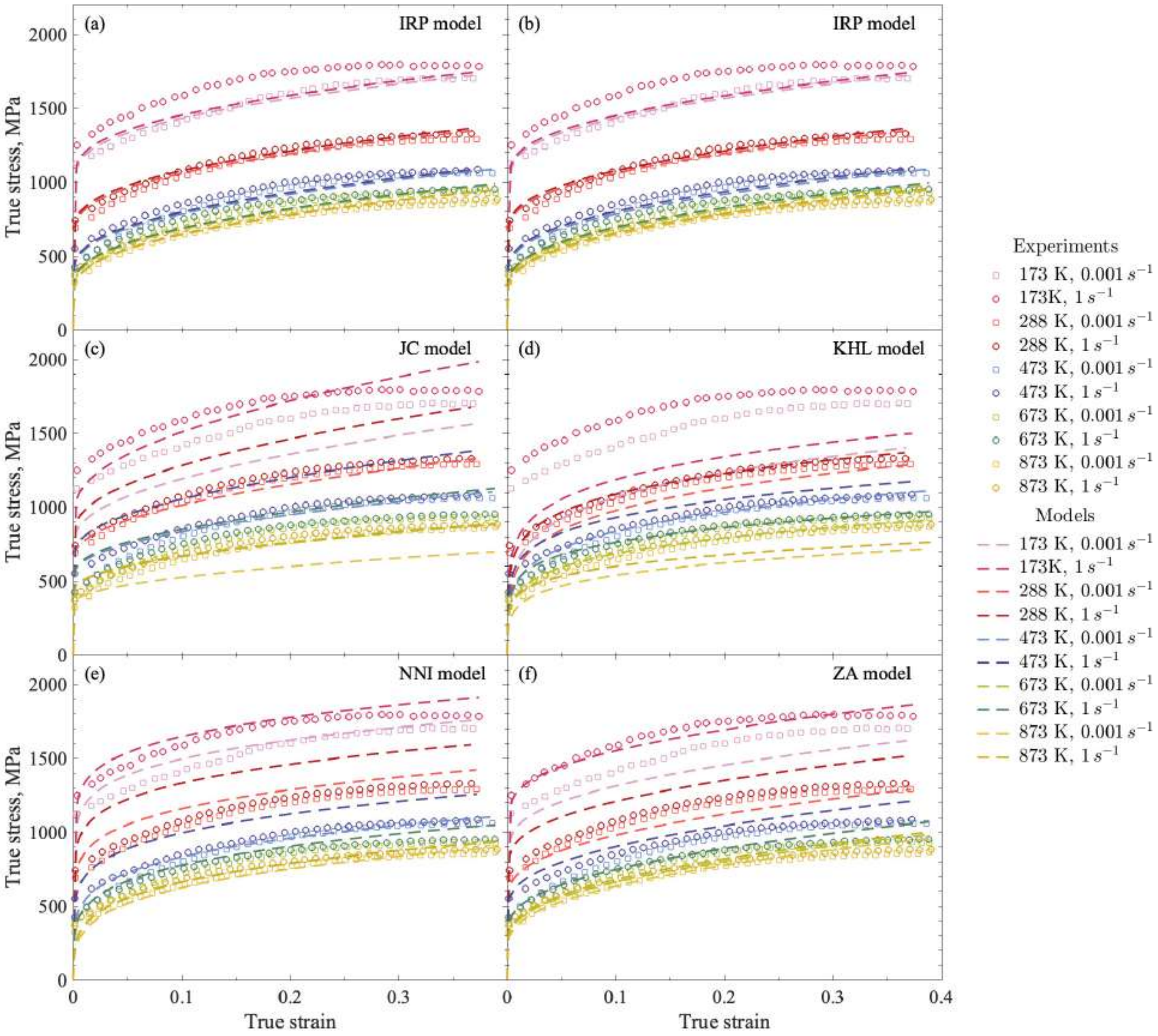

Figure 4.10: The stress-strain diagrams of the commercial 93W–4.9Ni–2.1Fe Tungsten-based composite at 5 temperatures and 2 quasi-static loading rates and the corresponding simulation performed by the IRP model with the temperature-dependent τ (a), the IRP model with the temperature-dependent α (b), JC model (c), KHL model (d), NNI model for BCC metals (e) and the ZA model for BCC metals (f).

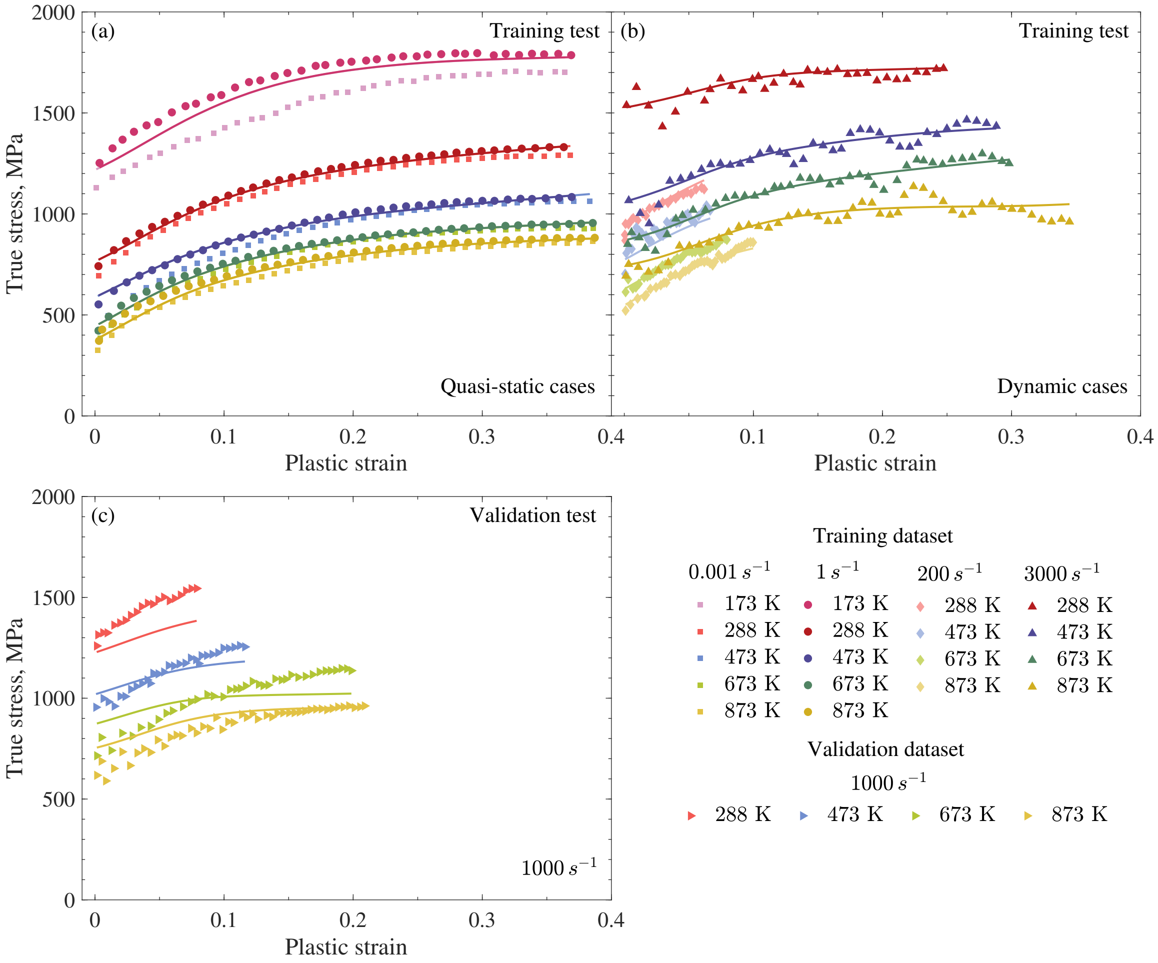

Figure 4.11: Performance of an Artificial Neural Network (ANN) model in describing stress-strain diagrams of the commercial 93W–4.9Ni–2.1Fe Tungsten-based composite at various temperatures and strain rates. The training dataset includes experimental data obtained at static strain rates of 0.001 s^{-1} and 1 s^{-1} (a) and dynamic strain rates of 200 s^{-1} and 3000 s^{-1} (b). The model validation is performed using experimental data at a strain rate of 1000 s^{-1} (c). The experimental data are represented by symbols, and the solid lines indicate the model descriptions.

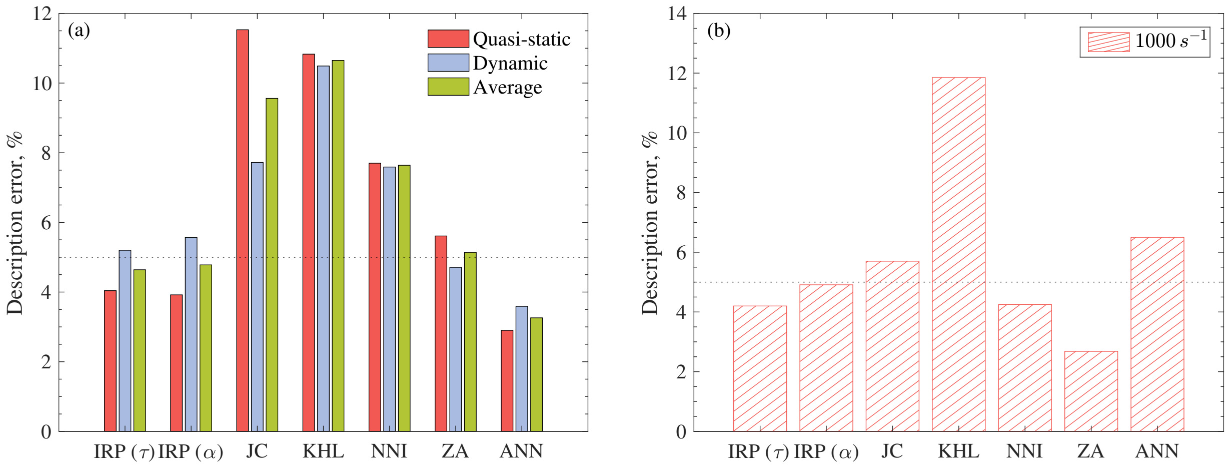

Figure 4.12: Comparison of description errors of different models in describing the stress-strain diagrams of the commercial 93W–4.9Ni–2.1Fe Tungsten-based composite. These include the overall comparison of errors at quasi-static and dynamic strain rates, as well as their average errors (a). Meanwhile, the error of the ANN model at its validation dataset ($1000\,s^{-1}$) and its comparison with other models are also focused (b).

$\left(559.77 - 0.1473T + 0.00042949T^2\right) \times 10^{-3}$ J/(gK) $\quad$ (278 K $< T <$ 1144 K)) in the analysis.

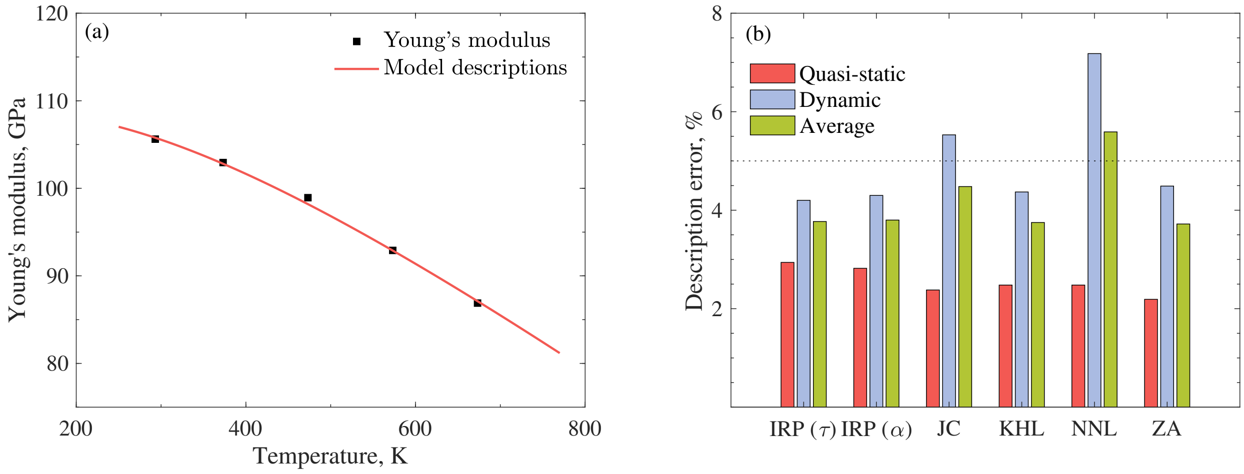

Figure 4.13: The temperature dependence of the Young's modulus (a) and the description error of different models for Ti-6Al-4V. The symbols are the experimentally measured Young's modulus. The solid line is the corresponding model description.

Figure 4.14 presents stress-strain diagrams and model descriptions at various strain rates and temperatures. The initial parameter values for the KHL, NNL, and ZA model for HCP metals are established based on works [74], [106], and [107], respectively. These values are then optimized using a constrained optimization procedure to minimize the errors between descriptive and experimental results. The final parameter values used in the JC, KHL, NNL and ZA models are listed in tables 4.8, 4.9, 4.10 and 4.11, respectively. The parameter values used in the IRP model are provided in table 4.5 and table 4.6 or 4.7. Figure 4.13 (b) reports the description errors of different models, among which the IRP, JC, KHL and the ZA model provide relatively accurate results. Nevertheless, the ZA model performs well at the expense of its hardening behavior at low strain rates. Among with all mentioned constitutive models, only the IRP model can feature the tendency of the non-monotonic pattern of the flow curves at high loading rates.

4.2.5 Main difference between constitutive models and ANN model

In this paper, the term "constitutive models" is specifically referred to phenomenological and physical-based models as shown in expressions (2.38)–(1.16). As discussed in section 1.4, the ANN model approximates the constitutive relationship $\sigma = F(\varepsilon_p, \dot{\varepsilon}, T)$ by a composition of the active function (1.20) and the linear regression (1.21), which requires a large number of weight and bias parameters. Therefore, the ANN model uses a data-driven learning approach, while constitutive models are proposed by the rule-based analyzing method. This is the main difference between the ANN model and different constitutive models. We explore this difference in two aspects: methodology of data analysis and interpretability.

One of the main advantages of ANN algorithm is its generality. The performance of the ANN model is data-driven, instead of being rule-based. It can "automatically" extract even implicit features or behavior patterns of the given dataset, disregarding the type or meaning of the data. This generality is a feature of most approximation algorithms, but the ANN seems to provide a more powerful approximation method (1.18) than the classical approaches (1.17) do. It can prove to be more advantageous in tackling intricate multi-dimensional problems. However, due to the data-driven feature, it is more sensitive to data quality. In machine learning, a model trained too well on the training dataset can become overcomplex, resulting in poor generalization to new, unseen data. This is overlearning of the model and it can happen when the model has too many parameters or is trained for too many epochs, causing it to fit the noise or random fluctuations in the training data. Overlearning in the ANN model can be detected by evaluating its performance on a separate validation dataset. Hence, to analyze data and extract a specific pattern from them, ANN model requires data to be separated into, at least, two groups: the training dataset

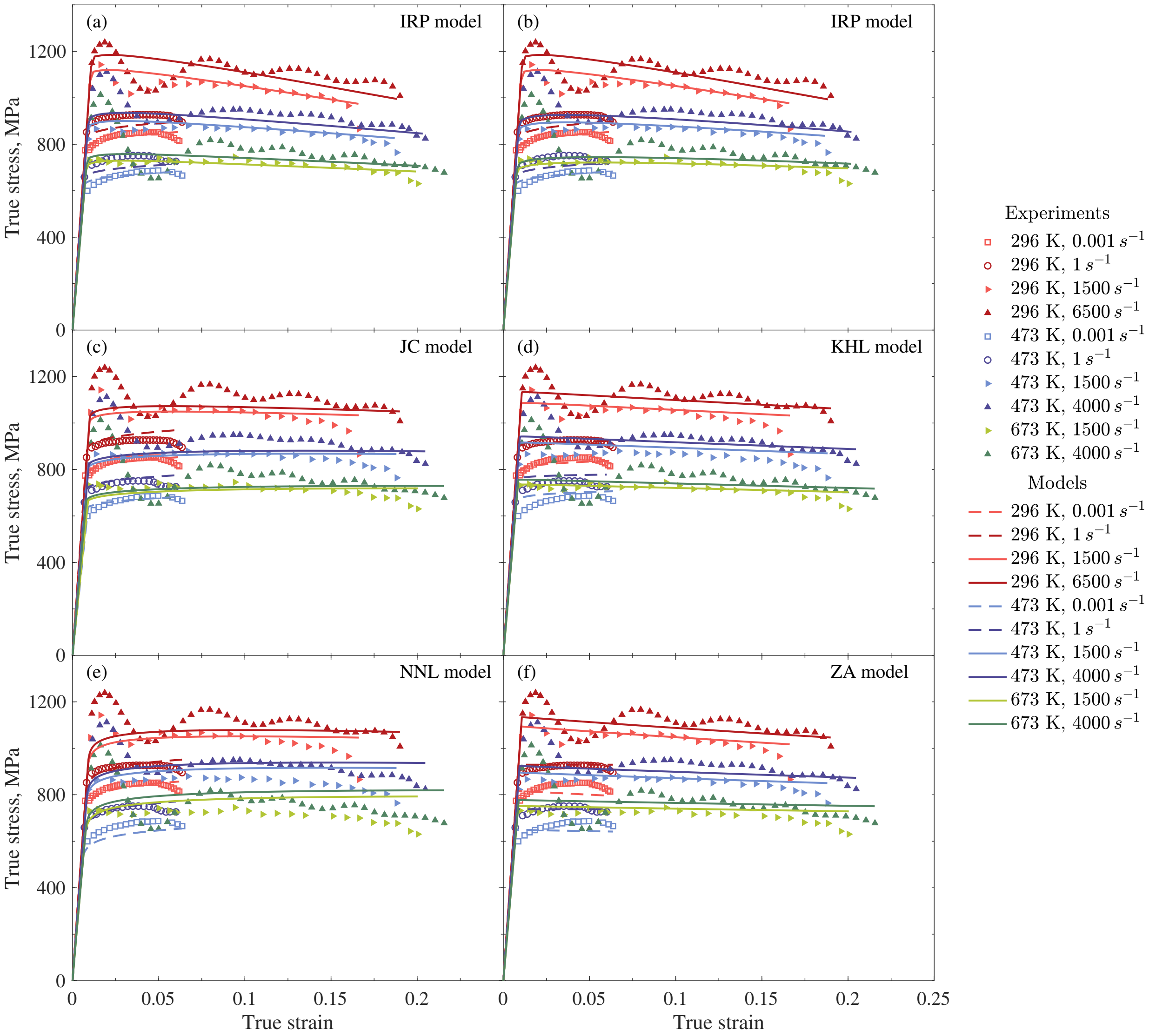

Figure 4.14: The stress-strain diagrams at 3 temperatures and 5 high loading rates and the corresponding simulation performed by the IRP model with the temperature-dependent τ (a), the IRP model with the temperature-dependent α (b), JC model (c), KHL model (d), NNL model for HCP metals (e) and the ZA model for HCP metals (f).

and the validation dataset. The validation dataset is often used for artificially adjusting values of hyper-parameters in relatively simple cases. The descriptive ability of an ANN model can be attributed to its capacity to extract implicit behavior patterns from the available data, including both the training and validation datasets. In contrast, constitutive models are rule-based. Behavior patterns have been mathematically summarised in them beforehand using a few parameters. And these are performed by the reliable scientific and interpretable analysis of the experimental facts. All given data can be used to validate their descriptive ability, and they are not likely to fit any noise or random fluctuations in data. The descriptive ability of constitutive models is determined by their ability to fit mathematically established rules/patterns to the existing data. Thus, their descriptive and predictive abilities are limited. The new abnormal physical phenomena often require the introduction of additional terms to the existing model basis, while the use of ANN model does not need such modifications.

The ANN model, with a "black box" nature, is not likely to interpret the physical meaning of parameters or the model itself. It might be a certain pure empirical model, but with a large number of parameters. This is also a consequence of its data-driven feature. Instead, the constitutive models show the interpretable meanings of their parameters. For example, the JC model uses the melting temperature T_m and the strain hardening exponent n corresponding to the hardening behavior.

Generally, fundamental principles or frameworks of mechanics are always required to be simple, clear, and “visualizable” for human investigators, and, more importantly, reliable. The reliability is protected by mathematically summarised rules, instead of a group of active functions and regressions, which may have unstable behaviors and technical challenges. Therefore, machine learning is not recommended for summarising or describing fundamental principles due to its poor interpretability. However, it can be used to describe and predict the consequences of fundamental principles, especially in intricate cases. After general topics, we continue to compare the performance of different models through the example of the Tungsten-based composite discussed in section 4.2.3.

A good performance of the ANN model in describing stress-strain diagrams on its training dataset is less valuable compared with that on its validation dataset. For the Tungsten-based composite, experimental data at a strain rate of $1000\,s^{-1}$

and different temperatures are selected to be the validation dataset. This allows us to test the performance of the model at a high strain rate, which belongs to the "learned" strain rate range from $200\,s^{-1}$ to $3000\,s^{-1}$. With this validation dataset, it can be assessed whether the model is overfitting to the training data or not. The description errors of all mentioned models on the validation dataset are shown in figure 4.12 (b). Except for the JC, KHL and ANN model, all other models exhibit a description error of less than 5%. However, this does not necessarily imply that the ANN model has poorer performance than many other models. Instead, the deviation of the ANN model's description from the dataset, and mainly at a temperature of 288 K and strain rate of $1000\,s^{-1}$, is more likely due to the "abnormal" behavior of flow stresses at a temperature of 288 K and a strain rate of $200\,s^{-1}$. As illustrated in figures 4.9, all constitutive models tend to overestimate these flow stresses denoted by the pink diamonds. More importantly, figures 2.5 (b) and (d) indicate that the experimentally measured flow stresses at a temperature of 288 K and a strain rate of $200\,s^{-1}$ does not follow the common decreasing behavior pattern of the RS factor. In other words, constitutive models, as rule-based models, are limited describing this "abnormal" behavior of flow stresses. However, the ANN model, with a data-driven feature, is capable of perfectly capturing this "abnormal" behavior during its training. Therefore, its underestimated description of stresses at the temperature of 288 K and strain rates higher than $200\,s^{-1}$, shown in figure 4.11 (c), is reasonable. By training the ANN model with a few more data points at the temperature of 288 K and strain rates higher than $200\,s^{-1}$, the description error is likely to be easily reduced to less than 5%.

4.3 Validation of the calculation scheme for RP model through finite element analysis

To validate the calculation scheme developed in section 3.3.2 for the simplified version of RP model (3.53), the SHPB setup is simulated using the commercial software package ABAQUS/Explicit. This package implements the explicit central difference method to solve the dynamic equation (3.31). The time step is chosen by ABAQUS/Explicit to ensure stability, but for added accuracy, the maximum time step is set to 0.2 μs. The work by Zhuang et al. [108] provides optimized dimensions for the incident and transmission bars to minimize computational resources. The recommended sizes are $\varnothing 25 \times 1000$ mm for the bars and $\varnothing 18 \times 22$ mm for the sample. The mechanical properties of the incident and transmission steel bars are as follows:

$$E = 200\text{GPa}, \nu = 0.3, \rho = 7.85 \text{ g/cm}^3$$

The sample used is the 603 steel investigated by Xu and Huang [109]. Figure 4.15 presents the experimental data and model behavior at quasi-static rates and impact loading rates of 2000 s^{-1} and 4500 s^{-1}. The impact cases are mainly focused here. The elastic modulus values are $E = 200$ GPa, $\nu = 0.3$. The model parameters are set to $\sigma_y = 850$ MPa, $K = 505.15$ MPa, $n = 0.40$, $\tau = 1.4 \times 10^{-4}$ s and $\alpha = 35$.

To take advantage of the symmetry in both geometry and boundary conditions, a 3D quarter-geometry of the bars and sample is created, as shown in figures 4.16a and 4.16b. The element type C3D8R is used. The contact between bars and samples are set to be hard (no friction, no thermal interactions, etc.). The experimental setup, including the boundary conditions, is illustrated in figures 4.17a and 4.17b. The cross-section normal to the x-axis is constrained by no-rotation conditions and a displacement condition of $u_x = 0$. Similarly, the cross-section normal to the y-axis is constrained by no-rotation conditions and a displacement condition of $u_y = 0$. The left side of the incident bar is subjected to stress pulses, as depicted in figures 4.18a and 4.18b. For instance, the stress pulse shown in figure 4.18a results in a strain rate of 2000 s^{-1} in the sample. In this case, figure 4.19a demonstrates that the stress state in the sample remains approximately uniform during loading. Additionally, figures 4.20a and 4.20b reveal that the strain ε_{33} and stress history σ_{33} of elements 182, 801, and 1497 (shown in figure 4.19b) validate the uniformity of the stress state. Another stress pulse, as shown in figure 4.18b, produces a strain rate of 4500 s^{-1}. The σ_{33}–ε_{33} diagrams obtained through FEA at two impact loading rates are presented in figure 4.21. The simulation results exhibit good agreement with the experimental data, which confirms the reliability of the RP model (3.53) and the developed calculation scheme.

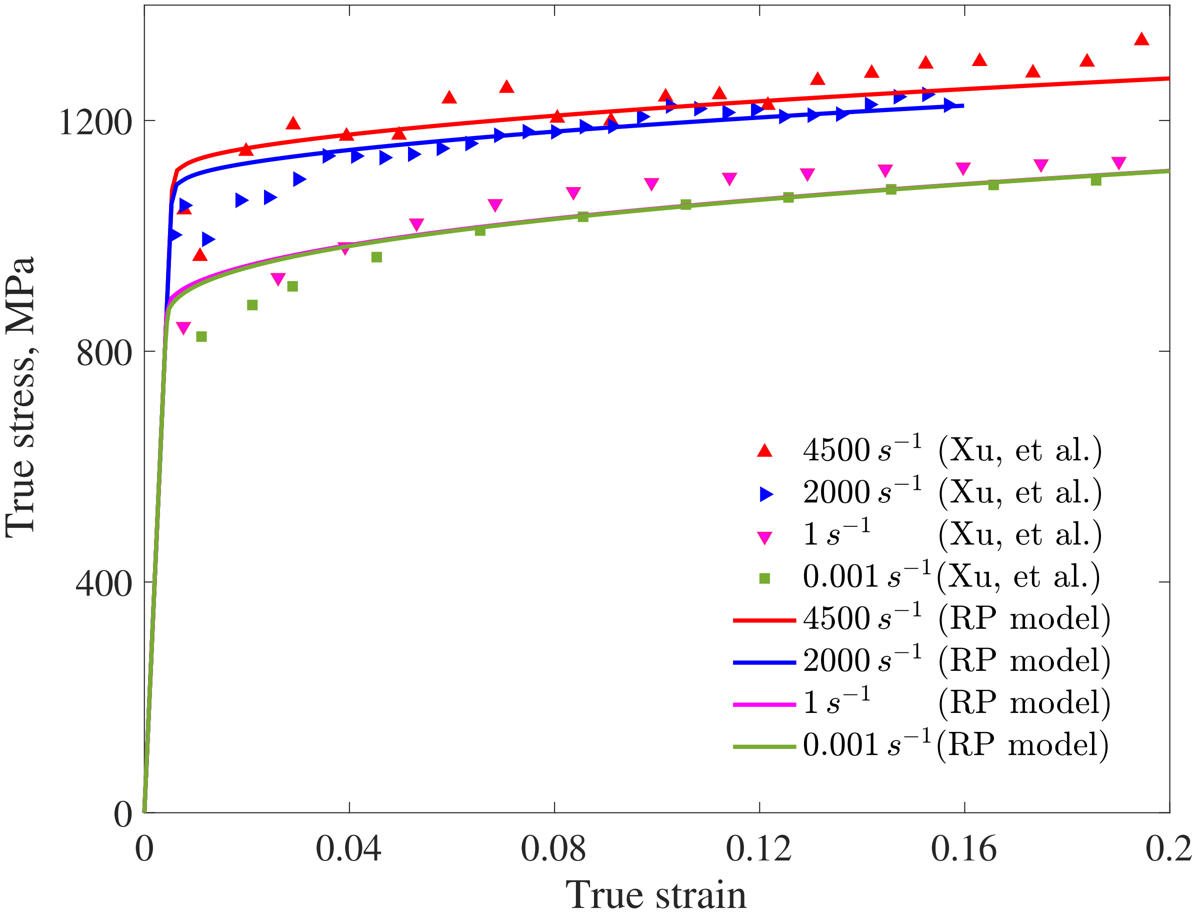

Figure 4.15: True stress-true strain diagrams for the 603 steel at different strain rates and the performance of the RP model

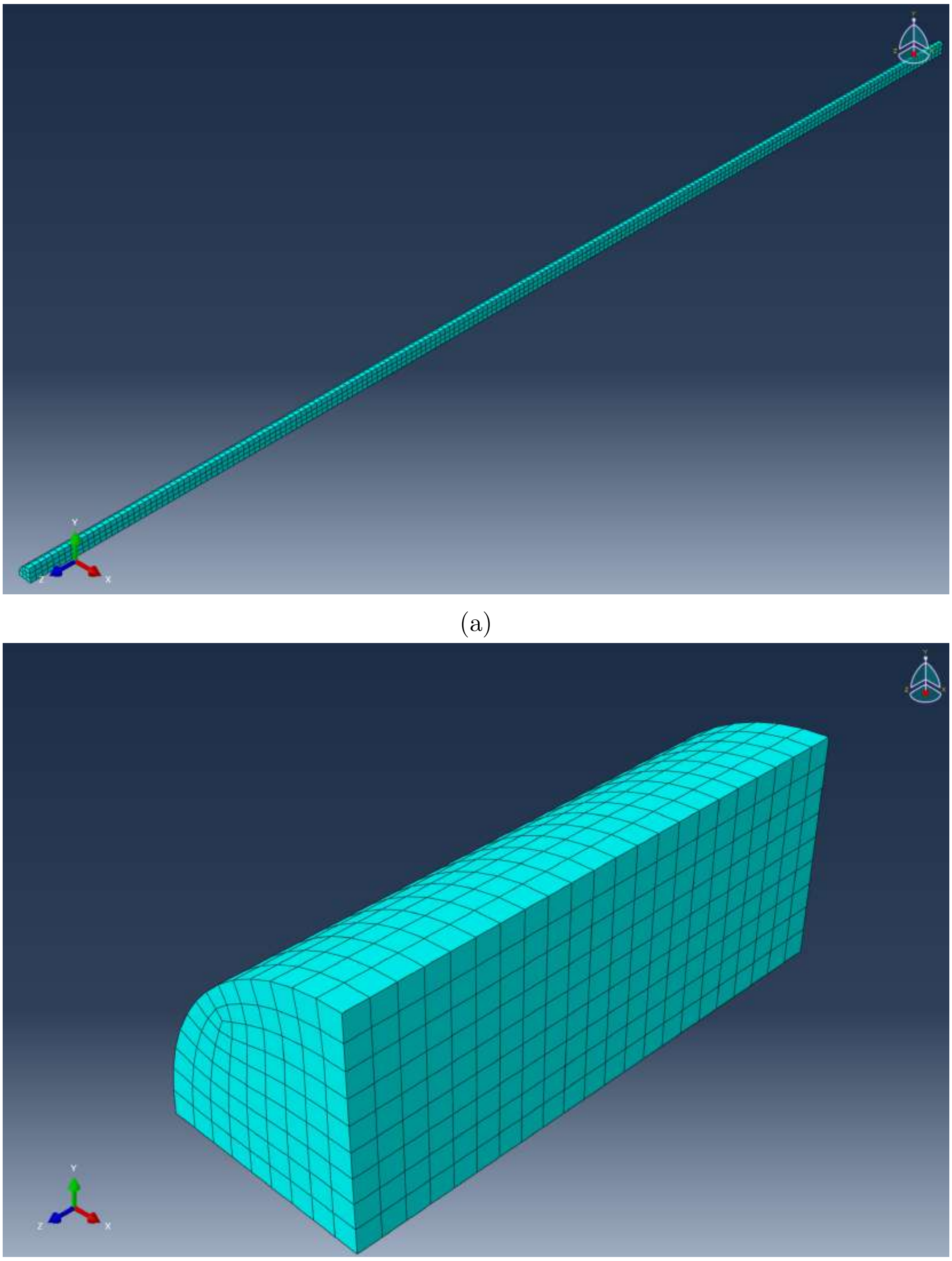

(a)

(b)

Figure 4.16: The geometry for the simulation: (a) A quarter of the incident and/or transmission bar, (b) a quarter of the sample.

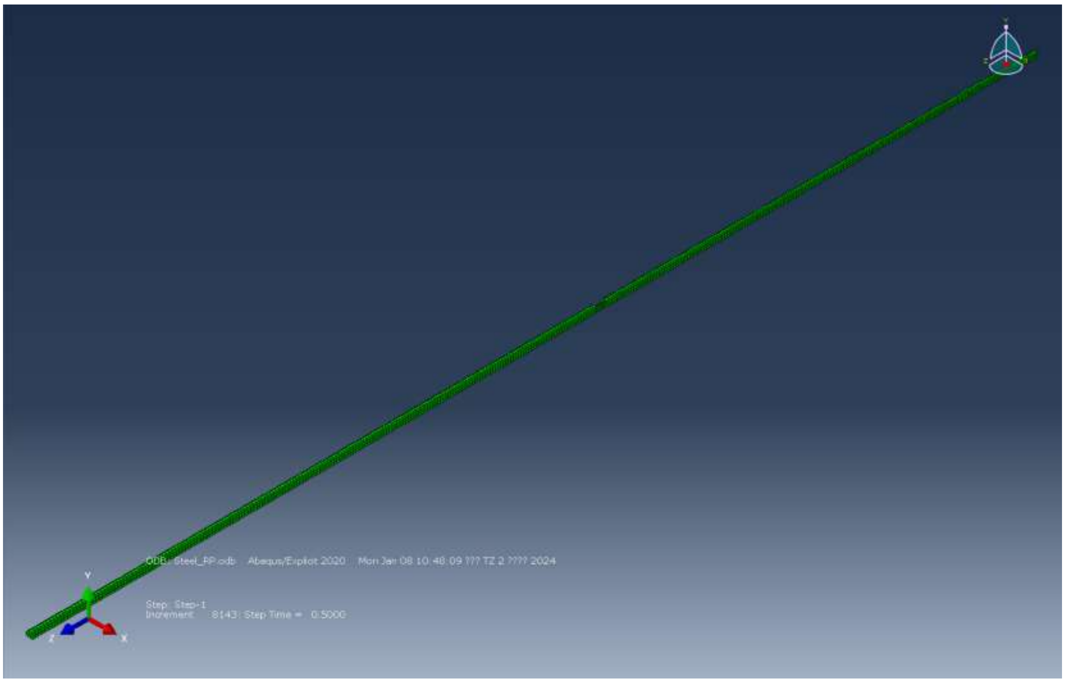

```
ODB: Steel_RP.odb    Abaqus/Explicit 2020    Mon Jan 08 10:48:09 ??? TZ 2 ???? 2024

Step: Step-1
Increment     8143: Step Time =    0.5000
```

(a)

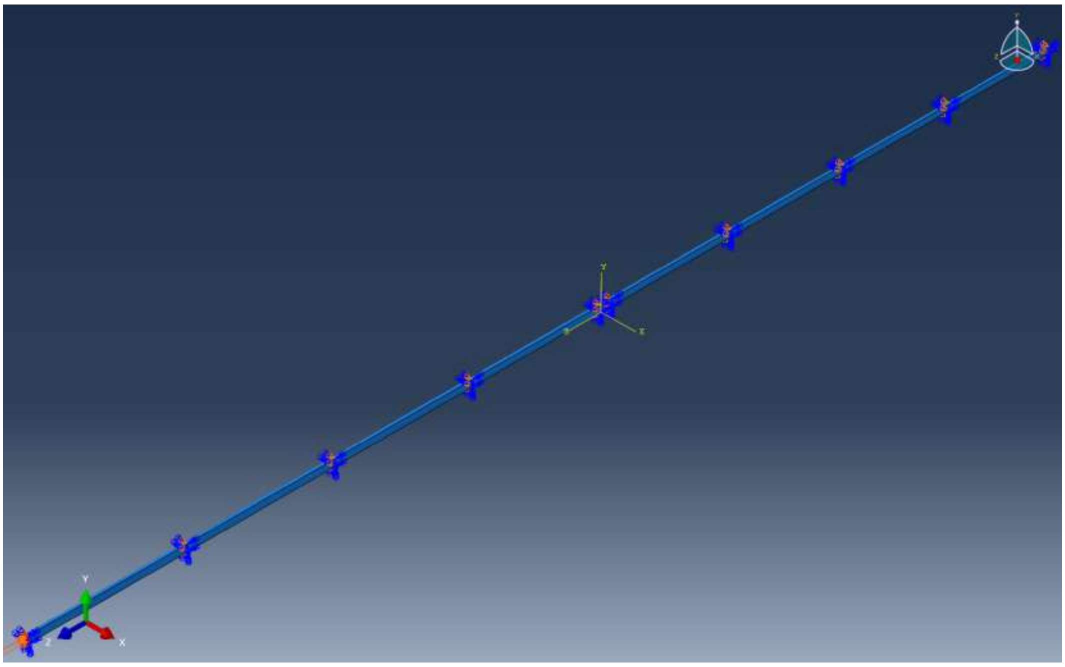

(b)

Figure 4.17: The assembled geometry (a) and boundary conditions (b)

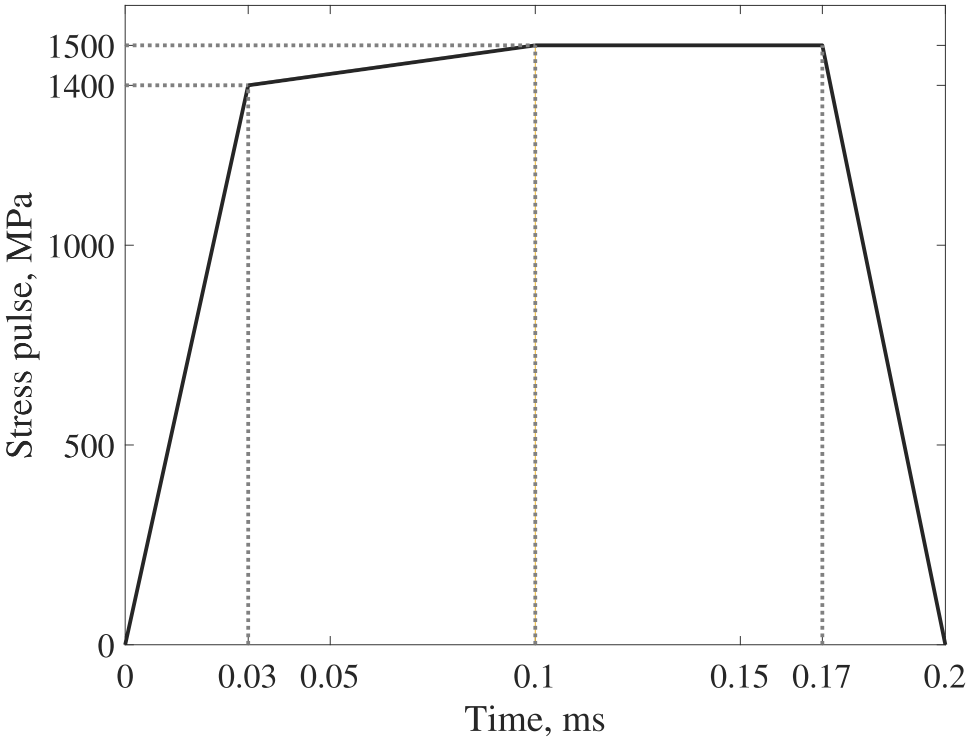

(a)

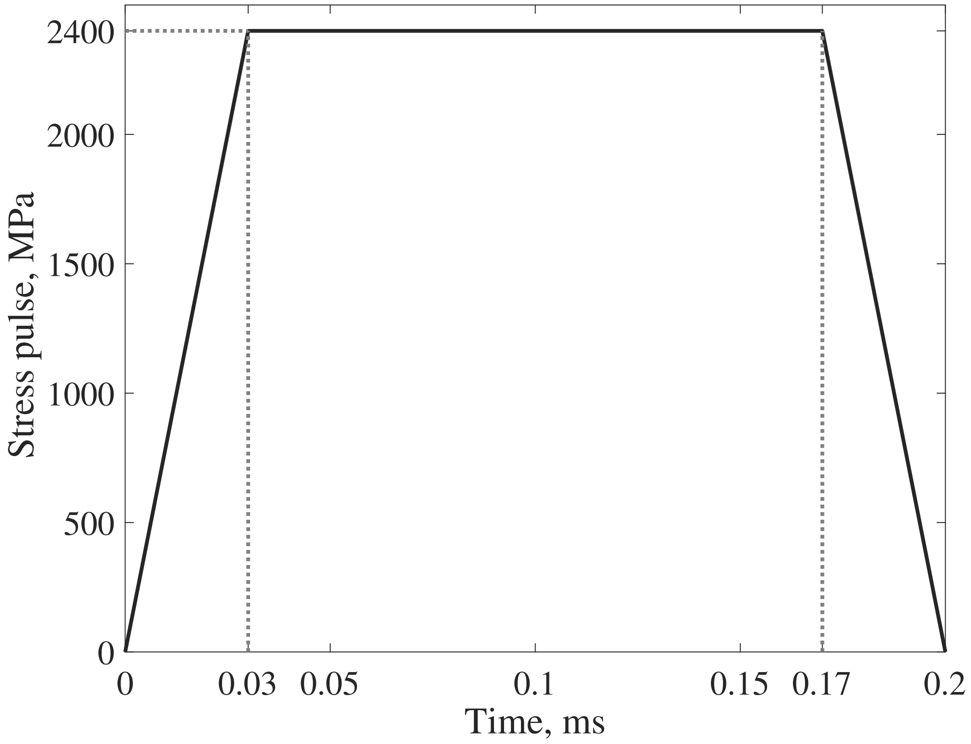

(b)

Figure 4.18: The stress pulses loaded on the left side of the incident bar causes two different strain rates of the sample: (a) $\dot{\varepsilon} = 2000\ s^{-1}$, (b) $\dot{\varepsilon} = 4500\ s^{-1}$.

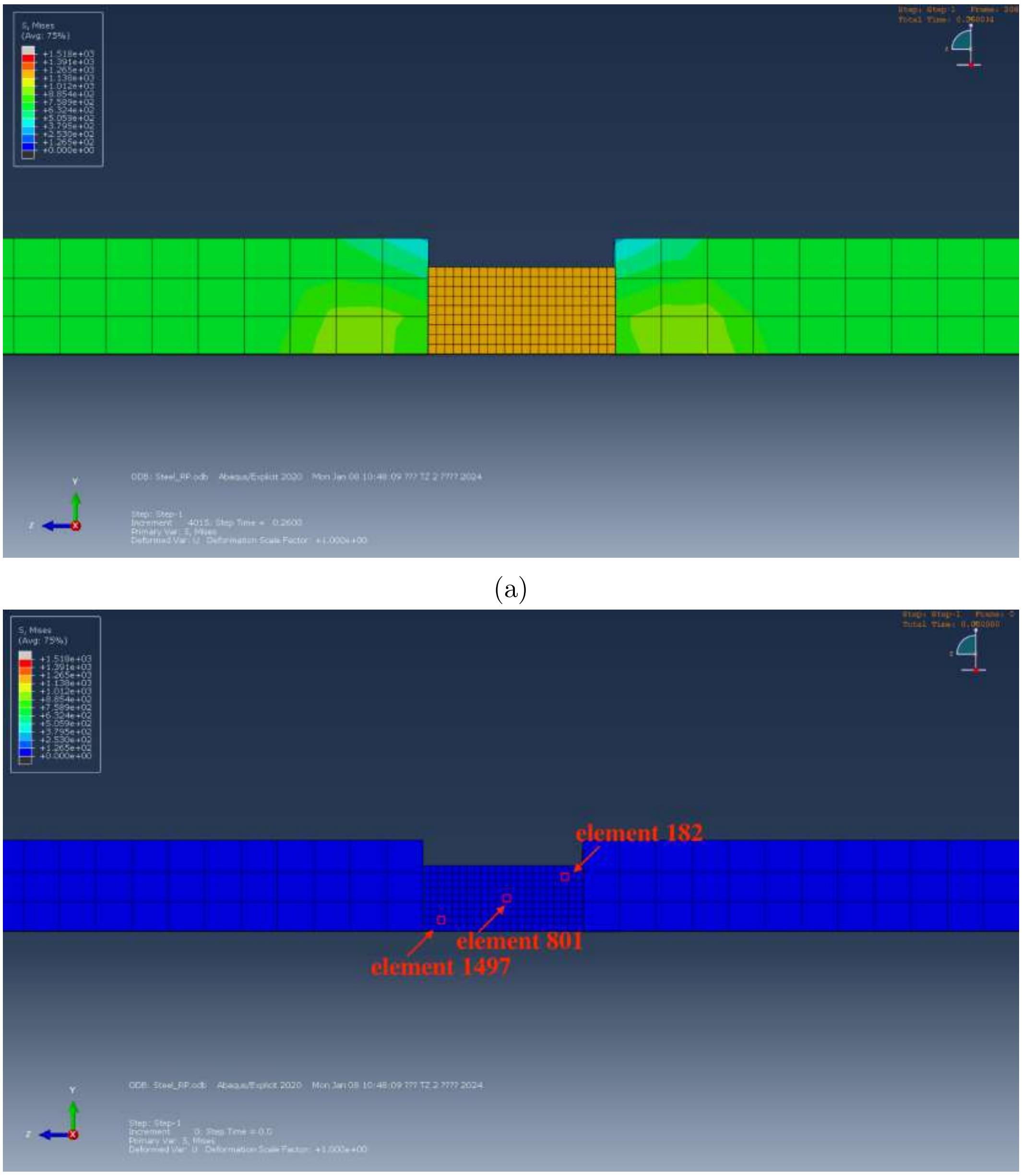

(a)

(b)

Figure 4.19: Stress distribution in sample during the loading (a) and elements selected for analysis (b)

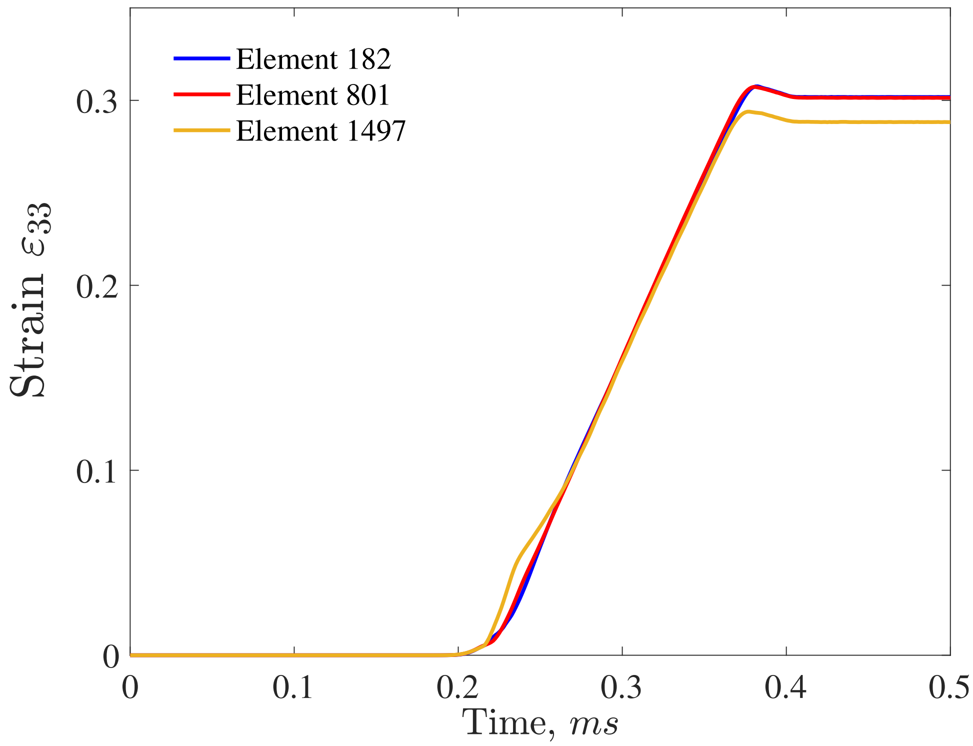

(a)

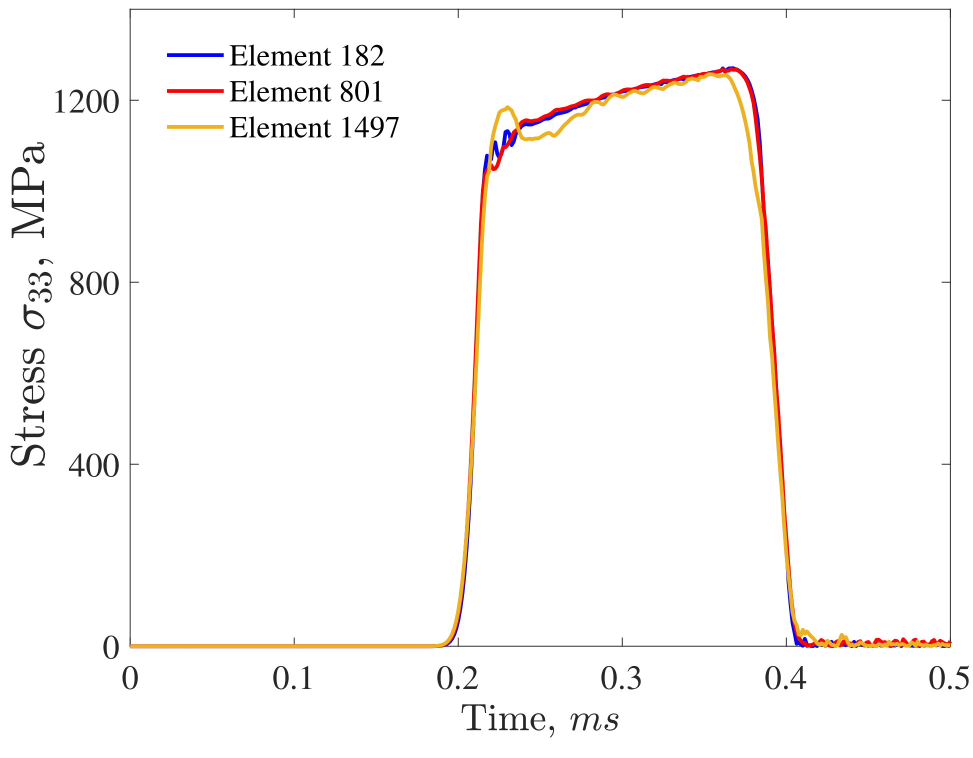

(b)

Figure 4.20: Strain history (a) and stress history (b) of three different elements.

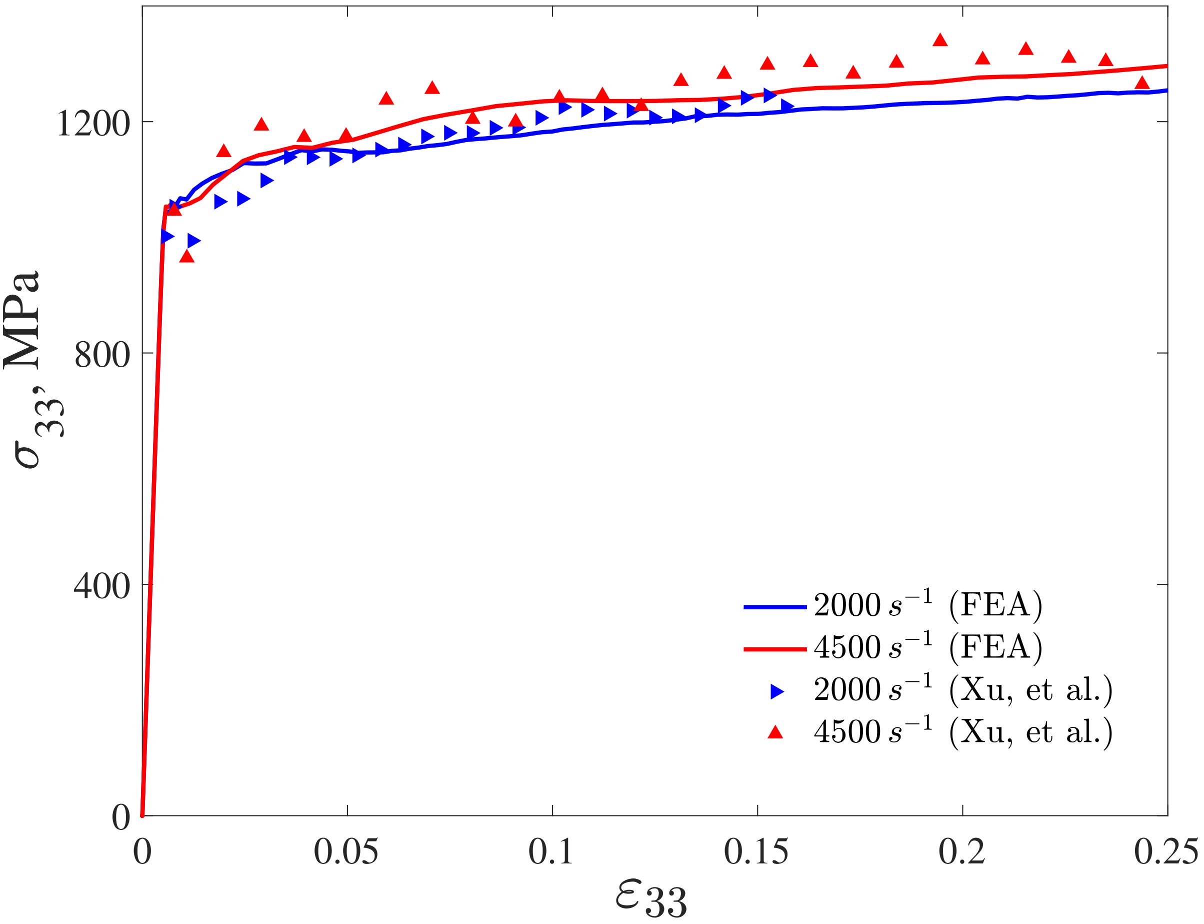

Figure 4.21: Comparison of stress-strain diagrams at strain rates of 2000 s^{-1} and 4500 s^{-1} between FEM simulations and experimental data.

Conclusions

In this work, modeling of dynamic plasticity problems is studied. Strain rate effects and thermal softening phenomenon of a group of metallic materials, as well as their negative hardening induced by the rapid plastic dissipation, are successfully simulated within the framework of the incubation time approach. A comprehensive analysis of the framework of the modified relaxation model of plasticity (RP model) is given. The finite element analysis is conducted to assess the accuracy and reliability of the computational approach developed for the RP model.

The following main conclusions are made:

1. The framework of the modified RP model is proposed. A simplified version and incremental version of the RP model are developed. The relaxation function $\gamma(\varepsilon_p(t))$ involves the dynamic stress intensity $M_\alpha(\cdot)$ to characterize strain rate effects instead of introducing an empirical rate-dependent component. The yield surface equation using incubation time approach is proposed. The incubation time approach considers the rate sensitivity as a manifestation of time sensitivity of materials.

2. A methodology of investigating the temperature-time correspondence, i.e. temperature dependence of the incubation time, is discussed. The relative stress (RS) factor can be used to analyze the tendency of the temperature-time relationship over a wide range of strain, strain rate and temperature. For studied HSLA-65 steel and Tungsten-based composite, the RS factors at different strain rates generally exhibit a monotonic decrease with increasing temperature. This implies that the temperature rise results in a monotonic decrease in τ. Some special cases of non-monotonic behavior may also occur due to, for instance, the dynamic strain aging, and a non-monotonic relation between τ and the temperature might be required.

3. Several possible temperature-time correspondences given in expressions (2.31)–(2.34) are discussed. Since any temperature-time correspondence ensuring a modeling error within 5% may be considered technically suitable, different phenomenological temperature-time relations were proposed previously and verified to be available. Exponential or power phenomenological relationships are preferable choices to avoid negative values of τ.

4. A comparative analysis is made between the effectiveness of the temperature-time principle with a constant value of parameter α and the dependence of parameter α on temperature with a constant value of parameter τ. Simulation results indicate that the modeling capabilities of relations (2.34) and/or (2.37) are almost equivalent.

5. The multiplicative form $\sigma = f_1(\varepsilon_p, \dot{\varepsilon}) f_2(\varepsilon_p, T)$ is improper to simulate the strain-rate effect and thermal softening phenomenon over a wide temperature range. Experiments demonstrate that the RS factor has a clear rate-dependent and temperature-dependent behavior pattern, which must be followed by the temperature-time correspondence. However, the multiplicative models $\sigma = f_1(\varepsilon_p, \dot{\varepsilon}) f_2(\varepsilon_p, T)$ is derived from the direct empirical fitting approach and results in a temperature-independent RS factor. In these models, dynamic relations are conventionally constructed in the way of direct extrapolation of static notions into dynamic cases using special terms incorporated into well-known static formula. Nevertheless, they are still very convenient for engineering problems where the temperature does not vary significantly.

6. The developed RP model is evaluated based on experimental data from various metallic materials including aluminium alloy 6082-T6, 2519A, HSLA-65 steel, 93W–4.9Ni–2.1Fe tungsten-based composite, and titanium alloy Ti-6Al-4V. A comparison is made between the descriptive ability of the IRP model and other phenomenological models, micromechanism-based models, and the artificial neural network (ANN) model. The IRP model provides a good descriptive ability and, specifically, can feature the tendency of the non-monotonic/softening behavior of the stress-strain curves at high loading rates.

7. Based on experimental facts of 93W–4.9Ni–2.1Fe tungsten-based composite, the

main difference between ANN model and other constitutive models is examined. The ANN model uses a data-driven learning approach, while other constitutive models are proposed by the rule-based analyzing method. The choice of modeling approach should depend on the specific material and loading conditions being studied, as well as the desired level of accuracy and computational complexity.

8. The negative hardening response of HSLA-65 steel caused by the rapid plastic dissapation is successfully simulated by the IRP model. The adiabatic temperature rise in the material results in a decrease in the characteristic relaxation time (or incubation time) as indicated by the temperature-time correspondence.
9. A computational approach is developed for the simplified version of RP model and validated through the finite element analysis. Software modules have been developed for calculating stress-strain diagrams of various materials, determining parameters of different models, and solving three-dimensional dynamic plasticity problems. The simulation results exhibit good agreement with existing experimental data, which confirms the reliability of the RP model and the developed calculation scheme.

Appendices

A The integral yield criterion.

Assuming a constant strain rate, i.e. $\sigma(t) = E\dot{\varepsilon}tH(t)$, where $H(t)$ is the Heaviside function, one may have

$$\begin{aligned} I(t) &= \frac{1}{\tau}\int_{t-\tau}^{t}\left(\frac{\sigma(s)}{\sigma_y}\right)^{\alpha} ds = \frac{E^{\alpha}\dot{\varepsilon}^{\alpha}}{\sigma_y^{\alpha}\tau}\int_{t-\tau}^{t} s^{\alpha}H(s)ds \\ &= \frac{E^{\alpha}\dot{\varepsilon}^{\alpha}}{\sigma_y^{\alpha}\tau}\cdot\left.\frac{s^{\alpha+1}H(s)}{1+\alpha}\right|_{t-\tau}^{t} \\ &= \frac{(E\dot{\varepsilon}t)^{\alpha+1}H(t) - (E\dot{\varepsilon}t - E\dot{\varepsilon}\tau)^{\alpha+1}H(t-\tau)}{(1+\alpha)\sigma_y^{\alpha}E\dot{\varepsilon}\tau} \\ &= \frac{\sigma(t)^{\alpha+1}H(t) - (\sigma(t) - E\dot{\varepsilon}\tau)^{\alpha+1}H(t-\tau)}{(1+\alpha)\sigma_y^{\alpha}E\dot{\varepsilon}\tau} \end{aligned} \tag{A.4}$$

According to the integral yield criterion 2.1, the plastic process begins when $I(t_y) = 1$ takes place. Thus, the rate-dependent yield stress (or strength) $\sigma_{dy} = \sigma(t_y)$ can be derived by A.5, where $H(\sigma_{dy} - E\dot{\varepsilon}\tau) = (E\dot{\varepsilon})\cdot H(t_y - \tau) = H(t_y - \tau)$.

$$\sigma_{dy}^{1+\alpha} - (\sigma_{dy} - E\dot{\varepsilon}\tau)^{1+\alpha} H(\sigma_{dy} - E\dot{\varepsilon}\tau) = (1+\alpha)(E\dot{\varepsilon}\tau)\sigma_y^{\alpha} \tag{A.5}$$

Now let us consider the case when $t_y = \tau$ or $\sigma_{dy} = E\dot{\varepsilon}\tau$. The equation A.5 transforms into equation A.6

$$\sigma_{dy}^{1+\alpha} = \sigma_y^{\alpha}(1+\alpha)(E\dot{\varepsilon}\tau) = (1+\alpha)\sigma_{dy}\sigma_y^{\alpha}, \tag{A.6}$$

which derives $\sigma_{dy} = (1+\alpha)^{1/\alpha}\sigma_y$ or $\dot{\varepsilon} = \frac{\sigma_y(1+\alpha)^{\frac{1}{\alpha}}}{E\tau}$. Thus, the equation A.5 can also be represented in the form A.7.

$$\begin{cases} \sigma_{dy}^{1+\alpha} - (\sigma_{dy} - E\dot{\varepsilon}\tau)^{1+\alpha} = (1+\alpha)(E\dot{\varepsilon}\tau)\sigma_y^{\alpha}, & \dot{\varepsilon} \le \frac{\sigma_y(1+\alpha)^{\frac{1}{\alpha}}}{E\tau}; \\ \sigma_{dy} = \left((1+\alpha)(E\dot{\varepsilon}\tau)\sigma_y^{\alpha}\right)^{\frac{1}{1+\alpha}}, & \dot{\varepsilon} > \frac{\sigma_y(1+\alpha)^{\frac{1}{\alpha}}}{E\tau}. \end{cases} \tag{A.7}$$

B The mean shear stress.

The mean shear stress $\bar{\sigma}_\tau$ proposed by Novozhilov V. V. at the point M is defined as

$$\bar{\sigma}_\tau = \lim_{r\to 0}\left(\frac{1}{\Omega}\iint \sigma_\tau^2 d\Omega\right)^{\frac{1}{2}}, \tag{B.8}$$

where Ω is the area of the spherical surface enclosing the point M, $d\Omega$ is the area of an infinitesimal plane on the surface Ω, r is the radius of the surface Ω, σ_τ is the shear stress on the plane $d\Omega$. For the sake of better readability, both the surface area and the surface could be denote by $d\Omega$ or Ω depending on the context.

Let us denote unit orthogonal vectors in three principal directions at considered point M by $\underline{e_1}, \underline{e_2}, \underline{e_3}$ and the normal vector of the plane $d\Omega$ by $\underline{n}$ with components n_i (i = 1,2,3). Then, the traction vector $\underline{t}$ on the plane $d\Omega$ is given by equation B.9

$$\underline{t} = \boldsymbol{\sigma} \cdot \underline{n} = \left(\sigma_i \underline{e_i} \otimes \underline{e_i}\right) \cdot \underline{n} = \sigma_i n_i \underline{e_i}, \tag{B.9}$$

where $\boldsymbol{\sigma}$ is the Cauchy stress tensor; σ_i is the principal stress in the direction of $\underline{e_i}$, and it is considered the principal stress at point M when r approaches 0. The magnitude of the normal stress component σ_n and the shear stress component σ_τ can be derived as follows.

$$\begin{aligned} \sigma_n &= \underline{t} \cdot \underline{n} = \sigma_i n_i^2, \\ \sigma_\tau &= |\underline{t} - \sigma_n \underline{n}| = \sqrt{(\sigma_i^2 n_i^2) - (\sigma_j n_j^2)^2} \end{aligned} \tag{B.10}$$

In the spherical coordinate system with the unit basis $(\underline{e_1}, \underline{e_2}, \underline{e_3})$, the area of the plane $d\Omega$ and the spherical surface Ω and components of the normal vector $\underline{n}$ are

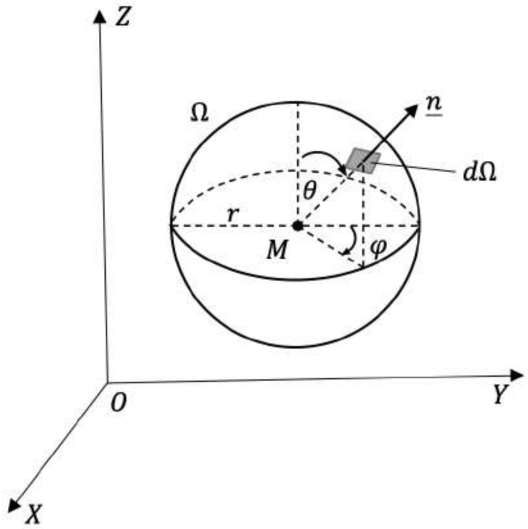

Figure B.1: The spherical face Ω enclosing the point M. r is the radio of the sphere and $d\Omega$ is an infinitesimal plane on the surface Ω with a normal vector $\underline{n}$. θ and φ are polar angle and azimuthal angle, respectively.

defined by

$$\begin{gathered} d\Omega = r^2 \sin\theta d\varphi d\theta; \\ \Omega = 4\pi r^2; \\ n_1 = \sin\theta\sin\varphi, n_2 = \sin\theta\cos\varphi, n_3 = \cos\theta; \\ \theta \in [0,\pi), \varphi \in [0,2\pi). \end{gathered} \tag{B.11}$$

The graphical illustration is shown in figure B.1. Therefore, the magnitude of the shear stress component can be derived from the equations B.10 and B.11 and given by equation B.12.

$$\begin{gathered} \sigma_\tau^2 = \sigma_1^2 \sin^2\theta\sin^2\varphi + \sigma_2^2\sin^2\theta\cos^2\varphi + \sigma_3^2\cos^2\theta - \\ - \left(\sigma_1\sin^2\theta\sin^2\varphi + \sigma_2\sin^2\theta\cos^2\varphi + \sigma_3\cos^2\theta\right)^2 \end{gathered} \tag{B.12}$$

And the integral in expression B.8 is transferred into the equation B.13.

$$\begin{aligned} \bar{\sigma}_\tau^2 =& \frac{1}{4\pi}\int_0^{2\pi} d\varphi \int_0^{\pi} \left\{\sigma_1^2\sin^2\theta\sin^2\varphi + \sigma_2^2\sin^2\theta\cos^2\varphi + \sigma_3^2\cos^2\theta - \right. \\ & \left. - \left(\sigma_1\sin^2\theta\sin^2\varphi + \sigma_2\sin^2\theta\cos^2\varphi + \sigma_3\cos^2\theta\right)^2\right\} \sin\theta d\theta \\ =& \frac{1}{15}\left[(\sigma_1-\sigma_2)^2 + (\sigma_2-\sigma_3)^2 + (\sigma_3-\sigma_1)^2\right] \end{aligned} \tag{B.13}$$

Thus, the shear stress intensity T (see expression 2.7) and the mean shear stress $\bar{\sigma}_\tau$

are equivalent, to within a constant factor, and are related by the expression B.14.

$$T = \sqrt{\frac{2}{15}}\bar{\sigma}_\tau = \sqrt{\frac{2}{15}} \lim_{r \to 0} \left(\frac{1}{\Omega} \iint \sigma_\tau^2 d\Omega \right)^{\frac{1}{2}} \tag{B.14}$$

Relation B.14 indicates that the stress intensity is not just an invariant with respect to the stress tensor, but also characterises the "mean" stress behaviour in the space.

Bibliography

[1] Johnson G.R., Cook W.H. A constitutive model and data for metals subjected to large strains, high strain rates and high temperatures // Proceedings of the 7th International Symposium on Ballistics. — Vol. 21. — The Hague, The Netherlands, 1983. — P. 541–547.

[2] Rusinek A., Klepaczko J.R. Shear testing of a sheet steel at wide range of strain rates and a constitutive relation with strain-rate and temperature dependence of the flow stress // International Journal of Plasticity. — 2001. — Vol. 17, no. 1. — P. 87–115.

[3] A computational determination of the Cowper–Symonds parameters from a single Taylor test / C. Hernandez, A. Maranon, I.A. Ashcroft, J.P. Casas-Rodriguez // Applied Mathematical Modelling. — 2013. — Vol. 37, no. 7. — P. 4698–4708.

[4] Lin Y.C., Chen X.M., Liu G. A modified Johnson-Cook model for tensile behaviors of typical high-strength alloy steel // Materials Science and Engineering: A. — 2010. — Vol. 527, no. 26. — P. 6980–6986.

[5] Gambirasio L., Rizzi E. An enhanced Johnson–Cook strength model for splitting strain rate and temperature effects on lower yield stress and plastic flow // Computational Materials Science. — 2016. — Vol. 113. — P. 231–265.

[6] Nemat-Nasser S., Isaacs J.B. Direct measurement of isothermal flow stress of metals at elevated temperatures and high strain rates with application to Ta and TaW alloys // Acta Materialia. — 1997. — Vol. 45, no. 3. — P. 907–919.

[7] Zerilli Frank J., Armstrong Ronald W. Dislocation-mechanics-based constitutive relations for material dynamics calculations // Journal of Applied Physics. — 1987. — Vol. 61, no. 5. — P. 1816–1825.

[8] Gruzdkov A. A., Petrov Yu V. On temperature-time correspondence in high-rate deformation of metals // Doklady Physics. — 1999. — Vol. 44, no. 2. — P. 114–116.

[9] Thermal Effect in Dynamic Yielding and Fracture of Metals and Alloys / A.A. Gruzdkov, E.V. Sitnikova, N.F. Morozov, Yu.V. Petrov // Mathematics and Mechanics of Solids. — 2009. — Vol. 14, no. 1-2. — P. 72–87.

[10] Selyutina N.S. Temperature relaxation model of plasticity for metals under dynamic loading // Mechanics of Materials. — 2020. — Vol. 150. — P. 103589.

[11] Zhao S. Software package for constructing stress-strain diagrams of metals under impact loading, calculated using an incremental relaxation model for plasticity (In russian). — 2023. — State registration of computer program No. 023684476, 11/15/2023.

[12] Yu Tongxi, Xue Pu. Chapter 12 - Introduction to dynamic plasticity // Introduction to Engineering Plasticity / Ed. by Tongxi Yu, Pu Xue. — Elsevier, 2022. — P. 327–371.

[13] Bagher Shemirani Alireza, Naghdabadi R., Ashrafi M.J. Experimental and numerical study on choosing proper pulse shapers for testing concrete specimens by split Hopkinson pressure bar apparatus // Construction and Building Materials. — 2016. — Vol. 125. — P. 326–336.

[14] Nemat-Nasser Sia, Guo Wei-Guo. Thermomechanical response of HSLA-65 steel plates: experiments and modeling // Mechanics of Materials. — 2005. — Vol. 37, no. 2. — P. 379–405.

[15] Roth Christian C., Fras Teresa, Mohr Dirk. Dynamic perforation of lightweight armor: Temperature-dependent plasticity and fracture of aluminum 7020-T6 // Mechanics of Materials. — 2020. — Vol. 149. — P. 103537.

[16] Xu Zejian, Huang Fenglei. Thermomechanical behavior and constitutive modeling of tungsten-based composite over wide temperature and strain rate ranges // International Journal of Plasticity. — 2013. — Vol. 40. — P. 163–184.

[17] Goviazin G.G., Shirizly A., Rittel D. Does plastic anisotropy affect the thermomechanical coupling in steel? // International Journal of Engineering Science. — 2023. — Vol. 187. — P. 103852.

[18] Garcia-Gonzalez D., Zaera R., Arias A. A hyperelastic-thermoviscoplastic constitutive model for semi-crystalline polymers: Application to PEEK under dynamic loading conditions // International Journal of Plasticity. — 2017. — Vol. 88. — P. 27–52.

[19] Importance of microstructure modeling for additively manufactured metal post-process simulations / Sumair Sunny, Glenn Gleason, Karl Bailey et al. // International Journal of Engineering Science. — 2021. — Vol. 166. — P. 103515.

[20] Johnson G. R., Holmquist T. J. An improved computational constitutive model for brittle materials // High-pressure Science and technology. — Vol. 309 of American Institute of Physics Conference Series. — 1994. — P. 981–984.

[21] Peng J. X., Li Y. L., Li D. H. An experimental study on the dynamic constitutive relation of tantalum (In Chinese) // Explosion and Shock Waves. — 2003. — Vol. 23, no. 2. — P. 183–187.

[22] Shokry Abdallah. A Modified Johnson–Cook Model for Flow Behavior of Alloy 800H at Intermediate Strain Rates and High Temperatures // Journal of Materials Engineering and Performance. — 2017. — Vol. 26, no. 12. — P. 5723–5730.

[23] A modified Johnson–Cook model for 7N01 aluminum alloy under dynamic condition / Yi-ben Zhang, Song Yao, Xiang Hong, Zhong-gang Wang // Journal of Central South University. — 2017. — Vol. 24, no. 11. — P. 2550–2555.

[24] Dynamic constitutive model of U75VG rail flash-butt welded joint and its application in wheel-rail transient rolling contact simulation / Jizhong Zhao, Xing Pang, Peilin Fu et al. // Engineering Failure Analysis. — 2022. — Vol. 134. — P. 106078.

[25] Experimental and numerical investigation on the ballistic resistance of 2024-T351 aluminum alloy plates with various thicknesses struck by blunt projec-

tiles / Jue Han, Yahui Shi, Qianqian Ma et al. // International Journal of Impact Engineering. — 2022. — Vol. 163. — P. 104182.

[26] Khan Akhtar S., Liang Riqiang. Behaviors of three BCC metal over a wide range of strain rates and temperatures: experiments and modeling // International Journal of Plasticity. — 1999. — Vol. 15, no. 10. — P. 1089–1109.

[27] Farrokh Babak, Khan Akhtar S. Grain size, strain rate, and temperature dependence of flow stress in ultra-fine grained and nanocrystalline Cu and Al: Synthesis, experiment, and constitutive modeling // International Journal of Plasticity. — 2009. — Vol. 25, no. 5. — P. 715–732.

[28] Characterization of hardening behaviors of 4130 Steel, OFHC Copper, Ti6Al4V alloy considering ultra-high strain rates and high temperatures / MingJun Piao, Hoon Huh, Ikjin Lee, Leeju Park // International Journal of Mechanical Sciences. — 2017. — Vol. 131-132. — P. 1117–1129.

[29] Evaluation of dynamic hardening models for BCC, FCC, and HCP metals at a wide range of strain rates / Hoon Huh, Kwanghyun Ahn, Ji Ho Lim et al. // Journal of Materials Processing Technology. — 2014. — Vol. 214, no. 7. — P. 1326–1340.

[30] Omer Kaab, Butcher Clifford, Worswick Michael. Characterization and application of a constitutive model for two 7000-series aluminum alloys subjected to hot forming // International Journal of Mechanical Sciences. — 2020. — Vol. 165. — P. 105218.

[31] Nemat-Nasser Sia, Li Yulong. Flow stress of f.c.c. polycrystals with application to OFHC Cu // Acta Materialia. — 1998. — Vol. 46, no. 2. — P. 565–577.

[32] Dynamic response of conventional and hot isostatically pressed Ti–6Al–4V alloys: experiments and modeling / Sia Nemat-Nasser, Wei-Guo Guo, Vitali F. Nesterenko et al. // Mechanics of Materials. — 2001. — Vol. 33, no. 8. — P. 425–439.

[33] Zerilli Frank J., Armstrong Ronald W. Constitutive relations for titanium and Ti-6Al-4V // AIP Conference Proceedings. — 1996. — Vol. 370, no. 1. — P. 315–318.

[34] Voyiadjis George Z., Abed Farid H. Microstructural based models for bcc and fcc metals with temperature and strain rate dependency // Mechanics of Materials. — 2005. — Vol. 37, no. 2. — P. 355–378. — New Directions in Mechanics and Selected Articles in Micromechanics of Materials.

[35] Voyiadjis George Z., Abed Farid H. Effect of dislocation density evolution on the thermomechanical response of metals with different crystal structures at low and high strain rates and temperatures // Archives of Mechanics. — 2005. — Vol. 57, no. 4. — P. 299–343.

[36] Song Yooseob, Yeon Jaeheum, Voyiadjis George Z. Constitutive modeling and numerical simulations for dynamic strain aging in MMFX steel at elevated temperatures // International Journal of Mechanical Sciences. — 2021. — Vol. 210. — P. 106743.

[37] Voyiadjis George Z., Song Yooseob, Rusinek Alexis. Constitutive model for metals with dynamic strain aging // Mechanics of Materials. — 2019. — Vol. 129. — P. 352–360.

[38] Rusinek A., Klepaczko J.R. Shear testing of a sheet steel at wide range of strain rates and a constitutive relation with strain-rate and temperature dependence of the flow stress // International Journal of Plasticity. — 2001. — Vol. 17, no. 1. — P. 87–115.

[39] Thermo-viscoplastic behavior of DP800 steel at quasi-static, intermediate, high and ultra-high strain rates / Bin Jia, Pengwan Chen, Alexis Rusinek, Qiang Zhou // International Journal of Mechanical Sciences. — 2022. — Vol. 226. — P. 107408.

[40] Thermo-viscoplastic behavior and constitutive relations for 304 austenitic stainless steel over a wide range of strain rates covering quasi-static, medium, high and very high regimes / Bin Jia, Yaoyue Zhang, Alexis Rusinek et al. // International Journal of Impact Engineering. — 2022. — Vol. 164. — P. 104208.

[41] Khan Akhtar S., Liu Jian. A deformation mechanism based crystal plasticity model of ultrafine-grained/nanocrystalline FCC polycrystals // International Journal of Plasticity. — 2016. — Vol. 86. — P. 56–69.

[42] Temperature effect on tensile behavior of an interstitial high entropy alloy: Crystal plasticity modeling / Xu Zhang, Xiaochong Lu, Jianfeng Zhao et al. // International Journal of Plasticity. — 2022. — Vol. 150. — P. 103201.

[43] Crystal plasticity-based impact dynamic constitutive model of magnesium alloy / Qijun Xie, Zhiwu Zhu, Guozheng Kang, Chao Yu // International Journal of Mechanical Sciences. — 2016. — Vol. 119. — P. 107–113.

[44] Xie Qijun, Zhu Zhiwu, Kang Guozheng. Thermal activation based constitutive model for high-temperature dynamic deformation of AZ31B magnesium alloy // Materials Science and Engineering: A. — 2019. — Vol. 743. — P. 24–31.

[45] Application of artificial neural networks in micromechanics for polycrystalline metals / Usman Ali, Waqas Muhammad, Abhijit Brahme et al. // International Journal of Plasticity. — 2019. — Vol. 120. — P. 205–219.

[46] Pantalé Olivier. Development and Implementation of an ANN Based Flow Law for Numerical Simulations of Thermo-Mechanical Processes at High Temperatures in FEM Software // Algorithms. — 2023. — Vol. 16, no. 1.

[47] Xu Z., Huang F. Artificial neural network modeling of mechanical properties of armor steel under complex loading conditions // Journal of Beijing Institute of Technology (English Edition). — 2012. — Vol. 21. — P. 157–163.

[48] Gu Yan, Zhang Chuanzeng, Golub Mikhail V. Physics-informed neural networks for analysis of 2D thin-walled structures // Engineering Analysis with Boundary Elements. — 2022. — Vol. 145. — P. 161–172.

[49] Counterexample-trained neural network model of rate and temperature dependent hardening with dynamic strain aging / Xueyang Li, Christian C. Roth, Colin Bonatti, Dirk Mohr // International Journal of Plasticity. — 2022. — Vol. 151. — P. 103218.

[50] Jordan Benoit, Gorji Maysam B., Mohr Dirk. Neural network model describing the temperature- and rate-dependent stress-strain response of polypropylene // International Journal of Plasticity. — 2020. — Vol. 135. — P. 102811.

[51] Cristescu N. A procedure for determining the constitutive equations for materials exhibiting both time-dependent and time-independent plasticity // International Journal of Solids and Structures. — 1972. — Vol. 8, no. 4. — P. 511–531.

[52] Lubliner Jacob. A generalized theory of strain-rate-dependent plastic wave propagation in bars // Journal of the Mechanics and Physics of Solids. — 1964. — Vol. 12, no. 1. — P. 59–65.

[53] Cottrell A. H., Bilby B. A. Dislocation Theory of Yielding and Strain Ageing of Iron // Proceedings of the Physical Society. Section A. — 1949. — Vol. 62, no. 1. — P. 49–62.

[54] Campbell J.D. The dynamic yielding of mild steel // Acta Metallurgica. — 1953. — Vol. 1, no. 6. — P. 706–710.

[55] Klepaczko Janusz R. On Fracture Enrgy of Concrete for Short-Time Loading in Tension // Brittle Matrix Composites 8 / Ed. by A. M. Brandt, V. C. Li, I. H. Marshall. — Woodhead Publishing, 2006. — P. 547–558.

[56] Stolarski A. Dynamic Strength Criterion for Concrete // Journal of Engineering Mechanics. — 2004. — Vol. 130, no. 12. — P. 1428–1435.

[57] Jankowiak T., Rusinek A., Wood P. Comments on paper: “Glass damage by impact spallation” by A. Nyoungue et al., Materials Science and Engineering A 407 (2005) 256–264 // Materials Science and Engineering: A. — 2013. — Vol. 564. — P. 206–212.

[58] Tuler Floyd R., Butcher Barry M. A criterion for the time dependence of dynamic fracture // International Journal of Fracture Mechanics. — 1968. — Vol. 4, no. 4. — P. 431–437.

[59] Petrov Yu. V., Utkin A. A. Dependence of the dynamic strength on loading rate // Soviet materials science : a transl. of Fiziko-khimicheskaya mekhanika materialov / Academy of Sciences of the Ukrainian SSR. — 1989. — Vol. 25, no. 2. — P. 153–156.

[60] Petrov Yu. V., Morozov N. F. On the Modeling of Fracture of Brittle Solids // Journal of Applied Mechanics. — 1994. — Vol. 61, no. 3. — P. 710–712.

[61] Petrov Yu. V. Quantum Analogy in the Mechanics of Fracture of Solids // Phys Solid State. — 1996. — Vol. 38, no. 11. — P. 1846—-1850.

[62] Morozov N. F., Petrov Yu. V. Dynamics of Fracture. — New York, NY : Springer Berlin, Heidelberg, 2000. — P. 98.

[63] Maximum yield strength under quasi-static and high-rate plastic deformation of metals / E. N. Borodin, A. E. Mayer, Yu. V. Petrov, A. A. Gruzdkov // Physics of the Solid State. — 2014. — Vol. 56, no. 12. — P. 2470–2479.

[64] A modified incubation time criterion for dynamic fracture of rock considering whole stress history / Xuan Xu, Li Yuan Chi, Jun Yang, Zong-Xian Zhang // International Journal of Rock Mechanics and Mining Sciences. — 2023. — Vol. 164. — P. 105361.

[65] An analytical approach to dynamic spalling of brittle materials / C. Yan, Z. Ou, Z. Duan, F. Huang // International Journal of Impact Engineering. — 2015. — Vol. 83. — P. 28–36.

[66] Yan C., Liu R., Ou Z. Analytical Model for Dynamic Yield Strength of Metal // Physical Mesomechanics. — 2019. — Vol. 22, no. 4. — P. 333–339.

[67] Petrov Yu. V. On the incubation stage of fracture and structural transformations in continuous media under pulse energy injection // Mechanics of Solids. — 2007. — Vol. 42, no. 5. — P. 692–699.

[68] Petrov Yu. V. Incubation time criterion and the pulsed strength of continua: Fracture, cavitation, and electrical breakdown // Doklady Physics. — 2004. — Vol. 49, no. 4. — P. 246–249.

[69] Petrov Yu. V., Borodin E. N. Relaxation mechanism of plastic deformation and its justification using the example of the sharp yield point phenomenon in whiskers // Physics of the Solid State. — 2015. — Vol. 57, no. 2. — P. 353–359.

[70] Relaxation model for dynamic plastic deformation of materials / Yu.V. Petrov, E.N. Borodin, E. Cadoni, N.S. Selyutina // EPJ Web of Conferences. — 2015. — Vol. 94. — P. 04039.

[71] The definition of characteristic times of plastic relaxation by dislocation slip and grain boundary sliding in copper and nickel / N. Selyutina, E.N. Borodin, Yu. V. Petrov, A.E. Mayer // International Journal of Plasticity. — 2016. — Vol. 82. — P. 97–111.

[72] Modeling of the thermal softening of metals under impact loads and their temperature–time correspondence / Shixiang Zhao, Yu. V. Petrov, Yuyi Zhang et al. // International Journal of Engineering Science. — 2024. — Vol. 194. — P. 103969.

[73] Effects of strain rate and stress state on mechanical properties of Ti-6Al-4V alloy / H. Hu, Z. Xu, W. Dou, F. Huang // International Journal of Impact Engineering. — 2020. — Vol. 145. — P. 103689.

[74] Khan Akhtar S., Sung Suh Yeong, Kazmi Rehan. Quasi-static and dynamic loading responses and constitutive modeling of titanium alloys // International Journal of Plasticity. — 2004. — Vol. 20, no. 12. — P. 2233–2248.

[75] Abed Farid, Makarem Fadi. Comparisons of Constitutive Models for Steel Over a Wide Range of Temperatures and Strain Rates // Journal of Engineering Materials and Technology. — 2012. — Vol. 134, no. 2.

[76] A Theory of Networks for Approximation and Learning : Rep. / MASSACHUSETTS INSTITUTE OF TECHNOLOGY ; Executor: Tomaso Poggio, Federico Girosi. — USA : 1989.

[77] A survey on modern trainable activation functions / Andrea Apicella, Francesco Donnarumma, Francesco Isgrò, Roberto Prevete // Neural Networks. — 2021. — Vol. 138. — P. 14–32.

[78] A privacy-preserving and non-interactive federated learning scheme for regression training with gradient descent / Fengwei Wang, Hui Zhu, Rongxing Lu et al. // Information Sciences. — 2021. — Vol. 552. — P. 183–200.

[79] Bottou Léon. Stochastic Gradient Descent Tricks // Neural Networks: Tricks of the Trade: Second Edition. — Berlin, Heidelberg : Springer Berlin Heidelberg, 2012. — P. 421–436.

[80] Schwab R., Ruff V. On the nature of the yield point phenomenon // Acta Materialia. — 2013. — Vol. 61, no. 5. — P. 1798–1808.

[81] Yoshida F., Kaneda Y., Yamamoto S. A plasticity model describing yield-point phenomena of steels and its application to FE simulation of temper rolling // International Journal of Plasticity. — 2008. — Vol. 24, no. 10. — P. 1792–1818. — Special Issue in Honor of Jean-Louis Chaboche.

[82] A generalized plasticity model incorporating stress state, strain rate and temperature effects / W. Dou, Z. Xu, H. Hu, F. Huang // International Journal of Impact Engineering. — 2021. — Vol. 155. — P. 103897.

[83] Determination of shear behavior and constitutive modeling of the 603 steel over wide temperature and strain rate ranges / Z. Xu, Y. Liu, H. Hu et al. // Journal of the Mechanics and Physics of Solids. — 2019. — Vol. 129. — P. 184–204.

[84] Zhao Shixiang, Petrov Yu.V., Volkov G.A. The modified relaxation plasticity model and the non-monotonic stress–strain diagram // International Journal of Mechanical Sciences. — 2023. — Vol. 240. — P. 107919.

[85] Zhao S., Petrov Yu. V., Volkov G. A. Modeling the Nonmonotonic Behavior Flow Curves under Dynamic Loads // Physical Mesomechanics. — 2022. — Vol. 25, no. 3. — P. 221–226.

[86] Selyutina N.S., Petrov Yu.V. Comparative Analysis of Dynamic Plasticity Models // Reviews on Advanced Materials Science. — 2018. — Vol. 57, no. 2. — P. 199–211.

[87] Selyutina N. S., Petrov Y. V. Instabilities of Dynamic Strain Diagrams Predicted by the Relaxation Model of Plasticity // Journal of Dynamic Behavior of Materials. — 2022. — Vol. 8, no. 2. — P. 304–315.

[88] Zadpoor A.A., Sinke J., Benedictus R. 4 - Numerical simulation modeling of tailor welded blank forming // Tailor Welded Blanks for Advanced Manufacturing / Ed. by Brad L. Kinsey, Xin Wu. — Woodhead Publishing, 2011. — Woodhead Publishing Series in Welding and Other Joining Technologies. — P. 68–94.

[89] Dynamic mechanical properties and constitutive equations of 2519A aluminum alloy / W. Liu, Z. He, Y. Chen, S. Tang // Transactions of Nonferrous Metals Society of China. — 2014. — Vol. 24, no. 7. — P. 2179–2186.

[90] Johnston W. G., Gilman J. J. Dislocation Velocities, Dislocation Densities, and Plastic Flow in Lithium Fluoride Crystals // Journal of Applied Physics. — 1959. — Vol. 30, no. 2. — P. 129–144.

[91] Zhao, Shixiang, Pronina, Yulia. On the stress state of a pressurised pipe with an initial thickness variation, subjected to non-homogeneous internal corrosion // E3S Web Conf. — 2019. — Vol. 121. — P. 01013.

[92] Zhao Shixiang, Pronina Yulia. On the MATLAB finite element modelling of an elastic plane with a hole under tension // 2017 Constructive Nonsmooth Analysis and Related Topics (dedicated to the memory of V.F. Demyanov) (CNSA). — 2017. — P. 1–4.

[93] Zhao S. On mechanochemical corrosion of a pipe with thickness deviation under the influence of external and internal pressure (In russian) // Togliatti State University science vector. — 2020. — no. 1. — P. 86–91.

[94] Zhao S. Algorithm for calculating the stress state of a plate with an elliptical hole in MATLAB (In russian) // Control process and stable performance. — 2017. — Vol. 4, no. 1. — P. 251–255.

[95] Nonlinear Finite Elements for Continua and Structures, 2nd ed. / T. Belytschko, W. Liu, B. Moran, K. Elkhodary. — Wiley, 2014.

[96] Zienkiewicz O., Taylor R. The finite element method for solid and structural mechanics. 7th ed. — Butterworth-Heinemann, 2014.

[97] Zienkiewicz O., Taylor R., J.Z. Zhu. The Finite Element Method: Its Basis and Fundamentals. 6th ed. — Butterworth-Heinemann, 2005.

[98] Hilber Hans M., Hughes Thomas J. R., Taylor Robert L. Improved numerical dissipation for time integration algorithms in structural dynamics // Earthquake Engineering & Structural Dynamics. — 1977. — Vol. 5, no. 3. — P. 283–292.

[99] Oden J. Tinsley. Finite Elements of Nonlinear Continua. — Dover publications, 1972.

[100] Ming, Lu, Pantalé, Olivier. An efficient and robust VUMAT implementation of elastoplastic constitutive laws in Abaqus/Explicit finite element code // Mechanics & Industry. — 2018. — Vol. 19, no. 3. — P. 308.

[101] Compressive Viscoplastic Response of 6082-T6 and 7075-T6 Aluminium Alloys Under Wide Range of Strain Rate at Room Temperature: Experiments and Modelling / W. Moćko, J. A. Rodriguez-Martinez, Z. L. Kowalewski, A. Rusinek // Strain. — 2012. — Vol. 48, no. 6. — P. 498–509.

[102] Winzer R., Glinicka A. The Static and Dynamic Compressive Behaviour of Selected Aluminium Alloys // Engineering Transactions. — 2014. — Vol. 59, no. 2. — P. 85–100.

[103] Low Cycle Fatigue Properties of Sc-Modified AA2519-T62 Extrusion / Robert Kosturek, Lucjan Śnieżek, Janusz Torzewski, Marcin Wachowski // Materials. — 2020. — Vol. 13, no. 1.

[104] Temperature-Dependent Material Property Databases for Marine Steels—Part 2: HSLA-65 / Jennifer K. Semple, Daniel H. Bechetti, Wei Zhang, Charles R. Fisher // Integrating Materials and Manufacturing Innovation. — 2022. — Vol. 11, no. 1. — P. 13–40.

[105] Babu Bijish. Physically Based Model for Plasticity and Creep of Ti-6Al-4V. — Lulea, Sweden : Luleå University of Technology, 2008.

[106] Dynamic response of conventional and hot isostatically pressed Ti–6Al–4V alloys: experiments and modeling / Sia Nemat-Nasser, Wei-Guo Guo, Vi-

tali F. Nesterenko et al. // Mechanics of Materials. — 2001. — Vol. 33, no. 8. — P. 425–439.

[107] Zerilli Frank J, Armstrong Ronald W. Constitutive relations for titanium and Ti-6Al-4V // Materials Science and Engineering: A. — 1996. — Vol. 209, no. 1-2. — P. 198–205.

[108] Finite element analysis and application based on ABAQUS (In Chinese) / Zhuo Zhuang, You Xiaochuan, Jianhui Liao, et al. — Tsinghua University Press, 2009.

[109] Xu Zejian, Huang Fenglei. Plastic behavior and constitutive modeling of armor steel over wide temperature and strain rate ranges // Acta Mechanica Solida Sinica. — 2012. — Vol. 25, no. 6. — P. 598–608.